



University of Kentucky  
UKnowledge

---

Theses and Dissertations--Physics and  
Astronomy

Physics and Astronomy

---

2018

## MAGNETIC FIELD DESIGN TO REDUCE SYSTEMATIC EFFECTS IN NEUTRON ELECTRIC DIPOLE MOMENT MEASUREMENTS

James Ryan Dadisman

*University of Kentucky*, ryandadisman@gmail.com

Digital Object Identifier: <https://doi.org/10.13023/ETD.2018.094>

[Right click to open a feedback form in a new tab to let us know how this document benefits you.](#)

---

### Recommended Citation

Dadisman, James Ryan, "MAGNETIC FIELD DESIGN TO REDUCE SYSTEMATIC EFFECTS IN NEUTRON ELECTRIC DIPOLE MOMENT MEASUREMENTS" (2018). *Theses and Dissertations--Physics and Astronomy*. 53.

[https://uknowledge.uky.edu/physastron\\_etds/53](https://uknowledge.uky.edu/physastron_etds/53)

This Doctoral Dissertation is brought to you for free and open access by the Physics and Astronomy at UKnowledge. It has been accepted for inclusion in Theses and Dissertations--Physics and Astronomy by an authorized administrator of UKnowledge. For more information, please contact [UKnowledge@lsv.uky.edu](mailto:UKnowledge@lsv.uky.edu).

## **STUDENT AGREEMENT:**

I represent that my thesis or dissertation and abstract are my original work. Proper attribution has been given to all outside sources. I understand that I am solely responsible for obtaining any needed copyright permissions. I have obtained needed written permission statement(s) from the owner(s) of each third-party copyrighted matter to be included in my work, allowing electronic distribution (if such use is not permitted by the fair use doctrine) which will be submitted to UKnowledge as Additional File.

I hereby grant to The University of Kentucky and its agents the irrevocable, non-exclusive, and royalty-free license to archive and make accessible my work in whole or in part in all forms of media, now or hereafter known. I agree that the document mentioned above may be made available immediately for worldwide access unless an embargo applies.

I retain all other ownership rights to the copyright of my work. I also retain the right to use in future works (such as articles or books) all or part of my work. I understand that I am free to register the copyright to my work.

## **REVIEW, APPROVAL AND ACCEPTANCE**

The document mentioned above has been reviewed and accepted by the student's advisor, on behalf of the advisory committee, and by the Director of Graduate Studies (DGS), on behalf of the program; we verify that this is the final, approved version of the student's thesis including all changes required by the advisory committee. The undersigned agree to abide by the statements above.

James Ryan Dadisman, Student

Dr. Brad Plaster, Major Professor

Dr. Christopher Crawford, Director of Graduate Studies

MAGNETIC FIELD DESIGN TO REDUCE SYSTEMATIC EFFECTS IN  
NEUTRON ELECTRIC DIPOLE MOMENT MEASUREMENTS

---

DISSERTATION

---

A dissertation submitted in partial  
fulfillment of the requirements for  
the degree of Doctor of Philosophy  
in the College of Arts and Sciences  
at the University of Kentucky

By  
James Ryan Dadisman  
Lexington, Kentucky

Director: Dr. Brad Plaster, Professor of Physics  
Lexington, Kentucky 2018

Copyright© James Ryan Dadisman 2018

## ABSTRACT OF DISSERTATION

### MAGNETIC FIELD DESIGN TO REDUCE SYSTEMATIC EFFECTS IN NEUTRON ELECTRIC DIPOLE MOMENT MEASUREMENTS

Charge-Conjugation (C) and Charge-Conjugation-Parity (CP) Violation is one of the three Sakharov conditions to explain via baryogenesis the observed baryon asymmetry of the universe (BAU). The Standard Model of particle physics (SM) contains sources of CP violation, but cannot explain the BAU. This motivates searches for new physics beyond the standard model (BSM) which address the Sakharov criteria, including high-precision searches for new sources of CPV in systems for which the SM contribution is small, but larger effects may be present in BSM theories. A promising example is the search for the electric dipole moment of the neutron (nEDM), which is a novel system to observe CPV due to the initial and final state being identical. A non-zero measurement necessarily requires violation of P and T discrete symmetries; invoking CPT invariance requires that CP is violated. There are BSM theories which predict a magnitude for the nEDM larger than SM predictions, so that such studies are beneficial at setting constraints on new physics. The current experimental limit of  $d_n < 3.0 \times 10^{-26} e \text{ cm}$  at 90% CL as set by the Institut Laue-Langevin (ILL) [1] was largely limited by systematic effects related to the magnetic field. The research presented here supported technical progress toward a new measurement of the nEDM, with the goal of improving the result by an order of magnitude. A novel approach to the problem of limiting systematics is proposed, studied in Monte Carlo simulations, and an optimized prototype was constructed for use in a magnetic resonance experiment.

KEYWORDS: Neutrons, electric dipole moment, magnetic fields

Author's signature: James Ryan Dadisman

Date: April 26, 2018

MAGNETIC FIELD DESIGN TO REDUCE SYSTEMATIC EFFECTS IN  
NEUTRON ELECTRIC DIPOLE MOMENT MEASUREMENTS

By  
James Ryan Dadisman

Director of Dissertation: Brad Plaster

Director of Graduate Studies: Christopher Crawford

Date: April 26, 2018

## ACKNOWLEDGMENTS

Thank you to my family,  
especially my wife Carrie and our children, Victoria and Logan.

Thank you to my adviser Brad Plaster for support and guidance.

Thank you to my initial adviser Susan Gardner for being supportive  
of my attempts at theory.

Thank you to my advising committee: Susan Gardner, Wolfgang Korsch,  
Alexandre Martin, and Brad Plaster.

Thank you to Alina Aleksandrova for the many projects we collaborated on,  
especially for contributions to the construction of the  $B_0$  coil  
and the in-situ mapper.

Thank you to Christopher Crawford for providing access to and help using COM-  
SOL.

Thank you to all of the collaborators on the LANL nEDM project.

Thank you to the University of Kentucky.

This material is based upon work supported by the U.S. Department of Energy,  
Office of Science, Office of Nuclear Physics under Award Number DE-SC0014622

# TABLE OF CONTENTS

Acknowledgments . . . . .	iii
List of Tables . . . . .	vi
List of Figures . . . . .	vii
Chapter 1 Theoretical Reasons for Neutron Electric Dipole Moment Searches . . . . .	1
1.1 Fundamental Symmetries . . . . .	2
1.2 Standard Model Contributions to the Neutron EDM . . . . .	4
Chapter 2 Measuring the Neutron EDM via the Ramsey Method of Separated Oscillatory Fields . . . . .	8
2.1 Ramsey Method of Separated Oscillatory Fields . . . . .	9
2.2 Ultracold Neutrons . . . . .	21
2.3 Gradient Field Effects . . . . .	23
Chapter 3 LANL nEDM Simulation . . . . .	31
3.1 General Simulation Methods . . . . .	31
3.2 Spin Tracking . . . . .	36
3.3 Magnetic Field Modeling . . . . .	37
3.4 Spin Relaxation . . . . .	43
3.5 Studying the Effects of Non-Constant Gradients . . . . .	49
Chapter 4 $B_0$ Coil Design . . . . .	54
4.1 Gapped Solenoid . . . . .	54
4.2 Current Optimizations in a Double-Gap Solenoid . . . . .	63
4.3 Ramsey Demonstration $B_0$ Coil . . . . .	66
4.4 In-Situ Mapping . . . . .	73
4.5 Full-size Neutron EDM $B_0$ Design Recommendations . . . . .	80
Chapter 5 LANL Ramsey Cycle Demonstration . . . . .	82
5.1 Setup . . . . .	82
5.2 Measurement Cycle . . . . .	85
5.3 Results . . . . .	87
Chapter 6 Time-Reversal Violation in B-Mesons . . . . .	91
6.1 BaBar Experiment . . . . .	91
6.2 Sensitivity to BSM Effects . . . . .	94
Chapter 7 Summary of Progress Toward a Neutron EDM Measurement . . . . .	99
7.1 Evaluation of the Multi-gap Solenoid Concept . . . . .	101

7.2	Improvements in Simulation of Neutron Electric Dipole Moment Experiments . . . . .	102
7.3	Magnetometry Improvements . . . . .	104
7.4	Final Notes on Magnetic Field Design for the Proposed LANL EDM Experiment . . . . .	106
	Bibliography . . . . .	108
	Vita . . . . .	113



## LIST OF TABLES

4.1	Comparison of theory to measured average fractional gradients for half-scale prototype $B_0$ coil. . . . .	62
4.2	Target nEDM uniformity compared with the prototype COMSOL models, centered and 3-in offset with z-shim. . . . .	72
6.1	Sample of initial and final state CP, T, and CPT asymmetries. . . . .	93

## LIST OF FIGURES

1.1	Feynman diagram of the leading order contribution to the neutron EDM considered by [14]. The CP-odd vertex shown contains the CPV phase from the CKM matrix. The second vertex is a CP-even, non-leptonic effective weak interaction. . . . .	6
(a)	Effective Feynman diagram . . . . .	6
(b)	Vertex 1 diagram . . . . .	6
2.1	Diagram showing the Ramsey method of separated oscillatory fields. [22]	11
2.2	Simulated Ramsey fringes for 10mG field with free precession times of $T = 1.8$ s and $T = 18$ s. . . . .	16
2.3	UCN production density at the ultracold neutron source at LANSCE as measured using the same apparatus as a function of year [27]. . . . .	22
2.4	Schematic diagram of the ultracold neutron source at LANSCE [27]. . . . .	24
2.5	Coordinate system for a cylindrical bottle. For the methods introduced in this chapter and used in the proceeding chapters, the nominal $B_0$ field is oriented with the $z$ -axis (longitudinal), and the transverse oscillating fields used to flip the spins are in the $xy$ plane. The electric field will be parallel or anti-parallel to the $B_0$ field. . . . .	28
3.1	Position distribution in $xy$ plane for different percentage of non-specular reflection: (a) 0.07%; (b) 2.2%; (c) 12.2%. . . . .	34
3.2	Tracks over 5 second period comparing specular and non-specular reflection. Specular reflections result in regular, repeating tracks which avoid the center. Non-specular reflections result in an increase in particle density near the center. . . . .	35
(a)	Cumulative tracks for 10 UCNs . . . . .	35
(b)	Single Example Specular Track . . . . .	35
(c)	Single Example Non-Specular Track . . . . .	35
3.3	Testing the precession within a constant magnetic field. . . . .	37
(a)	10N precessing for 1000s . . . . .	37
(b)	1N Precessing in transverse plane; frequency is correct for $B = 1\mu$ T	37
3.4	Polynomial fits along the main axes of the $B_0$ COMSOL model. . . . .	41
3.5	Comparison of the 49 parameter fit model to COMSOL along the $y$ -axis at different positions in $x$ and $z$ for the optimized double-gap solenoid. Fiducial volume is $z \in (-5$ cm, 5 cm) and $\rho < 25$ cm. . . . .	42
3.6	Histogram of the residuals comparing the $\ell = 6$ expansion with the COMSOL model of the $B_0$ prototype at $2.2 \mu$ T. . . . .	43
3.7	Example of simulation results fitted to exponential curve to extract $T_1$ . . . . .	44
3.8	A comparison of $T_1$ as a function of UCN energy for “realistic” and random wall reflections compared to the Redfield / McGregor model for a gas given as a function of temperature. . . . .	46

3.9	Sample histogram used to extract $T_2$ from simulation for $\left  \frac{dB_z}{dz} \right  = 5 \times 10^{-11}$ T mm <sup>-1</sup> , using random wall collisions and velocity $v = 7$ m/s. . . . .	47
3.10	A comparison of $T_2$ as a function of UCN energy for “realistic” and random wall reflections compared to the McGregor model for a low density gas as a function of temperature. . . . .	48
3.11	Comparison of $T_2$ for a linear and quadratic field profile, with purely specular reflections and a mix of non-specular. . . . .	52
4.1	A demonstration of the magnetic flux density between split solenoids (blue lines). Magnetic field lines (black lines) are plotted for simple bar magnets. Left: A single magnet’s magnetic field diverges in a dipole pattern. Right: Aligned with an opposite pole and with a gap, the flux is pushed inward, straightening the magnetic field lines along the length and decreasing the magnetic field gradients over a greater distance. . . . .	54
4.2	A demonstration of the increased magnetic field uniformity when a solenoid is placed within a magnetically shielded enclosure using 2D FEA. Left: A single magnet’s magnetic field diverges in a dipole pattern. Right: Surrounded by a material with high magnetic permeability which draws in magnetic flux density. . . . .	55
4.3	Concept used by Gosling and Cunningham [45]. A gapped solenoid is built of a cylindrical shell sheet of current with half-length $L_s$ and radius $a$ . The gap is modeled as a cylindrical shell sheet of current with half-length $L_g$ , identical radius, and opposite current. By superposition, this is equivalent to two individual solenoids of length $(L_s - L_g)$ with a gap of total length $2L_g$ and total coil length $2L_s$ . . . . .	56
4.4	4:7 Scale Gapped-Solenoid. Included are a set of saddle coils to reduce backgrounds. The field was mapped inside a cylindrical shield of axially-aligned strips of Metglas, a material with very high permeability used for magnetic shielding. . . . .	61
4.5	Diagram for asymmetric saddle coils, used to produce a transverse field capable of shimming constant field with a linear gradient. . . . .	62
4.6	Theory vs. Map along the $x$ and $z$ axes of the gapped solenoid. The left axis scale is for the field map, the right axis scale is for the theory plot. The saddle coils used to trim the background field are included in the theoretical gapped solenoid plot. . . . .	63
4.7	Contours of the vector potential are plotted for a DGS configuration of magnets. The blue lines represent edges of permanent magnets. Left: Inner and outer currents are equal. Right: Example with a substantially larger current in the outer coils relative to the inner coil. Note how the vector potential lines have gone from diverging to converging within the central coil. . . . .	64

4.8	Comparison of a COMSOL model of the prototype $B_0$ coil design for a solid solenoid (left), double-gapped solenoid (middle), and current optimized DGS with $I_{\text{Outer}} = 1.1I_{\text{Inner}}$ (right). The colormap scale has a range of 1% of the central magnetic field value $B_z = 10$ mG. The white box indicates the fiducial region. . . . .	65
4.9	Geometry used for benchmark $\cos\theta$ coils: The left geometry will produce a magnetic field along the $x$ -axis; the right will produce a magnetic field along the $z$ -axis. . . . .	65
4.10	COMSOL model comparing a $\cos\theta$ coil with the same dimensions and shielding as the prototype DGS (top) in the transverse ( $xy$ ) plane. The $\cos\theta$ coil produces nominally a field perpendicular to the longitudinal axis (left); it can be turned on its side (right) to produce a field in the same direction as the DGS. The white lines indicate the fiducial region under consideration for a double-chamber experiment, for which the DGS is proposed to be superior. . . . .	66
4.11	COMSOL model comparing a $\cos\theta$ coil with the same geometry and shielding as the prototype DGS (top) in the longitudinal ( $yz$ ) plane. The $\cos\theta$ coil produces nominally a field perpendicular to the longitudinal axis (left); it can be turned on its side (right) to produce a field in the same direction as the DGS. The white lines indicate the fiducial region under consideration for a double-chamber experiment, for which the DGS is proposed to be superior. . . . .	67
4.12	Double-gapped solenoid inside shield. The two vertical struts in the foreground, resting on the top of the $B_0$ frame, are rectangular fiberglass frames which support the spin-flipping $B_1$ coils. . . . .	68
4.13	Histogram of the transverse polarization angle, $\phi$ , after 350 s of free precession for the prototype $B_0$ coil set to produce a 10 mG field. The left histogram is for the upper velocity cutoff of the velocity distribution $v_{\text{max}} = 5$ m/s; the right histogram is for $v_{\text{max}} = 7$ m/s. . . . .	69
4.14	Measured background inside shield after degaussing. Dashed lines indicate the edge of the fiducial region. . . . .	70
4.15	Comparison of DGS with current optimization and without (current in inner and outer coils is the “same”) along $x$ -axis. Dashed lines indicate the edges of fiducial volume, and fields are normalized to the central value. . . . .	71
4.16	Measured $B_0$ coil at 110% current ratio compared to COMSOL model. . . . .	71
4.17	Comparison of separate radial and vertical offsets of 1 in between the center of the coil and the shield. The same color scale is used for each. . . . .	73
4.18	Rotating assembly: A) Hollow UHMW shaft; B) Acrylic top / bottom plates; C) Aluminum base; D) Teflon thrust bearing. . . . .	74
4.19	Diagram showing how the triple-axis magnetometers mount to slits in the vertical rails via brass screws for boundary value measurements. Screws hold the probe flush to the vertical rail, and there is clearance between the slit and the screws so that they are free to slide vertically. String connects at the top of the probe to set height. . . . .	75
4.20	Overview of internal assembly as setup for collecting volume maps. . . . .	76

4.21	Comparison of $B_0 = 22$ mG along the x-axis at different heights. . . . .	78
4.22	Comparison of background along the x-axis at different heights. . . . .	78
4.23	Comparison of $B_0$ to the background with a constant 22.08 mG offset. . . . .	79
4.24	$B_0$ with background subtracted at different heights. . . . .	79
4.25	$B_0 = 222$ mG at different heights. . . . .	80
4.26	Concept multi-gap solenoid with current optimizations. Colormap indicates the nominal field component with a scale of $\pm 0.1\%$ . Shield dimensions are $2\text{ m} \times 2\text{ m} \times 1\text{ m}$ . . . . .	81
5.1	Ramsey measurement general apparatus: (a) magnetic shield; (b) switcher; (c) analyzer; (d) polarizer. . . . .	83
5.2	Apparatus inside shield (excludes support structures), side view (Left) and angle view (Right): (a) $B_1$ coils; (b) $B_0$ coil; (c) storage cell. . . . .	84
5.3	Spin transport coil placement (five total, blue). . . . .	85
5.4	Combined quad measurement for a 30 s holding time. The initial peak near 55 s is due to the switcher connecting the chamber, with the cell valve closed, to the analyzer. The result is any UCNs left in the guide and valve assembly pass into the analyzer. The cell valve is opened at 85 s; the final peak at 95 s is due to the analyzer spin-flipper turning on, allowing the remaining UCNs of opposite spin-state to be counted. . . . .	86
5.5	Measurements for spin relaxation times $T_1$ and $T_2$ . . . . .	87
	(a) $T_1$ Measurement . . . . .	87
	(b) $T_2$ Measurement . . . . .	87
5.6	Measurement of the Rabi resonance envelope. . . . .	88
5.7	Central Ramsey fringe for $T = 1$ s, $\tau = 0.5$ s. . . . .	89
5.8	Ramsey fringe for $T = 10$ s, $\tau = 0.5$ s. . . . .	89
5.9	Ramsey fringe for $T = 20$ s, $\tau = 0.5$ s. . . . .	90
6.1	Lowest order “box” Feynman diagrams for $B\bar{B}$ mixing. By exchange of two charged $W^\pm$ bosons, the final state is the initial state under charge-conjugation: $d\bar{b} \rightarrow b\bar{d}$ . The diagrams are identical for the opposite oscillation. . . . .	92
6.2	Leading order decay modes for the neutral B-meson. Of special interest to CKM unitarity angle $\beta$ is the decay of $b \rightarrow c\bar{c}\bar{s}$ . . . . .	93
	(a) Semi-leptonic Decay . . . . .	93
	(b) Mesonic Decay: Tree Diagram . . . . .	93
	(c) Mesonic Decay: Penguin Diagram . . . . .	93

6.3	The transition $B^0 \rightarrow B_-$ and the construction of its time-conjugate $B_- \rightarrow B^0$ . a) Idealized: the initial detection of $\ell^-$ projects the surviving $B$ into the orthogonal flavor state, realizing $B^0 \rightarrow B_-$ upon subsequent detection of $J/\psi K_S$ , whereas the initial detection of $J/\psi K_L$ projects the surviving $B$ into the $CP = -$ state. In this latter case subsequent detection of $\ell^+ X$ realizes $B_- \rightarrow B^0$ , the time-reversed process associated with $B^0 \rightarrow B_-$ . The initial-state projections can be thought of as inverse decays of $\ell^+$ and $J/\psi K_S$ , respectively [56]. b) Expanded to include the particles that are detected (boxes) to tag the initial and final states of the $B$ -meson. The second process is not the time conjugate of the first once direct $CP$ violation in the tagging decay is included. The $CP$ state of the $B$ -meson prepared through inverse decay is not identical to that of the $B$ which decays to $J/\psi K_S(\pi^+\pi^-)$ . . . . .	95
7.1	Histograms showing the simulated neutron distribution as a function of radius for roughness parameters $b = 2\text{nm}$ , $w = 10\text{nm}$ (left), and $b = 25\text{nm}$ , $w = 125\text{nm}$ (right). . . . .	99
7.2	A model 4-gap solenoid, lightly optimized for a double-chamber configuration. Model is shown on the left, $B_z$ is shown on the right. The white box indicates the edges of the fiducial volume. Note the heatmap scale is $(1 \pm 7.6 \times 10^{-5}) \times 13.175$ [mG]. . . . .	102
7.3	A simulated Ramsey measurement to determine the false EDM. Note the leading order estimate is shifted by nearly $\delta\nu/2$ ; as a result, only $\sim 25\%$ of the simulated frequencies are useful. . . . .	105

## Chapter 1 Theoretical Reasons for Neutron Electric Dipole Moment Searches

The first measurement of the neutron electric dipole moment (EDM) was published by Smith, Purcell and Ramsey in 1957 [2], and was consistent with a zero EDM as “would be expected based on the argument of time-reversal invariance”. This was seen as a significant test of the fundamental symmetries of parity and time reversal; a non-zero result would indicate violation of each. In the 1940’s and 1950’s, there was considerable debate regarding whether these symmetries were universally conserved. The consensus at the time was yes, until parity violation (PV) was observed in nuclear beta decay of  $^{60}\text{Co}$  by Wu et al. in 1957 [3] based on the suggestion from Lee and Yang [4] that PV may occur in the weak interaction. In the aftermath of this result, it was postulated that perhaps the combined transformation of charge-conjugation with parity (CP) is conserved. This postulate was short-lived, as CP violation was observed in kaon decays in 1964 [5]. This led to the consensus that the combination of charge-conjugation with parity and time reversal (CPT) must be invariant, which is still observed to be true today.

More generally, any quantum field theory which uses a Hermitian Hamiltonian and is invariant under Lorentz transformations must also be invariant under the combined CPT transformation [6], [7]. The Hamiltonian must be Hermitian in order for the energy eigenvalues, which are observable, to be real, and Lorentz invariance is required for the laws of physics to be valid in any inertial frame. Consequently, CPT must be a conserved symmetry of nature.

Time-reversal violation (TV) has only recently been observed by the BaBar Collaboration [8] in oscillations of entangled  $B - \bar{B}$  pairs. BaBar was able to test CP, T, and CPT separately, observing CPT invariance with separate CPV and TV consistent with SM predictions for CPV due to the weak interaction. This would seemingly reduce the importance of measuring the neutron EDM as a fundamental symmetry test, but the importance remains as a probe of additional sources of CP violation.

A leading open question in physics is the origin of the Baryon Asymmetry of the Universe (BAU): why is there so much more matter than anti-matter? The presence of C and CP violation is one of the three conditions proposed by Sakharov to explain how the currently observed asymmetry between matter and anti-matter could have developed through baryogenesis; additionally the process must change baryon number and must be out of thermal equilibrium [9]. The known CP violation in the standard

model gives a prediction for BAU, defined as the difference between baryons and anti-baryons over the number of observed photons  $\eta = (n_B - n_{\bar{B}})/n_\gamma$ , as  $\eta \approx \mathcal{O}(10^{-18})$  [10], 8 orders of magnitude smaller than the result derived from the cosmic microwave background  $\eta \approx 6 \times 10^{-10}$  [11].

It seems there must be some additional sources of CP violation beyond the standard model (BSM). The discovery of the Higgs boson mass of 125 GeV, made by the CMS collaboration at the Large Hadron Collider [12], constrains electroweak baryogenesis models such that BSM physics are necessary to describe the BAU [13]. This motivates a search for sources of BSM physics which violate CP, which could possibly satisfy the Sakharov criteria. The standard model prediction for the neutron EDM is so small,  $\mathcal{O}(10^{-32} e \text{ cm}^{-1})$  [14], that the search for a non-zero value is a promising method to probe new physics. Existing BSM theories predict the neutron EDM to be between the current result  $d_n \leq 3.0 \times 10^{-26} e \text{ cm}$  at 90% CL and the SM prediction.

## 1.1 Fundamental Symmetries

A continuous symmetry can be parametrized with a continuous parameter in the generator of the symmetry; by the Noether theorem this leads to some conserved “charge”. For example, the generator of rotations about the z-axis is represented by the unitary operator  $U = \exp(-i\phi\hat{L}_z)$  for which the conserved charge is angular momentum  $L_z$ . Symmetries and conserved charges represent a rich theoretical topic, but discrete symmetries, which cannot be parametrized with a continuous parameter, play a more central role in the theoretical underpinnings of the neutron electric dipole moment.

There are three types of discrete symmetries: Parity, Charge-conjugation, and Time-reversal. They are distinct from continuous symmetries in that a continuous parameter cannot generate the transformations. Starting with parity, which is the easiest of these to understand: all spatial coordinates are changed by a sign flip:  $\vec{r} \rightarrow -\vec{r}; x \rightarrow -x, y \rightarrow -y, z \rightarrow -z$ . This is equivalent to changing from a right-handed Cartesian system to a left-handed Cartesian system for three spatial dimensions, which is perfectly suitable language for visualizing why it is discrete: it is impossible to make a right hand look like a left hand by rotation only! Parity is often incorrectly described as “mirror” symmetry. In a 1-dimensional case, this is correct; however, a mirror does not flip all coordinates, so that the analogy is inaccurate. Vectors change sign under parity, e.g., position  $\vec{r}$  and velocity  $\vec{v}$ ; pseudo-vectors do not, e.g., angular momentum  $\vec{L}$ .



$$P\vec{r} = -\vec{r} \quad (1.1)$$

$$P\vec{v} = -\vec{v} \quad (1.2)$$

$$P\vec{L} = P(\vec{r} \times m\vec{v}) = (-\vec{r} \times -m\vec{v}) = \vec{r} \times m\vec{v} = \vec{L} \quad (1.3)$$

Charge-conjugation is the transformation of particles to anti-particles, and vice-versa. It is trivial to see that this cannot be achieved by any type of continuous transformation, as particles are inherently discrete. Charge-conjugation, like parity, is in most cases simple to change or observe in an experiment with charged particles. Production of particles and anti-particles are typically similar, e.g., through decay of more massive particles or via pair production at an energy resonance in a particle collider. This statement refers more to unstable particles which decay, e.g. - pions. Abundant particles which are stable, e.g., electrons, can be easily extracted from materials, as opposed to their anti-particles which are not readily available due to the BAU. For production processes which produce mixtures of charged particles and anti-particles, it is straightforward to separate them using electric or magnetic fields.

Time reversal symmetry is conceptually simple, but difficult to realize in an experiment. As the name implies, TR is reversing the direction of time  $t \rightarrow -t$ , or equivalently switching initial and final states. In physics we typically look at collisions or decays in which the initial state may be a collinear beam of particles and the final state may be a set of identical particles anisotropic in space and time with momenta directed radially outward from the site of decay or collision. To attempt a TR experiment would require precise control of the energy, momenta, and timing at the individual particle level, which is extremely infeasible for most experiments.

PV and CPV have been extensively studied experimentally, excellent summaries of which can be found in review articles from the Particle Data Group (PDG) [15]. I would like to focus on TR, as it has historically been a significant motivation for measuring the neutron EDM. I will start with a discussion of CP and T violation in the standard model as related to the neutron EDM. This will lead into a thorough discussion of the Rabi and Ramsey methods as applied to a neutron EDM measurement and the significance of magnetic field design. Chapters 3 and 4 discuss the original work performed in magnetic field design and simulations, as applied to a prototype apparatus utilized in Rabi and Ramsey measurements using the ultracold neutron source at the Los Alamos Neutron Science Center (LANSCE) 5. The final chapter is a discussion of the first observation of TR violation in a system, measured by the

BaBar collaboration using entangled B-mesons, and a proposed method of analysis to which I contributed that may be used to elucidate small SM or new physics effects via construction of pseudo-‘T’ asymmetries.

## Baryon Number Violation

The additional Sakharov criteria necessary to give rise to a non-zero BAU as a result of baryogenesis are that processes which change baryon number exist, and that the processes which violate CP and change baryon number occur out of thermal equilibrium. Establishing baryon number as  $B = \pm 1$  for baryons and anti-baryons, respectively, summing over the entire universe would quantify the BAU. In introducing the Sakharov conditions, the discussion focused on CP violation as though baryon number violation is secondary to CPV; quite the opposite is true. Charge-conjugation effectively changes the baryon number sign for the particles in an interaction. For a process which does not change the baryon number from initial to final states, CPV will not contribute to the BAU because the number of baryons is unchanged. Therefore, processes must exist which violate baryon number so that the net baryon number of the universe can possibly change.

A baryon number violating process in itself is necessary but insufficient. For a general process which results in  $\Delta B = +1$ , there is a charge-conjugated process which results in  $\Delta B = -1$ . If the two processes occur equally, then the net baryon number of the universe remains unchanged. This is why C and CP violation are required: in order for an asymmetry to form, processes which produce an abundance of baryons must be favored relative to the processes which produce an abundance of anti-baryons.

The requirement that the baryon number violating processes occur outside of thermal equilibrium may be demonstrated by considering a set of arbitrary reactants and products:  $A + B \leftrightarrow C + D$ . In thermal equilibrium, the number of each is conserved, i.e., the system is invariant under T transformations. This implies that, in thermal equilibrium, the net number of baryons and anti-baryons is unchanged in time and thus an asymmetry cannot form.

## 1.2 Standard Model Contributions to the Neutron EDM

The simplest method of interpreting the effects of PV and TV in the neutron EDM is based on an examination of the Hamiltonian:

$$H_n = -\vec{\mu}_n \cdot \vec{B} - \vec{d}_n \cdot \vec{E} \tag{1.4}$$

The only intrinsic “vector” along which the magnetic and electric moments must align is the spin:  $\vec{\mu}_n = \mu_n \vec{J}/J$ ; and  $\vec{d}_n = d_n \vec{J}/J$ . The sign of the electric dipole moment is embedded in the scalar  $d_n$  as shown, and is to be determined experimentally. This means  $\vec{d}_n$  behaves like  $\vec{J}$ , a pseudo-vector, under discrete symmetries. The magnetic field is also a pseudo-vector, whereas the electric field is a vector. The electric dipole term in the Hamiltonian is thus a pseudo-scalar which changes sign separately under  $P$  and  $T$ , whereas the magnetic moment term is a scalar that is unchanged under each. A non-zero value for the electric dipole moment will violate  $P$  and  $T$  symmetry; by invoking  $CPT$  invariance,  $CP$  is also violated.

There are two sources in the Standard Model (SM) which allow for  $CP$  and  $T$  violation: the complex phase present in the Cabibbo-Kobayashi-Masukawa (CKM) matrix due to the weak force; and the so-called  $\theta$ -term in the strong force. The relative strength of the  $\theta$ -term is an outstanding problem in physics: it is observed to be  $|\theta| < 7.4 \times 10^{-11}$ , the current limit actually set by the neutron electric dipole moment [16], though as a phase it is expected to take any value from 0 to  $2\pi$ .

$CPV$  in the weak interaction is well understood and has been experimentally observed in systems with kaons and B-mesons. The flavor and mass eigenstates of quarks differ, which results in a mixing between  $u$ -type and  $d$ -type quarks when coupled to a  $W^\pm$  boson. The relative weighting of the quark mixing is given by the CKM matrix. A look at equation 1.5 and sum of the squares of any row or column demonstrates that the CKM matrix is unitary to current precision [15].

$$|V|_{CKM} = \begin{pmatrix} 0.97417(21) & 0.2248(6) & 0.00409(39) \\ 0.220(5) & 0.995(16) & 0.0405(15) \\ 0.0082(6) & 0.0400(27) & 1.009(31) \end{pmatrix} \quad (1.5)$$

$$|V_{i1}|^2 + |V_{i2}|^2 + |V_{i3}|^2 = |V_{1j}|^2 + |V_{2j}|^2 + |V_{3j}|^2 = 1 \quad (1.6)$$

When calculating the interaction amplitude of a Feynman diagram, a vertex which includes a  $u$ ,  $d$ -type quark conversion carries an additional factor of  $V_{ij}$ , corresponding to  $u$ -type quark  $i$  and  $d$ -type quark  $j$ . The source of  $CP$  violation is the phase  $\delta$  which arises from a parametrization of the matrix elements with 3 mixing angles  $\theta_{12}, \theta_{13}, \theta_{23}$ , and phase  $\delta$  [17].

$$V_{CKM} = \begin{pmatrix} c_{12}c_{13} & s_{12}c_{13} & s_{13}e^{-i\delta} \\ -s_{12}c_{23} - c_{12}s_{23}s_{13}e^{i\delta} & c_{12}c_{23} - s_{12}s_{23}s_{13}e^{i\delta} & s_{23}c_{13} \\ s_{12}s_{23} - c_{12}c_{23}s_{13}e^{i\delta} & -c_{12}s_{23} - s_{12}c_{23}s_{13}e^{i\delta} & c_{23}c_{13} \end{pmatrix} \quad (1.7)$$

Thus far, CP violation has not been discovered in any flavor-conserving interactions [17]. The presence of a neutron EDM clearly does not change the quark flavor as the initial and final state is that of a neutron, so that the discovery of a non-zero result would be historic.

The CPV phase  $\delta$  must not cancel out from Feynman diagrams in order for a particular diagram to violate CP and T. This is not possible for a neutron coupling to an external photon until the Feynman diagram has at least 3-loops [18]. The tree

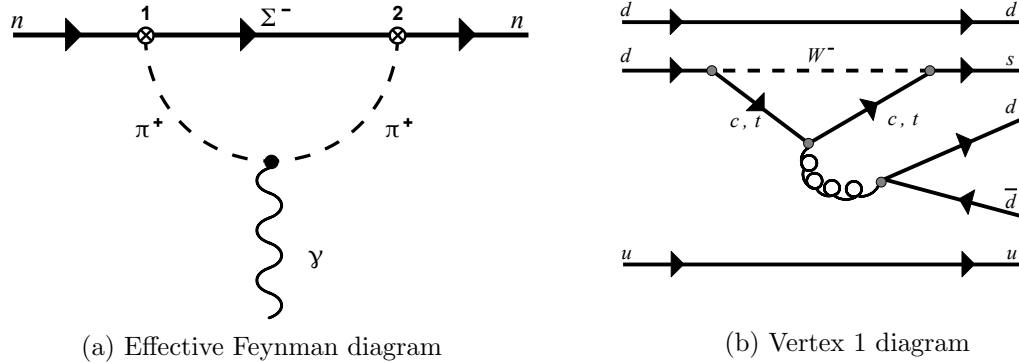


Figure 1.1: Feynman diagram of the leading order contribution to the neutron EDM considered by [14]. The CP-odd vertex shown contains the CPV phase from the CKM matrix. The second vertex is a CP-even, non-leptonic effective weak interaction.

level process is a purely QED interaction, i.e., emission or absorption of a photon with no weak interaction, which does not violate C, P, or T and therefore will not contribute to an EDM. The 1-loop diagram would involve a  $W^\pm$  loop; however there are only two vertices with CKM factors, such that the  $V_2 = V_1^*$  so that the CP-violating phase will cancel. Shabalin showed that, though the phase survives in individual Feynman 2-loop level diagrams, the contributions from diagrams with different quarks causes the EDM to vanish at the 2-loop level [18]. Several methods have been used to determine the neutron EDM with leading order 3-loop diagrams. A calculation made by Khriplovich and Zhitnisky, shown in figure 1.1, couples an external photon to an intermediate  $\pi^+$ , where one vertex is a CP-even  $n\pi^+\Sigma^-$  effective weak interaction and the other is CP-odd as a result of quark mixing. Note in figure 1.1b that the  $d$  quark is mixing to  $c$  or  $t$ ; the CKM matrix element  $V_{ud}$  does not contain the phase  $\delta$  so that it would not result in CPV. The resulting dipole moment of  $d_n = 2 \times 10^{-32} e$  cm [14] is one of the larger SM predictions. Considerably more 3-loop diagrams can be drawn using the CKM mechanism at the purely quark level; in order to violate CP, they must include quark mixing which results in different combinations of CKM

matrix elements which do not cancel the phase  $\delta$ . Purely quark level calculations result in lower SM predictions for the neutron EDM  $d_n \approx 10^{-34} e \text{ cm}$  [19].

## Chapter 2 Measuring the Neutron EDM via the Ramsey Method of Separated Oscillatory Fields

The most recent upper limit for a neutron EDM of  $3.0 \times 10^{-26} e \text{ cm}$  at 90% CL was determined by a room-temperature experiment conducted at the Institut Laue-Langevin [1] using ultracold neutrons (UCN) with kinetic energy  $\mathcal{O}(100 \text{ neV})$ . There are several new experiments proposed to further improve this limit, notably a proposal by Golub and Lamoreaux [20] to be performed at the Spallation Neutron Source (SNS) at Oak Ridge National Laboratory. There are many technical hurdles pertinent for this experiment, largely related to cryogenics and in-situ UCN production. As a stepping stone to this experiment, and following an upgrade to the UCN source at LANL, work has been made toward a room-temperature experiment targeting a result between the ILL limit and that proposed by the SNS experiment. Much of my research is in support of this proposed experiment for LANL.

In the presence of a constant magnetic field, it is well understood that a neutron's spin will precess at the Larmor precession frequency as determined from the Hamiltonian 1.4.

$$\nu_L = -\frac{\gamma_n B}{2\pi} \quad (2.1)$$

A modification to this is required if the neutron also has an electric dipole moment. The EDM vector should be parallel or anti-parallel to the spin vector, analogous to the magnetic moment  $\mu_n$  which is embedded in the gyromagnetic ratio  $\gamma_n$  present in equation 2.1. The full precession frequency becomes, with the sign of the EDM relative to the neutron spin absorbed into the variable  $d_n$ :

$$\nu_n = -2[\mu_n B + d_n E] / h \quad (2.2)$$

here  $h$  is Planck's constant. The shift associated with the electric dipole moment is very small: using the upper end of the standard model prediction  $d_n \sim 10^{-32} e \text{ cm}$  [14] with an electric field of 10 kV/cm would result in a frequency shift  $\sim 50 \text{ fHz}$ . The Larmor frequency due to the magnetic field, required to maintain polarization during the experiment, is  $\sim 30 \text{ Hz}$ , so that this fractional shift in frequency is  $\sim 10^{-15}$ . Direct measurement of a very small frequency shift is difficult, so sophisticated methods which allow a long time for phase to accumulate is preferred. The Ramsey method

of separated oscillatory fields is one of the premier methods, and the foundation for the LANL nEDM experiment.

## 2.1 Ramsey Method of Separated Oscillatory Fields

A problem arises in trying to directly measure accumulated phase in the plane transverse to the electric and magnetic fields: a count of spin-up and/or spin-down states is measured, and this is not trivially related to a small shift in frequency. Fortunately, such information can be accessed by applying an oscillating field transverse to the initial polarization. This is known as the Rabi method, and relies on the probability of the spin flipping in the presence of an oscillating field having a resonance when the oscillation frequency is near the Larmor frequency. A key modification to this Rabi method was proposed by Ramsey to increase the sensitivity of such measurements [21].

### Derivation of the Rabi Resonance Method

Consider the Schrödinger equation for a general spinor in the  $S_z$  basis under the application of a time-oscillating transverse field.

$$|\Psi\rangle = \begin{pmatrix} \psi_+(t) \\ \psi_-(t) \end{pmatrix} \quad (2.3)$$

$$i\hbar \begin{pmatrix} \dot{\psi}_+(t) \\ \dot{\psi}_-(t) \end{pmatrix} = -\frac{\hbar\gamma_g}{2} \begin{pmatrix} B_0 & B_1 e^{-i\omega t} \\ B_1 e^{i\omega t} & -B_0 \end{pmatrix} \begin{pmatrix} \psi_+(t) \\ \psi_-(t) \end{pmatrix} \quad (2.4)$$

where  $\gamma_g$  is the gyromagnetic ratio of the particle and  $\omega$  is the angular frequency of the applied oscillating field  $B_1$ . It is of particular interest to determine the probability of an initially spin-up polarization flipping to the opposite state after the oscillating field has been turned on for some time. For simplicity the transverse  $B_1$  field is considered “circular”, i.e.- composed of perpendicular components in the transverse plane with the same magnitude but out of phase by  $90^\circ$ . It is convenient to separate the time dependence in the state which is the result of the unperturbed Hamiltonian,  $H_0$ , and the time dependence due to the time-dependent perturbation,  $H_I$ .

$$H = H_0 + H_I; \quad H_0 = -\frac{\hbar\gamma B_0}{2}\sigma_z; \quad H_I = -\frac{\hbar\gamma B_1}{2} \begin{pmatrix} 0 & e^{-i\omega t} \\ e^{i\omega t} & 0 \end{pmatrix} \quad (2.5)$$

$$E_{\pm} = \mp \frac{\hbar}{2}\gamma B_0 = \mp \hbar \frac{\omega_0}{2} \quad (2.6)$$

$$|\psi_+\rangle = \begin{pmatrix} 1 \\ 0 \end{pmatrix}; \quad |\psi_-\rangle = \begin{pmatrix} 0 \\ 1 \end{pmatrix} \quad (2.7)$$

$$\Psi(t) = u(t)e^{-iE_+t/\hbar}\psi_+ + d(t)e^{-iE_-t/\hbar}\psi_- \quad (2.8)$$

The probability that the spin is found in the up or down state at a later time is dependent purely on the solutions to the scalar functions  $u(t)$  and  $d(t)$ , respectively. Assuming an initially polarized sample, this reduces to an initial value problem with conditions  $u(t=0) = 1$  and  $d(t=0) = 0$ . A simplification which arises by the use of perturbation theory is that the interaction terms in the Hamiltonian have now been separated from the non-interaction, constant field terms. The exact solution is given by the coupled differential equations:

$$\dot{u} = \frac{i\gamma B_1}{2}e^{i(\omega-\omega_0)t}d \quad (2.9)$$

$$\dot{d} = \frac{i\gamma B_1}{2}e^{-i(\omega-\omega_0)t}u \quad (2.10)$$

Here  $\omega_0 = (E_+ - E_-)/\hbar = \gamma_n B_0$ . Taking the derivative of 2.9 and substituting  $\dot{d}$  from equation 2.10 yields a 2<sup>nd</sup> order homogeneous differential equation with constant coefficients.

$$\ddot{u} - i(\omega - \omega_0)\dot{u} + \frac{\gamma^2 B_1^2}{4}u = 0 \quad (2.11)$$

with general solution

$$u(t) = e^{i\frac{\omega-\omega_0}{2}t} [C_1 e^{i\Omega t} + C_2 e^{-i\Omega t}] \quad (2.12)$$

$$\Omega = \frac{\sqrt{(\omega - \omega_0)^2 + \gamma^2 B_1^2}}{2} \quad (2.13)$$

$d(t)$  can be determined from the derivative of the general solution to  $u(t)$  using equation 2.9. Assuming an initial ‘‘up’’ polarization, the coefficients  $C_1, C_2$  are solved



using initial values  $u(t = 0) = 1$ ,  $d(t = 0) = 0$ . The probability of a spin flip after time  $t$  is given by  $|d(t)|^2$ .

$$d(t) = \frac{i\gamma B_1}{\sqrt{(\omega - \omega_0)^2 + \gamma^2 B_1^2}} \sin\left(\frac{\sqrt{(\omega - \omega_0)^2 + \gamma^2 B_1^2}}{2} t\right) \quad (2.14)$$

$$\begin{aligned} P_{+\rightarrow-}(t) &= |\langle \psi_- | \Psi(t) \rangle|^2 = |d(t)|^2 \\ &= \frac{\gamma^2 B_1^2}{(\omega - \omega_0)^2 + \gamma^2 B_1^2} \sin^2\left(\frac{\sqrt{(\omega - \omega_0)^2 + \gamma^2 B_1^2}}{2} t\right) \end{aligned} \quad (2.15)$$

This is the famous Rabi formula, with Rabi frequency  $\Omega = \sqrt{(\omega - \omega_0)^2 + \gamma^2 B_1^2}/2$ . Of particular interest is the  $(\omega - \omega_0)^2$  term in the denominator, which produces a resonance peak at the precession frequency  $\omega_0$ . This method was first proposed by Rabi to improve measurements of atomic energy transitions. A simple yet elegant modification was proposed by Ramsey [21]: break a Rabi spin flip into two  $\pi/2$  pulses, separated by a period of time with a constant holding field.

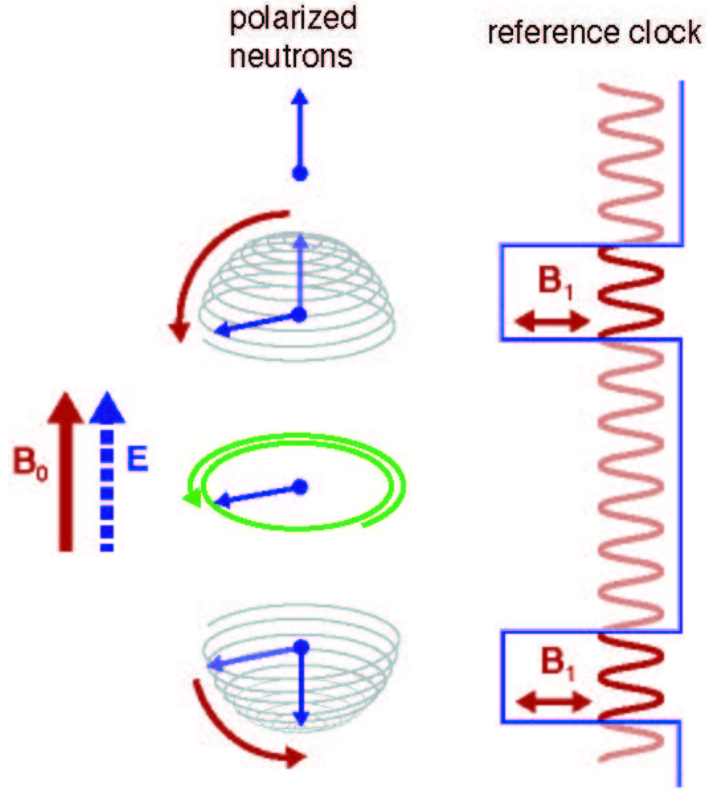


Figure 2.1: Diagram showing the Ramsey method of separated oscillatory fields. [22]

Figure 2.1 shows a general overview of the Ramsey method. Neutrons start polarized along a constant magnetic field  $B_0$ . A reference clock, represented by the oscillating wave on the right side of the figure, maintains the frequency at which the neutron spin is probed, and maintains a coherent phase throughout the process. A transverse magnetic field,  $B_1$ , is turned on and driven by the reference clock to apply two separate  $\pi/2$  pulses; the first tips the spin into the plane transverse to the holding field  $B_0$ . If the frequency is on resonance, the second  $\pi/2$  pulse will complete a spin-flip relative to the initial polarization. The  $B_1$  field is turned off between these two pulses, so that the spins freely precess in the plane transverse to the  $B_0$  field for time  $T$ . If the spin-flip pulses are executed consecutively so that  $T = 0$  s, then this reduces to the Rabi method for a  $\pi$  spin-flip. Splitting the spin-flip into two  $\pi/2$  pulses separated in time introduces oscillations of the spin-flip probability which enables a more precise determination of the resonant frequency.

### Derivation of the Ramsey Resonance Method

Using the formalism of the Rabi derivation as a starting point, a unitary transformation can be constructed to determine the final state, given some initial wavefunction  $\Psi$ . There are three distinct stages of the Ramsey method: 1. The initial  $\pi/2$  spin flip for time  $\tau$ ; 2. The free precession in ideally constant magnetic field for time  $T$ ; 3. The final  $\pi/2$  spin flip, ideally for the same time  $\tau$  used for the initial spin flip. A single unitary operator can describe this entire process, constructed by taking the product of separate unitary operators acting on the wavefunction in each stage:  $U = U_{\frac{\pi}{2}} U_0 U_{\frac{\pi}{2}}$ . The central operator used during free precession is found using the energy eigenvalues.

$$U_0 = \begin{pmatrix} e^{\frac{\omega_0}{2}t} & 0 \\ 0 & e^{-\frac{\omega_0}{2}t} \end{pmatrix} \quad (2.16)$$

A simplification was implicitly made in the Rabi derivation which must now be corrected. No consideration was given as to the phase of the transverse field which induces the spin flips. In the case of an initially spin-up neutron, a phase will cancel out of the observable probability of a spin-flip. With two separate spin rotations, there can now be interference between the phases, such that a cancellation will not necessarily occur. This can be accounted for by modifying the interaction terms in the Hamiltonian.

$$H_I = -\frac{\hbar}{2}\gamma_n B_1 \begin{pmatrix} 0 & e^{-i(\omega t + \phi)} \\ e^{i(\omega t + \phi)} & 0 \end{pmatrix} \quad (2.17)$$

As with the Rabi method, the result is a pair of coupled differential equations, with an additional phase.

$$\dot{u} = \frac{i\gamma_n B_1}{2} e^{i(\omega - \omega_0)t + i\phi} d \quad (2.18)$$

$$\dot{d} = \frac{i\gamma_n B_1}{2} e^{-i(\omega - \omega_0)t - i\phi} u \quad (2.19)$$

For a single application of the transverse, oscillating field starting in a polarized state with  $u(t=0) = 1$  and  $d(t=0) = 0$ , this phase will cancel out in the observable probability of a spin flip after time  $t$ ,  $|d(t)|^2$ . The phase cannot be ignored, however, if multiple applications of the spin-flipping field will occur because the initial state for all applications subsequent to the first are dependent on  $u(t)$  and  $d(t)$ , which still include the accumulated phase. Additionally, the final state will include a phase contribution from the unperturbed Hamiltonian as shown in the general solution for the time evolution, equation 2.2. Rather than attempting to solve for final states  $|\Psi_f\rangle$  given arbitrary initial states  $|\Psi_i\rangle = \begin{pmatrix} \psi_{+,i} \\ \psi_{-,i} \end{pmatrix}$  with complex values for  $\psi_{+,i}$  and  $\psi_{-,i}$ , it is favorable to build a unitary operator  $U_{\frac{\pi}{2}}$  which can perform the general transformation from initial to final states during the spin-flip  $|\Psi_f\rangle = U_{\frac{\pi}{2}} |\Psi_i\rangle$ .

$$|\Psi_f\rangle = U_{\frac{\pi}{2}}(\tau) |\Psi_i\rangle \quad (2.20)$$

$$\begin{pmatrix} \psi_{+,f} \\ \psi_{-,f} \end{pmatrix} = \begin{pmatrix} U_{11} & U_{12} \\ U_{21} & U_{22} \end{pmatrix} \begin{pmatrix} \psi_{+,i} \\ \psi_{-,i} \end{pmatrix} \quad (2.21)$$

Equation 2.21 demonstrates a straightforward method of constructing the unitary transform matrix. The solution to the coupled ODEs 2.18 for an initially polarized spin-up state  $|\Psi_+\rangle = \begin{pmatrix} 1 \\ 0 \end{pmatrix}$  will yield the matrix elements  $U_{11}, U_{21}$ ; the other two matrix elements are found by solving for initial state  $|\Psi_-\rangle$ .

$$\begin{pmatrix} U_{11} \\ U_{21} \end{pmatrix} = \begin{pmatrix} U_{11} & U_{12} \\ U_{21} & U_{22} \end{pmatrix} \begin{pmatrix} 1 \\ 0 \end{pmatrix} \quad (2.22)$$

$$\begin{pmatrix} U_{12} \\ U_{22} \end{pmatrix} = \begin{pmatrix} U_{11} & U_{12} \\ U_{21} & U_{22} \end{pmatrix} \begin{pmatrix} 0 \\ 1 \end{pmatrix} \quad (2.23)$$

The unitary operator for the spin-flip stages is given by

$$U_{\frac{\pi}{2}} = \begin{pmatrix} [\cos \Omega\tau - i\frac{\omega-\omega_0}{2\Omega} \sin \Omega\tau] e^{i\frac{\omega}{2}\tau} & i\frac{\gamma_n B_1}{2\Omega} \sin \Omega\tau e^{i\frac{\omega}{2}\tau+i\phi} \\ -i\frac{\gamma_n B_1}{2\Omega} \sin \Omega\tau e^{-i\frac{\omega}{2}\tau-i\phi} & [\cos \Omega\tau + i\frac{\omega-\omega_0}{2\Omega} \sin \Omega\tau] e^{i\frac{\omega}{2}\tau} \end{pmatrix} \quad (2.24)$$

The final spinor state for the Ramsey method is built up by multiplying the matrices for the unitary transformations using time ordering  $U_{\frac{\pi}{2},2} U_0 U_{\frac{\pi}{2},1}$ , where the subscripts differentiate between the first (1) and second (2) spin-flips which will have a different phase  $\phi_{1,2}$ . Ensuring the spin-flip pulses are coherent must be controlled by correctly setting the phase,  $\phi$ , at each of the spin-flip stages. For simplicity, it can be assumed that  $\phi_1 = 0$ . The phase for the second pulse is chosen based on the coherence of the transverse field pulses:  $\phi_2$  is the phase which is accumulated by the reference ‘‘clock’’ which applies the spin-flip pulses at frequency  $\omega$ . After an initial spin-flip applied for time  $\tau$  and a free precession period  $T$ , the initial phase for the second pulse which is coherent with the first pulse is  $\phi_2 = \phi_1 + \omega(\tau + T) = \omega(\tau + T)$ . The net unitary operator can be described, using the applied time  $t$  and for initial RF phase  $\phi$ :

$$U_R(\phi_1, t_1; T; \phi_2, t_2) = U_{\frac{\pi}{2}}(\phi_2, t_2) U_0(T) U_{\frac{\pi}{2}}(\phi_1, t_1) \quad (2.25)$$

To determine the probability of a spin flip from an initially polarized state requires calculation of  $|\psi_{-,f}|^2$  using the formalism of equation 2.25 and describing the stages by the effective fields in each as: 1.  $\vec{B} = B_0\hat{z} + B_1(\cos(\omega t)\hat{x} + \sin(\omega t)\hat{y})$  for time  $\tau$ ; 2.  $\vec{B} = B_0\hat{z}$  for time  $T$ ; 3.  $\vec{B} = B_0\hat{z} + B_1(\cos(\omega t)\hat{x} + \sin(\omega t)\hat{y})$  for time  $\tau$ .

$$\begin{pmatrix} \psi_{+,f} \\ \psi_{-,f} \end{pmatrix} = U_R(0, \tau; T; \omega\tau + \omega T, \tau) \begin{pmatrix} 1 \\ 0 \end{pmatrix} \quad (2.26)$$

$$\psi_{-,f} = -i\frac{\gamma B_1}{2\Omega} \sin(\Omega\tau) e^{-i\frac{\omega}{2}\tau - i\frac{\phi}{2}} \quad (2.27)$$

$$\times \left[ 2 \cos(\Omega\tau) \cos\left(\frac{\omega_0 - \omega}{2} T\right) - 2\frac{\omega_0 - \omega}{2\Omega} \sin(\Omega\tau) \sin\left(\frac{\omega_0 - \omega}{2} T\right) \right]$$

The probability of an initially spin-up neutron to be found in the spin-down state after a Ramsey cycle is thus:

$$P_{+\rightarrow-} = |\psi_{-,f}|^2 = \tag{2.28}$$

$$4 \left( \frac{\gamma B_1}{2\Omega} \right)^2 \sin^2(\Omega\tau) \left[ \cos(\Omega\tau) \cos\left(\frac{\omega_0 - \omega}{2}T\right) - \frac{\omega_0 - \omega}{2\Omega} \sin(\Omega\tau) \sin\left(\frac{\omega_0 - \omega}{2}T\right) \right]^2$$

It is prudent to check that in the limit  $T \rightarrow 0$ , this returns to the Rabi equation 2.15. The second term in brackets goes to zero, and the first reduces to  $\cos^2(\Omega\tau)$ . Combined with the  $4 \sin^2(\Omega\tau)$  outside the bracket, this becomes an overall factor of  $\sin^2(2\Omega\tau)$ , and equation 2.28 reduces to the Rabi formula for a spin-flip time of  $2\tau$ . The Ramsey sequence contains two separate  $\pi/2$  spin flips, each for time  $\tau$ , which is equivalent to a single Rabi  $\pi$  flip for time  $2\tau$ , therefore the two agree in the limit  $T \rightarrow 0$ .

There is an overall factor proportional to a single Rabi spin-flip which forms an outer envelope containing higher order oscillations. A conceptual argument can be made that the limit of precision in measuring the resonant frequency is related to the width of the central fringe for each method. It will be shown that the width of central fringes in the Ramsey method is inversely proportional to the free precession time  $T$ , such that the width for the Ramsey method can be made orders of magnitude smaller than the width of the Rabi envelope. This is demonstrated in simulation results shown in figure 2.2, for which the simulation method will be discussed in chapter 3, where increasing the free precession time increases the density of fringes within the Rabi envelope.

Simulated results demonstrate the value of separating the  $\frac{\pi}{2}$  pulses. Both have oscillations inside the Rabi envelope, which has a width  $\approx 4$  Hz. For  $T = 1.8$  s the central peak width decreases by an order of magnitude; typical free precession times for EDM measurements are 100 s - 200 s. The fringes become so close that countermeasures to prevent magnetic field drifts over time must be implemented, and the field must be accurately monitored to make systematic corrections when field deviations are detected.

### **Extracting Resonant Frequency using Ramsey Interferometry**

It was stated without proof that the width of the central fringes are related to the limit of precision in measuring the resonant frequency. Measurements are made in

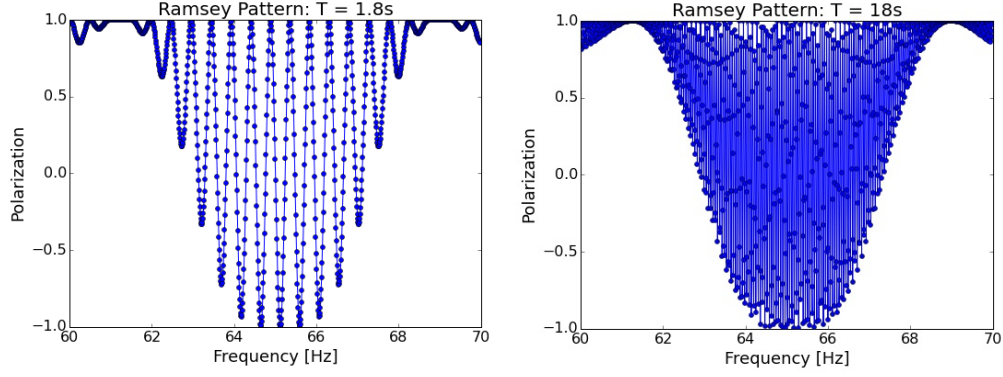


Figure 2.2: Simulated Ramsey fringes for 10mG field with free precession times of  $T = 1.8$  s and  $T = 18$  s.

experiment by counting the neutrons in each spin state for a series of frequencies near half the central fringe, which corresponds to approximately equal probability of spin-up and spin-down. This is the region in which the theoretical probability of spin flip, equation 2.28, is steepest, i.e.-  $\left| \frac{dP}{d\omega} \right|$  is maximal. This is where very small frequency shifts, for example those associated with the electric dipole coupling to the electric field, will result in the greatest shift in the measurable polarization. The narrow fringes in the Ramsey method enable a larger  $\left| \frac{dP}{d\omega} \right|$ , which is desired, relative to the Rabi method. However, other factors play a significant role in this. For example, if a measurement of the Ramsey method is made with free precession time  $T$  long enough that a significant amount of the neutrons depolarize, then it is possible for the Ramsey method to be less effective than the Rabi method. This is because the real magnetic field will not be perfectly uniform as used in the derivation, and the Rabi method requires orders of magnitude less time in the field.

A proper analysis of the precision of the measured frequency should begin with the determination of the resonant frequency. As previously stated, measurements are made at approximately  $\omega_0 \pm \frac{\delta\omega}{2}$ , corresponding to half the central fringe width. The width  $\delta\omega$  is equivalent to the frequency shift between the resonant frequency, where the probability of spin-flip is one, and the nearest frequency at which the probability of a spin flip is zero.  $P_{+\rightarrow-}(\omega = \omega_0 \pm \delta\omega) = 0$  can be determined by equation 2.28 for the region near the central fringe as

$$\cos(\Omega\tau) \cos\left(\frac{\omega_0 - \omega}{2}T\right) = \frac{\omega_0 - \omega}{2\Omega} \sin(\Omega\tau) \sin\left(\frac{\omega_0 - \omega}{2}T\right) \quad (2.29)$$

$$\rightarrow \frac{\Delta\omega}{2\Omega} \tan\left(\frac{\Delta\omega}{2}T\right) = \cot(\Omega\tau) \quad (2.30)$$

An important note on notation:  $\delta\omega$  corresponds to the value of  $\Delta\omega = \omega - \omega_0$  which is equal to the central fringe width at half height. The following equations will use  $\delta\omega$ , as it is the special value for  $\Delta\omega$  near which measurements will be taken. A full analytical solution for  $\delta\omega$  for all values of  $t$  and  $T$  is not available due to discontinuities (poles of  $\pm\infty$ ) in the equation. It is a useful first step to write the factor of  $\gamma B_1$  inside  $\Omega$  in terms of the spin flip time  $\tau$ . For the circular oscillating field used in the derivation, the spin-flip tuning can be determined by considering the Rabi spin-flip probability on resonance from equation 2.15, with  $\omega = \omega_0$ :

$$P_{+\rightarrow-}(t) = \sin^2\left(\frac{\gamma B_1 t}{2}\right) \quad (2.31)$$

For a  $\pi$  flip, this probability is 1, which is achieved for  $\gamma B_1 t = \pi$ . The Ramsey method splits this into two equal  $\pi/2$  pulses, so that the circular field amplitude  $B_1$  tuning for a  $\pi/2$  flip time  $\tau$  is given by

$$2\gamma B_1 \tau = \pi \quad (2.32)$$

This tuning can then be used to simplify  $\Omega\tau$ :

$$\Omega\tau = \frac{\tau}{2} \sqrt{\delta\omega^2 + \gamma^2 B_1^2} = \frac{1}{2} \sqrt{\tau^2 \delta\omega^2 + \frac{\pi^2}{4}} \approx \frac{\pi}{4} \quad (2.33)$$

Here the approximation assumes  $\tau^2 \delta\omega^2 \ll \frac{\pi^2}{4}$ , which is supported by simulation results shown in figure 2.2. This allows extensive simplification, as  $\cot(\Omega\tau) \approx 1$  and  $2\Omega \approx \frac{\pi}{2\tau}$ .

$$\delta\omega = \frac{\pi}{2\tau} \cot\left(\frac{\delta\omega}{2}T\right) \quad (2.34)$$

$\delta\omega$  is expected to be very small, which allows an expansion of the right hand side for  $\cot\left(\frac{\delta\omega}{2}T\right)$  in the region  $\frac{\delta\omega}{2}T \approx \frac{\pi}{2}$ .

$$\cot\left(\frac{\delta\omega}{2}T\right) \approx \frac{\pi}{2} - \frac{\delta\omega}{2}T + O\left(\left(\frac{\pi}{2} - \frac{\delta\omega}{2}T\right)^2\right) \quad (2.35)$$

The resulting approximation to the full width at half maximum, which has been found for  $T > 100$ s to agree with the numerically calculated results to within parts-per-million [23], is given in equation 2.36.

$$\delta\omega = \frac{\pi}{T + 4t/\pi} \quad (2.36)$$

The derivative  $\left| \frac{dP_{+\rightarrow-}}{d\omega} \right|$  is maximized at  $\Delta\omega = \delta\omega/2$ , which sets the target frequencies used in the experiment. Rather than fitting the full Ramsey equation, the limit near the central fringe is used, such that  $\Delta\omega \ll \gamma B_1$  and  $\Omega \approx \gamma B_1/2$ . Also making use of the relation  $\gamma B_1 \tau = \frac{\pi}{2}$ , the probability of a spin flip 2.28 reduces to

$$P_{+\rightarrow-} \approx 4 \sin^2 \left( \frac{\gamma B_1}{2} \tau \right) \cos^2 \left( \frac{\gamma B_1}{2} \tau \right) \cos^2 \left( \frac{\Delta\omega}{2} T \right) = \cos^2 (\pi \Delta\nu T) \quad (2.37)$$

Assuming perfect experimental setup with no losses of neutrons, no loss of polarization, and 100% detection efficiency, the count of neutrons spin-down would be  $N_- = N_0 \cos^2 (\pi \Delta\nu T)$ , where  $N_0$  is the total count of initially spin-up neutrons. Some modifications must be made to this model to account for experimental effects. Depolarization and the analyzer's efficiency at differentiating spin-states can be accounted for by introducing  $N_{\max}$ ,  $N_{\min}$ ,  $\bar{N}$ , and  $\alpha$ .

$$N_{\max} = \epsilon_+ N_0 \quad (2.38)$$

$$N_{\min} = \epsilon_- N_0 \quad (2.39)$$

$$\bar{N} = \frac{N_{\max} + N_{\min}}{2} = \frac{N_0}{2} \quad (2.40)$$

$$\alpha = \frac{\epsilon_+ - \epsilon_-}{\epsilon_+ + \epsilon_-} = \epsilon_+ - \epsilon_- \quad (2.41)$$

$N_{\max}$ ,  $N_{\min}$  correspond to the maximum and minimum counts for the frequency on resonance;  $\bar{N}$  is the average of the two; and  $\epsilon_{\pm}$  refers to the probability that an initially spin-up neutron is counted as either spin-up or spin-down. Note that the cause of mis-counting an initially spin-up neutron as a spin-down (and vice versa) is a combination of the efficiency of the analyzer and the depolarization of the neutrons. Here it is assumed there are no losses, so that  $N_{\max} + N_{\min} = N_0$  and  $\epsilon_+ + \epsilon_- = 1$ . The count of spin-down neutrons then takes the form



$$\begin{aligned}
N_- &= \epsilon_+ N_0 \cos^2(\pi \Delta\nu T) + \epsilon_- N_0 \sin^2(\pi \Delta\nu T) = N_0 \epsilon_- + N_0 \alpha (\epsilon_+ + \epsilon_-) \cos^2(\pi \Delta\nu T) \\
&= \bar{N} [1 + \alpha \cos(2\pi \Delta\nu T)] \quad (2.42)
\end{aligned}$$

$$N_+ + N_- = 1 \quad (2.43)$$

$$N_{\pm} = \bar{N} [1 \mp \alpha \cos(2\pi (\Delta\nu + \nu_d)T)] \quad (2.44)$$

Equation 2.44 is the final form that will be fitted, in which an additional fit parameter  $\nu_d$  has been added to the equation. This term encapsulates any systematic frequency shifts from the Larmor frequency, including the desired shift resulting from a non-zero electric dipole moment. It is important to note this explicit separation of the systematic effects from  $\omega_0$ , which is now only the Larmor frequency due to the applied magnetic field  $|\gamma B_0|$ . The reason for this is that the average magnetic field in the precession chamber will change over time, due to fluctuations in the external background field and potential drifts in the current source for the  $B_0$  magnetic field coil. It takes many runs to accumulate the required statistics, and there must be some way to account for systematic shifts in the frequency when combining these runs. For this reason, co-magnetometers are used to determine the expected Larmor precession due to the magnetic field coupling alone, so that  $\Delta\nu$  is a number known at analysis and only the unaccounted for shift is a fit parameter. Assuming all systematic effects are accounted for, and the only shift from the Larmor frequency is due to the electric dipole moment, the EDM  $d_n$  can be calculated from the difference in the fit parameter  $\nu_d$  extracted from measurements with electric field at  $\pm E$ . Alternatively, the phase shift can be measured at multiple different values of the electric field, then a linear fit can extract  $d_n$ .

$$d_n = \frac{h \Delta\nu_d}{4E} \quad (2.45)$$

## Experimental Sensitivity

Determining the precision with which  $d_n$  can be measured requires an analysis of the error in the frequency shift  $\nu_d$  and the electric field. Assuming the electric field is well understood, its error may be assigned as  $\sigma_E$ . The error in  $\nu_d$  will have two

contributions: the error in the fit  $\sigma_{\nu,f}$ , extracted from the covariance matrix; and the error in frequency assuming the fit were perfect  $\sigma_{\nu,p}$ , resulting from measured uncertainties in the input parameters. The final error is found by adding these two in quadrature:  $\sigma_{\nu}^2 = \sigma_{\nu,f}^2 + \sigma_{\nu,p}^2$ .

Any standard non-linear solver will output a covariance matrix,  $C_{ji}$ ; for the parameter  $\nu_d$  corresponding to the  $k^{\text{th}}$  parameter, the fit error in  $\sigma_{\nu_d}$  is taken as  $\sqrt{C_{kk}}$ . The error in  $\nu_d$  due to the fit,  $\sigma_{\nu,f}$ , follows straightforwardly from error propagation.

$$\sigma_{\nu,f} = \sqrt{C_{kk}} \quad (2.46)$$

The data used to determine  $\nu_d$  is taken from a count of spin-up (down) neutrons given by expression 2.44 at different frequencies near  $\Delta\nu = \pm \frac{\delta\nu}{2}$ .  $\sigma_{\nu,p}$  can be backed out of a calculation for the error propagation for  $N_{\pm}$ , if it is taken as a function of parameters  $\alpha$ ,  $T$ ,  $\bar{N}$  and  $\nu$ .

$$\sigma_N^2 = \left(\frac{\partial N}{\partial \nu}\right)^2 \sigma_{\nu,p}^2 + \left(\frac{\partial N}{\partial T}\right)^2 \sigma_T^2 + \left(\frac{\partial N}{\partial \alpha}\right)^2 \sigma_{\alpha}^2 + \left(\frac{\partial N}{\partial \bar{N}}\right)^2 \sigma_{\bar{N}}^2 \quad (2.47)$$

Using Poisson statistics to determine the error in the counts,  $\sigma_N = \sqrt{N}$ , assuming the  $\sigma_{\nu,p}$  term dominates, and recalling that the frequency is measured at half the central fringe width such that  $2\pi\Delta\nu T = \frac{\delta\omega}{2}T \approx \frac{\pi}{2}$ :

$$N = (2\pi\alpha T \bar{N} \sigma_{\nu,p})^2 \quad (2.48)$$

$$\sigma_{\nu,p} = \frac{1}{2\pi\alpha T \sqrt{\bar{N}}} \quad (2.49)$$

The strength of the Ramsey method comes from the factor of  $\frac{1}{T}$  in the denominator. Larger free precession times enable greater precision in the measurement of  $\nu_d$ , however neutron decay limits the maximum useful  $T \sim \mathcal{O}(100\text{s})$ . The average neutron lifetime in bottle experiments, which is a very suitable value for an EDM experiment using UCNs in a bottle, is 878s based on a recent result from the UCNTau collaboration [24]. Using the relationship between the lifetime  $\tau_n$  and half-life  $t_{1/2} = \tau_n \ln 2$ , this means that half of the initial neutrons are lost within 608s. This excludes neutron losses due to collisions with the wall, which has been measured as  $\approx 10^{-4}$  per wall collision for nickel-phosphorus (NiP) surfaces [25], commonly used for UCN experiments due to its effective Fermi potential  $\sim 213$  neV [25] being suitable for trapping UCNs. For a thorough discussion, see [26]. For  $T \sim 100\text{s}$ , UCNs will

collide with the walls  $\sim 10^3$  times such that approximately 10% of the neutrons which haven't decayed will also be lost. Balancing these loss mechanisms to maximize the statistics  $N$  and the visibility of the fringe  $\alpha$  sets the discussed limits on  $T$ .

Propagating the error in frequency to the electric dipole moment equation 2.45

$$\sigma_d^2 = \frac{h^2}{16} \left[ \frac{\sigma_\nu^2}{E^2} + \frac{\nu_d^2}{E^4} \sigma_E^2 \right] \quad (2.50)$$

In experiments,  $E$  is as large as possible, so that the term proportional to  $E^{-4}$  is much less than the first term. Also assuming the fit error is much less than the error in the experiment parameters yields the common expression for the error in the Ramsey method,  $\sigma_d = \frac{h}{4\pi\alpha TE\sqrt{N}}$ . This indicates that a large electric field is favorable, which is expected based on the desired frequency shift being proportional to the applied field.

## 2.2 Ultracold Neutrons

As demonstrated in the previous section, a long free precession time is necessary for a very sensitive measurement of the frequency. This is one reason why incredibly low energy neutrons, “ultracold neutrons” (UCNs), are beneficial. The energies are so low,  $\mathcal{O}(100 \text{ neV})$ , that the Fermi potential of many materials is sufficiently high that the neutrons are totally internally reflected at all incident angles: UCNs can be bottled and stored for 100's of seconds. In comparison, consider an example of a beam of UCNs with velocity  $\approx 10 \text{ m/s}$ : this would require an experimental apparatus  $\sim 1 \text{ km}$  long to allow the beam to travel for the equivalent free precession time. This reductio ad absurdum argument demonstrates why bottling UCNs is so effective: the time available for phase to accumulate from a potential UCN is several orders of magnitude larger than for beams. Additionally, systematic effects caused by field gradients, as discussed in 2.3, are reduced due to the lower velocities of UCNs.

The downside of using UCNs is the substantial drop in statistics. Neutrons are produced by removing them from heavy nuclei, which is highly dependent on the process but typically produces neutrons with energies on the order of the nuclear binding energies  $\sim \text{MeV}$ . Moderation and downscattering is required to decrease the energy, but neutrons are lost in the process. Upgrades to the LANL UCN source has increased UCN production by an order of magnitude in the last decade [27], as shown in figure 2.3.

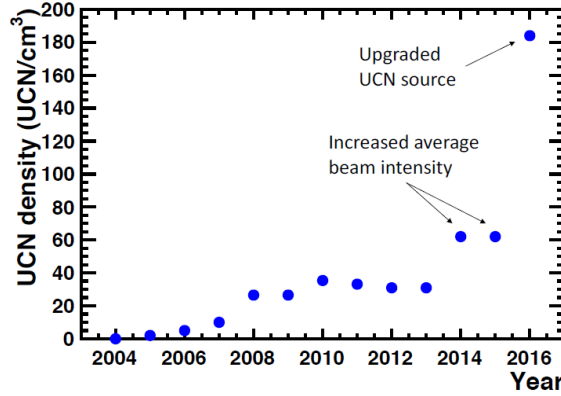


Figure 2.3: UCN production density at the ultracold neutron source at LANSCE as measured using the same apparatus as a function of year [27].

### UCN Properties

Most generally, UCNs could be described as neutrons with energies low enough that they can be stored inside material containers. This corresponds to energies  $\leq 300$  neV, the approximate maximum Fermi potentials of most materials. The corresponding wavelengths of UCNs is greater than 50 nm; as a result, interactions with the atoms which makeup materials can be approximated by an effective constant, complex potential,  $V_F = V + iW$ , called the Fermi potential. For a thorough review of UCN interactions with materials, see [26].

Translating this kinetic energy into a velocity via  $\frac{1}{2}m_n v^2 = 300$  neV, using the neutron mass of  $\sim 939$  MeV/ $c^2$  corresponds to a maximum velocity  $\sim 7.6$  m/s. Interestingly, UCNs can be contained in an open-top bottle: the potential energy due to gravity  $PE = mgh \sim 102$  neV/m, for acceleration due to gravity  $g \sim 9.8$  m/s. This implies that UCNs cannot escape vertically through an open container  $\sim 3$  meters high. Gravitational traps can be useful for reducing the number of wall interactions.

A very beneficial property related to UCNs is the energy shift due to the coupling of the magnetic moment to magnetic fields,  $E_{\pm} = \mp \frac{\hbar}{2} \gamma B$ , where the subscript  $+(-)$  corresponds to the spin-up (down) state. Using the values of Planck's constant  $\hbar \approx 6.582 \times 10^{-16}$  eV·s and the neutron gyromagnetic ratio  $\gamma \approx 1.832 \times 10^8$  T $^{-1}$  s $^{-1}$ , the resulting energy shift of a neutron in a magnetic field is  $\Delta E \approx \mp 60.3$  neV / T. Dependent on the direction of the magnetic field, one spin-state of UCNs can almost completely be rejected by a magnetic field  $\sim 5$  Tesla, and the other spin-state is passed through with an energy boost. Very high polarizations can be achieved using this method. The magnetic interaction is also being used in a novel bottling

technique by the UCNTau collaboration to reduce the effects of wall collisions [24].

## UCN Production

To produce ultracold neutrons, it is first necessary to produce many neutrons. This is typically done using spallation sources, in which heavy nuclei are bombarded with high energy protons from an accelerator. The Spallation Neutron Source at Oak Ridge National Lab uses mercury as its target, whereas the UCN source at LANSCE uses tungsten. Spallation is a process similar yet different to fission: energy is absorbed by incident particles in each. In fission, the result is the splitting of the nucleus, with the release of only a few neutrons. For spallation, the nucleus is excited with a cascade of hadrons being produced. As the nucleus relaxes, it “evaporates” neutrons (and other hadrons), producing  $\sim 5\text{-}6\times$  more neutrons, with  $\sim 1/6$  the energy from a similar fission reaction [28]. The increase in neutrons makes spallation favorable as a source, and the lower energy is also preferable for producing low energy neutrons.

The LANSCE UCN source, as shown in figure 2.4, uses beryllium and graphite as moderators to initially decrease neutron energies. Then, the neutrons pass through a layer of polyethylene beads cooled to 45 K. Finally, UCNs are produced by down-scattering phonon collisions through a volume of solid deuterium at 5 K. UCNs pass through the  $\text{SD}_2$ , and pass to the exit guides with the help of a mechanical flapper to prevent falling back into the moderator [27]. Preventing the UCNs from falling back into the moderator is essential, as the UCN lifetime in  $\text{SD}_2$  has been measured to be  $\sim 1.5$  ms [29]. From here, NiP coated pipes guide the UCNs into the experiment hall, where they are routed to different experiments.

### 2.3 Gradient Field Effects

Magnetic field gradients are problematic in high precision measurements of neutron spin precession. Though the magnetic field does not appear explicitly in the result for the electric dipole moment, and also is not present in the error, its effects can be seen implicitly. In a perfect environment free of all background magnetic fields, then the polarization of the neutrons could be maintained and the precession frequency determined exclusively by the electric field coupling to the electric dipole moment as shown in equation 2.2. However, there is a balance between the environment we can feasibly achieve with the requirements of the experiment. Typical wall collisions will depolarize or absorb neutrons at a rate of  $\approx 10^{-4}$  per collision, and we want as large a free precession time as possible. We can either decrease the precession time, or build

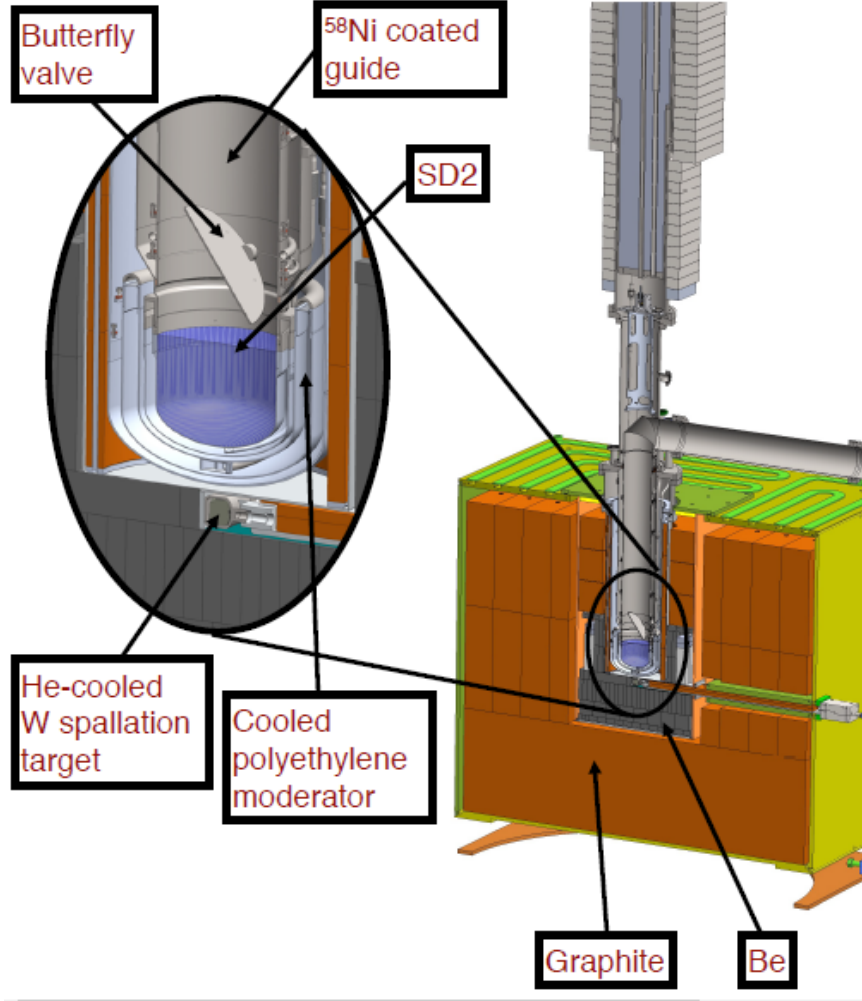


Figure 2.4: Schematic diagram of the ultracold neutron source at LANSCE [27].

the chamber larger. A larger chamber means we need a larger magnetically shielded room, which is already expensive due to the highly magnetic permeable materials from which it must be constructed. These are the types of trade-offs that must be made, and this particular trade-off means that typical background magnetic fields inside the shield are  $\sim 1$  nT. This sets the order of magnitude for the  $B_0$  field, which must be significantly greater than the background to maintain polarization of the neutron spin.

This holding field will have gradients, and as a result an ensemble of neutrons sampling different phase-space will eventually depolarize. The fit parameter  $\alpha$  from equation 2.44 is implicitly linked to the transverse spin relaxation,  $T_2$ . Parameters  $N_{\max}$ ,  $N_{\min}$  referred to the expected counts of spin-down and spin-up neutrons on the resonant frequency. Consider the case of a perfect analyzer which is 100% efficient at

counting spin-up or spin-down correctly, used in a Ramsey cycle measurement of an initial group of 3 spin-up and 1 spin-down neutrons,  $N_0 = 4$ , in perfect magnetic fields. On resonance, a perfect analyzer would detect 1 spin-up and 3 spin-down neutrons, that is  $N_{\max} = 3$  and  $N_{\min} = 1$ . This would correspond to  $\alpha = 0.5$ , which decreases the sensitivity in measuring  $d_n$  by a factor of two. A similar effect will occur if there is an initially 100% polarized sample which depolarizes during free precession, which will present as a reduction in the visibility,  $\alpha$ . In addition to this, the interference between magnetic field gradients with motional magnetic fields induced by motion through an electric field produces a systematic effect which mimics an electric dipole moment.

### Spin Relaxation

Consider two UCNs with the exact same spin state. Over some period of time, if they experience the same magnetic fields with no other interactions, then they will have the same final spin state. If they both experience constant magnetic fields which differ, for example by 1%, then the precession frequencies will differ by 1% and they will only periodically have the same polarization at later times. There will always be some inhomogeneity in the magnetic fields which will cause variations in the average sampled field. In reality, it is more complex than this example which only considers a single component of the field. It is thus essential to characterize the spin relaxation of the experiment setup, a property defined as the time in which the ensemble depolarizes. There are two flavors of spin relaxation:  $T_1$ , commonly called the longitudinal spin relaxation because it is the depolarization time for an ensemble initially polarized along the nominal field vector; and  $T_2$ , labeled the transverse spin relaxation because the initial polarization is in the plane perpendicular to the nominal field vector.

For the case of a longitudinally polarized neutron, i.e.,  $\langle \vec{S} \rangle = \frac{\hbar}{2} \hat{z}$ , it is the transverse components of the magnetic field,  $\vec{B}_\perp = B_x \hat{x} + B_y \hat{y}$  which cause depolarization. As a thought exercise, consider a field which has spatial or time variations in the longitudinal component and zero transverse components  $\vec{B} = B(\vec{r}, t) \hat{z}$  (as a thought exercise only; such a field clearly does not obey Maxwell's equations). In the  $S_z$  basis, longitudinal polarization corresponds to a spinor of the form  $\psi = \begin{pmatrix} e^{i\phi} \\ 0 \end{pmatrix}$ , with phase  $\phi$  not observable in  $\langle \vec{S}_z \rangle$ . The Schrödinger equation in this case has no mixing of the up and down components of the spinor.

$$i\hbar\dot{\psi} = -\frac{\hbar\gamma B_z(\vec{r}, t)}{2} \begin{pmatrix} 1 & 0 \\ 0 & -1 \end{pmatrix} \psi \quad (2.51)$$

$$\begin{pmatrix} \dot{\psi}_+ \\ \dot{\psi}_- \end{pmatrix} = i\gamma B_z \begin{pmatrix} \psi_+ \\ \psi_- \end{pmatrix} \quad (2.52)$$

$$\langle \sigma_z(t) \rangle = \begin{pmatrix} e^{(-i\gamma B_z t + \phi_0)} & 0 \\ 0 & -1 \end{pmatrix} \begin{pmatrix} 1 & 0 \\ 0 & -1 \end{pmatrix} \begin{pmatrix} e^{(i\gamma B_z t + \phi_0)} \\ 0 \end{pmatrix} = 1 \quad (2.53)$$

In this thought exercise, the only time dependence is in the phase  $\phi$  which is not observable, and so the expectation value  $\langle S_z \rangle$  is unchanged. This indicates that it is the transverse fields which will cause longitudinal depolarization.

The transverse spin relaxation is more complicated. Consider an ensemble of neutrons with initial polarization  $\langle \vec{S} \rangle = \frac{\hbar}{2} \hat{x}$ , corresponding to spinor  $\psi = \begin{pmatrix} 1 \\ 1 \end{pmatrix} / \sqrt{2}$ , in the non-physical field used in the previous thought exercise. An individual in this ensemble will experience some time dependent magnetic field  $B(\vec{r}_j, t_j)$ , which will differ depending on the phase space sampled by each individual neutron resulting in different precession frequencies,  $\omega_j$ . Consequently, the neutrons will dephase in the  $xy$  plane over time, dependent on how much the field varies for the parameter space sampled. Thus, variance in the longitudinal component of the magnetic field causes transverse spin depolarization.

The addition of transverse magnetic field components introduces mixing of the up and down states. For a constant transverse component, e.g.,  $\vec{B} = B_x \hat{x} + B_z \hat{z}$ , the polarization vector will precess about the net magnetic field vector. For a time-dependent transverse field, the polarization will tip as studied in section 2.1. Gradients in the magnetic field will cause spatial variations in the field which will appear as time dependent fields due to the neutron's motion. Depolarization is thus a complex relationship between the magnetic field and the phase space, often studied analytically by correlation functions  $S_{i,j} = \int_0^\infty e^{i\omega\tau} \langle \vec{B}_i(0) \cdot \vec{B}_j(\tau) \rangle$  [30], see also [31], [32]. Typical solutions are solved for special cases, e.g., ballistic or diffusive motion using a simple field  $\vec{B} = (B_0 + G_z z) \hat{z} - G_z \frac{\rho}{2} \hat{\rho}$  with  $G_z = \frac{dB_z}{dz} = \text{constant}$ . Using solutions to the equations of motion with some simple field profile allows for the correlation functions to be solved by writing the fields as a function of the position and velocity, using analytical models of the motion.

While many of the analytical solutions fit observations very well, the approximations break down in the case of larger experimental regions, where higher order terms



in the magnetic field become more prevalent. In these cases, it is appropriate to use Monte Carlo simulations of the phase space to study the spin dynamics with high accuracy as in chapter 3.

### False EDM due to Geometric Phase

When measuring an observable which is theoretically predicted to be miniscule, identification of any systematic effects which are comparable in size is essential. Any effect which is linearly proportional to the electric field is especially significant, because it would be interpreted as an electric dipole moment. There is such an effect, which is the result of interference between gradients in the magnetic field and the motion through an electric field.

Under special relativity, electromagnetic fields transform such that the component parallel to the relative velocity between the frames is unchanged, but the components perpendicular to the boost are

$$\vec{E}'_{\perp} = \gamma_r \left( \vec{E}_{\perp} + \vec{v} \times \vec{B} \right) \quad (2.54)$$

$$\vec{B}'_{\perp} = \gamma_r \left( \vec{B}_{\perp} - \frac{\vec{v} \times \vec{E}}{c^2} \right) \quad (2.55)$$

The relativistic effects are considerable for beam neutron experiments, but for ultracold neutrons the Lorentz factor  $\gamma_r \approx 1$  and  $v/c \approx 10^{-8}$ , which led to this largely being disregarded in early UCN experiments. As such, the motional contribution,  $\vec{B}_v = \frac{\vec{E} \times \vec{v}}{c^2}$ , is much smaller than the nominal field  $B_0$ , however it may be comparable to the transverse components which are typically orders of magnitude smaller than  $B_0$ . The most general spin precession frequency is given by  $\omega_0 = \gamma_n |\vec{B}|$ . Assuming the transverse fields are much smaller than the nominal magnetic field, the effective frequency shift caused by  $B_v$  can be estimated by an evaluation of the magnitude of the field.

$$\left| \vec{B}_0 + \vec{B}_v \right| = \sqrt{B_0^2 + B_v^2 + 2\vec{B}_0 \cdot \vec{B}_v} \approx |B_0| + \frac{1}{2|B_0|} \left( \gamma_r \frac{\vec{v} \times \vec{E}}{c^2} \right)^2 - \gamma_r \frac{\vec{B}_0 \cdot \vec{v} \times \vec{E}}{|B_0| c^2} \quad (2.56)$$

The  $E^2$  term will not contribute to a false EDM, but the term linear in E will clearly result in a false EDM at the level of individual neutrons. This is a small perturbation, so that it is safe to approximate  $\vec{E} = E\hat{z}$ , and as such the false EDM is

only dependent on the transverse components of  $\vec{B}_0$  and  $\vec{v}$ :  $\vec{B} \cdot \vec{v} \times \vec{E} = \vec{E} \cdot \vec{B} \times \vec{v} = E(B_x v_y - B_y v_x)$ . Conceptually, one might assume that once the neutrons are isotropic inside the storage chamber, the contributions of neutrons with  $\vec{v}$  would be canceled by those with  $-\vec{v}$ , so that this effect may not be seen in the ensemble result. It will be shown that this assumption does not hold true.

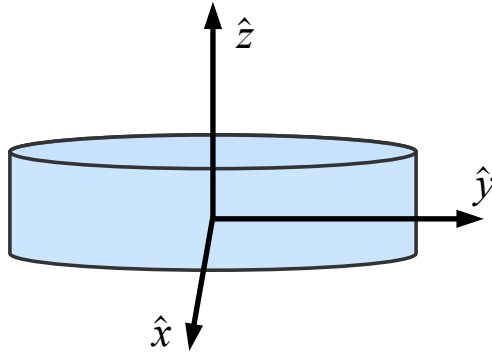


Figure 2.5: Coordinate system for a cylindrical bottle. For the methods introduced in this chapter and used in the proceeding chapters, the nominal  $B_0$  field is oriented with the  $z$ -axis (longitudinal), and the transverse oscillating fields used to flip the spins are in the  $xy$  plane. The electric field will be parallel or anti-parallel to the  $B_0$  field.

A derivation of the Ramsey-Bloch-Siegert shift [33] is beneficial to calculate the ensemble effect on the resonant frequency. Assuming, for simplicity, that the neutrons in a cylindrical chamber follow approximately circular paths in the  $x-y$  plane (which, as shown above, are the only components of velocity to contribute significantly to this false EDM), define the frequency which a particular neutron circles as  $\omega_c$ . Using the notation  $\omega_0 = \gamma_g B_0$  and  $\omega_{xy} = \gamma_g B_{xy}$ , the resonant frequency in a frame rotating at  $\omega_c$ , related to the resonant frequency in the stationary frame  $\omega$  via  $\omega = \omega' + \omega_c$ , is given by

$$\omega' = \gamma_g B_{ef} = \sqrt{(\omega_0 - \omega_c)^2 + \omega_{xy}^2} \quad (2.57)$$

where the “effective” magnetic field along  $\hat{z}$  is the result of some pseudo field  $B_c = \frac{\omega_c}{\gamma_g}$ . In the limit  $\omega_0 - \omega \gg \omega_{xy}$ , the resonant frequency in the rotating frame is found to be

$$\omega' \approx (\omega_0 - \omega_c) \left[ 1 + \frac{\omega_{xy}^2}{2(\omega_0 - \omega_c)^2} \right] \quad (2.58)$$

and the resonant frequency in the non-rotating frame is

$$\omega = \omega_0 + \frac{\omega_{xy}^2}{2(\omega_0 - \omega_c)} \quad (2.59)$$

The resulting frequency shift is known as the Ramsey-Bloch-Siegert (RBS) shift [33], equation 2.60, the starting point for a derivation by Pendlebury et al. [34] to analytically quantify this false EDM effect.

$$\Delta\omega = \frac{\omega_{xy}^2}{2(\omega_0 - \omega_c)} \quad (2.60)$$

The factor in the denominator indicates a resonance dependent on the phase-space of the neutrons relative to the spin frequency due to the nominal  $B_0$ . The numerator is dependent on the transverse velocities of the neutron and transverse components of the magnetic field, including the motional field  $B_v$ . Neglecting background fields, the transverse components of the magnetic field is directly related to the gradients in the  $B_0$  coil. Assuming a constant gradient,  $\vec{B}_{xy} = (\gamma_r \frac{\vec{E} \times \vec{v}}{c^2} - \frac{\rho}{2} \frac{\partial B_{0z}}{\partial z}) \hat{\rho}$ . Using for shorthand notation  $G_z = -\frac{\partial B_{0z}}{\partial z}$ :

$$\omega_{xy}^2 = \gamma_g^2 \left[ G_z^2 \frac{\rho^2}{4} + \left( \gamma_r \frac{\vec{E} \times \vec{v}}{c^2} \right)^2 + G_z \rho \gamma_r \frac{\vec{E} \times \vec{v}}{c^2} \right] \quad (2.61)$$

Considering the cumulative effect on an isotropic ensemble in circular orbits with equal probability  $\vec{v} = \pm v_\phi \hat{\phi}$  with a corresponding sign-flip in  $\omega_c$  and  $\omega_{xy\pm}^2$  where the sign in the subscript corresponds to the sign of the velocity, the RBS shift becomes

$$\Delta\omega = \frac{\omega_{xy+}^2}{4(\omega_0 - |\omega_c|)} + \frac{\omega_{xy-}^2}{4(\omega_0 + |\omega_c|)} \quad (2.62)$$

Consider the difference between this phase shift for a sign change in the electric field, denoted  $\Delta\omega_{\uparrow\uparrow} - \Delta\omega_{\uparrow\downarrow}$ , where the first arrow indicates the direction of the magnetic field and the second the electric field. Any non-zero result would present as a systematic effect, but not necessarily a false EDM which must be explicitly linear in the electric field. The first two terms in  $\omega_{xy}^2$  clearly cancel, being dependent on  $B$  and  $E^2$ , neither of which change under the exchange  $E \rightarrow -E$ .

$$\begin{aligned} \Delta\omega_{\uparrow\uparrow} - \Delta\omega_{\uparrow\downarrow} &= \frac{\gamma_n^2 \gamma_r v_\phi E \delta B_0}{2c^2} \left[ \frac{1}{\omega_0 - |\omega_c|} - \frac{1}{\omega_0 + |\omega_c|} \right] \\ &= -E \left( \frac{\partial B_{0z}}{\partial z} \right) \frac{\gamma_n^2 \gamma_r v_\phi \rho |\omega_c|}{2c^2 (\omega_0^2 - \omega_c^2)} \end{aligned} \quad (2.63)$$

Equation 2.63 indicates that there is a frequency shift for the ensemble of neutrons which does not cancel when considering the direction of the orbits within the cylindrical chamber. The full form of the false EDM is dependent on the phase-space factor  $\frac{v_\phi \rho |\omega_c|}{(\omega_0^2 - \omega_c^2)}$ , which Pendlebury et al. calculated for several cases [34]. Later papers have used the method of correlation functions as briefly discussed in the spin-relaxation section to calculate the false EDM [30].

To leading order, the false EDM is dependent on  $\frac{\partial B_{0z}}{\partial z}$ , which is used as a key metric in optimization of magnetic field profiles introduced in chapter 4. Great minds have put forth substantial effort to derive analytical forms of this effect, but the solutions are largely limited to special cases, low order expansions of magnetic fields, and assumptions for the storage chamber geometry as used in the presented derivation. As suppression of higher order terms in the false EDM effect enter the discussion, it will become necessary to utilize numerical studies of this frequency shift to assist in the optimization of magnetic field profiles.

## Chapter 3 LANL nEDM Simulation

To better understand expected systematic effects for the room-temperature LANL nEDM experiment, a Monte Carlo simulation was developed in C++, with an emphasis on modeling the fields as accurately as possible. The experiment uses the Ramsey method of separated oscillatory fields as discussed in chapter 2. UCNs will be guided from the source into two cylindrical chambers. Since the chambers are identical and symmetrically displaced about the center of the cylindrical solenoid, the simulation only considers a single chamber. Note that, because of the height difference of the UCNs between the two chambers, there will be a small shift in the energy spectra of UCNs. A full analysis of the UCN energy spectrum at some standard input guide height must be conducted to fully model the experiment. Then the difference in the top and bottom cells can be simulated by shifting the minimum and maximum velocities in the simulated neutron event generator.

A  $^{199}\text{Hg}$  co-magnetometer is present within the chamber. Once the chamber is filled, two separate time-dependent  $B_{\text{RF}}^{(\text{n,Hg})}$  pulses are applied for a period  $t_{\text{RF}}^{(\text{n,Hg})}$  at frequencies to rotate the spins for neutrons and Hg, respectively, into the plane transverse to the magnetic holding field (a  $\frac{\pi}{2}$  spin-flip). The gyromagnetic ratios of the neutron and  $^{199}\text{Hg}$  differ enough that separate pulses can be applied with minimal effect on the polarization of the other ( $1.83 \times 10^8 \text{ T}^{-1} \text{ s}^{-1}$  and  $4.77 \times 10^7 \text{ T}^{-1} \text{ s}^{-1}$ , respectively [35]). The particles then freely precess for a time period  $T$  on the  $\mathcal{O}(100\text{s})$  in the  $B_0$  field. Finally, a third  $\frac{\pi}{2}$  pulse is applied to rotate the UCNs anti-parallel to the original polarization vector. The chambers are then emptied and the UCNs directed to a spin analyzer to count the number of up and down spins. The simulation has built-in compatibility to simulate neutrons and  $^{199}\text{Hg}$  (or any fermion), but for the study presented here, only neutrons were considered.

### 3.1 General Simulation Methods

In the simulation of the Ramsey sequence which I developed, the UCN guide is not modeled; therefore particles are generated randomly on a thin disk just inside the cylinder wall at the location where the guide will connect to the chamber. This simplification is used so that a simpler method of detecting wall collisions may be used, in which the radius and height is checked against the radius and bottom/top of the virtual cell. The initial momentum is set as a unit vector, randomly distributed

within a hemisphere oriented normal to the cylinder wall pointing inward. The vector components are then scaled with a magnitude sampled from a  $P(v) \propto v^2$  distribution, up to a typical maximum  $v_{\max} = 7$  m/s. The expected number density for particles is  $O(10^2 \text{ cm}^{-3})$  for UCNs and  $O(10^{10} \text{ cm}^{-3})$  for Hg. Both of these number densities are sufficiently low that the motion is effectively ballistic following kinematic equations, where  $g = 9.807 \text{ m/s}^2$  is the acceleration due to gravity.

$$\vec{r}(t + \Delta t) = \vec{r}(t) + \dot{\vec{r}}(t)\Delta t + \ddot{\vec{r}}\frac{\Delta t^2}{2} \quad (3.1)$$

$$\dot{\vec{r}}(t + \Delta t) = \dot{\vec{r}}(t) + \ddot{\vec{r}}\Delta t \quad (3.2)$$

$$\ddot{\vec{r}} = -g\hat{z} \quad (3.3)$$

Movement through the chamber will be solved exactly at each integration step using the kinematics equation for the integrated time  $\Delta t$ , with gravity being the only present force. Reflections are considered mostly specular, with some percentage of non-specular reflections with given probability and angles determined by the method of Steyerl et al. [36]. Spins are treated as 4 numbers: real and imaginary components each of the up and down spinors in the z-basis. They obey the Schrödinger equation, and the full spinor is normalized at each step. All random number generation is performed by the xor4096 algorithm by R. P. Brent [37], a pseudo-random number generator (RNG) which is widely available and passes the “Big Crush” test of randomness.

### Bulirsch-Stoer ODE Integrator

The time-dependence of the spin requires a differential equation integrator for each step made in time. The simplest is the Euler method:  $y(t + H) \approx y(t) + \frac{dy(t)}{dt}H$ . The accuracy is highly dependent on the step-size  $H$ , thus the first improvement is to divide  $H$  into  $n$  sub-steps of size  $h = H/n$ . The Runge-Kutta algorithms of different order are one of several types of algorithms which use some type of sub-step methodology to improve the accuracy of the integration over a single integration iteration. One improvement that can be made is to take measurements using increasing number of sub-steps  $n$ , then extrapolate the results to the limit  $n \rightarrow \infty; h \rightarrow 0$ . This is the general idea for the Bulirsh-Stoer algorithm [38]. It is beneficial to use the modified midpoint method for each set  $n$ , as the error expressed as a power series in  $h$  contains only even powers of  $h$ . The Runge-Kutta methods to  $O(n)$  have error to  $O(h^{n+1})$ , e.g.,

RK4 has error  $O(h^5)$  and requires 4 calculations of the derivative. Using the same number of function calls it is possible to run the modified midpoint method multiple times by re-using the initial derivative to run the set  $n = 2, 3$ . Neville's algorithm is used to perform polynomial extrapolation after each order in  $n$  to estimate the integral. An additional benefit of extrapolation is that a result is obtained after each extrapolation of order  $n$ , which can be compared with the previous extrapolation to give an error approximation. This error estimate is used for the adaptive step-size controller to determine whether the next time step should be larger or smaller, using the Deuffhard method [39].

## Reflections

Wall collisions are handled in a simple and efficient manner. The geometry of the storage chamber is a cylinder, which makes checking for the occurrence of a wall collision a matter of checking whether the height  $z$  is above or below the top or bottom of the chamber and if  $x^2 + y^2 > \rho_{\text{cell}}^2$ . Before each integration step, this check is made for the current time-step setting; if a collision is expected, the kinematic equations are used to set a time-step which will take the neutron exactly to the wall. After the integration step, the default time-step is restored and the velocity vector is rotated to model either specular or non-specular reflection.

The method of Steyerl et al. is used with Monte Carlo acceptance / rejection to determine the angle of reflection [36]. A height correlation function is required to model the roughness of a surface. One of the more common models is a Gaussian.

$$f_G(\delta) = b^2 \exp \left[ -\frac{\delta^2}{2w^2} \right] \quad (3.4)$$

where  $b^2$ , the mean square roughness, and  $w$ , long-range cutoff, quantify the roughness and  $\delta$  is the displacement from center of the Gaussian. The height correlation function defines a potential at the boundary of a vacuum with a smooth, flat surface of constant potential. Perturbation theory is used, assuming elastic scattering, to calculate the reflected wave function for a wave incident from the vacuum side,  $\psi_{in} = \exp \left( i\vec{k}_{in} \cdot \vec{r} \right)$ . From this, the probability of non-specular reflection excluding wall-losses may be determined:

$$P_{NS} = \frac{4k^4 b^2 w^2}{2\pi} \cos(\theta_i) \cos(\theta)^2 \exp \left[ -\frac{q^2 w^2}{2} \right] \quad (3.5)$$

where  $\vec{q}$  is the *in-plane* momentum transfer (i.e. - the plane defined by the normal to the wall surface; recall this is elastic scattering so that  $\|\vec{k}\|$  is conserved) and is a

function of the incident and reflected angles. Here  $\theta$  is defined relative to the normal pointing inward from the surface, and  $\phi$  is an angle of rotation about the normal relative to incidence with  $\phi = 0$  defined such that the tangential component changes only in magnitude, not direction. The method of acceptance / rejection is used to determine non-specularity: the reflected angles  $\theta \in (0, \pi)$  and  $\phi \in (0, 2\pi)$  and a total probability  $P \in (0, 1)$  are each randomly selected from the RNG. The angles are inserted into 3.5: if  $P < P_{NS}(\theta, \phi)$  then these are the reflected angles; else the reflection is specular.

It is important to note that the position distribution of the particles is highly dependent on the amount of non-specular reflections. Unfortunately, the roughness parameters are generally not well understood, especially the long-range cutoff  $w$ . The roughness  $b$  is better known, and depending on the finishing method typically falls between 10-50Å for highly polished surfaces [36]. Inhomogeneous distribution of neutrons within the storage chamber has an effect on the accuracy of the comagnetometer determination of the leading order resonance  $\nu_0$  in equation 2.44. The average resonant frequency is determined by the average field sampled by the ensemble of neutrons, which clearly does not correspond to an unweighted geometric average. This must be corrected in analysis, which will benefit from an accurate model of the wall collisions.

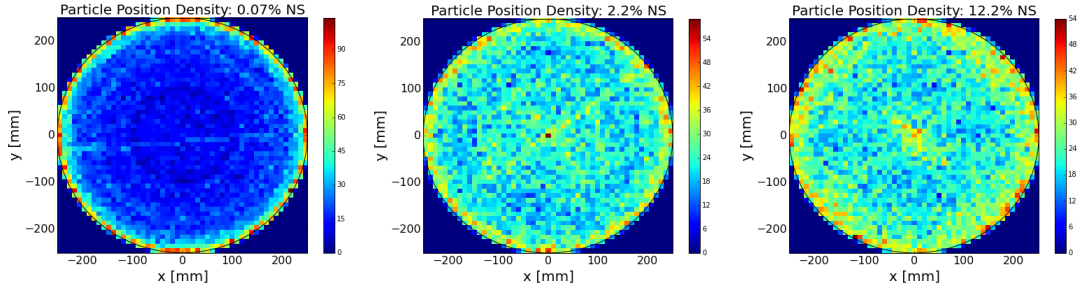


Figure 3.1: Position distribution in  $xy$  plane for different percentage of non-specular reflection: (a) 0.07%; (b) 2.2%; (c) 12.2%.

The figures 3.1 are for identical physical parameters, and the degree of non-specularity purely comes from changes to the roughness parameters  $b, w$ . Near 100% specular reflections results in particles spending more time near the outer edges of the container. The explanation is simple: every particle interacts with the walls regularly, occupying a region from the radius of the wall to some minimum radius greater than zero. Introducing any degree of non-specularity results in three regions in the  $xy$  plane, as seen in figures 3.1b and 3.1c: a “core”, a “mantle”, and a “crust”.



The core and crust occupy the center and outer edges respectively, and generally have approximately twice the particle density of the mantle. As shown in figure 3.2, specular reflections result in regular, repeating orbits, which by the previous explanation describes the crust and mantle regions. The core is an interesting result of the occasional non-specular reflection. The regular, specular orbits in general avoid the center, and the probability of a particle being initialized with momentum carrying it through the center of the chamber is very small. However, the  $\cos^2 \theta$  dependence on the probability of non-specular reflection favors reflected trajectories towards the center. This result can have a big impact on systematics and potentially on magnetic field profile design. Mostly specular reflections results in each neutron sampling a limited phase-space. Non-specularity introduces occasional changes to the phase space which results in differences in the average magnetic field which is sampled. A comparison of the results for spin relaxation dramatically demonstrates this effect in section 3.4.

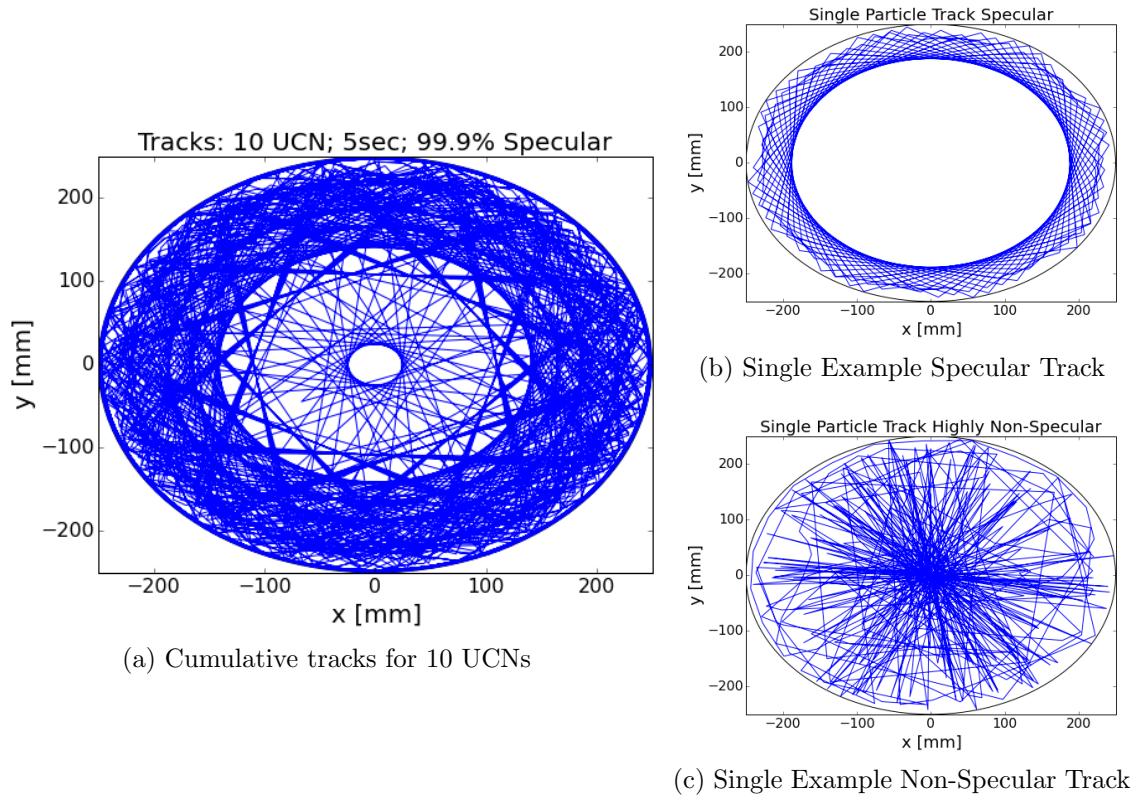


Figure 3.2: Tracks over 5 second period comparing specular and non-specular reflection. Specular reflections result in regular, repeating tracks which avoid the center. Non-specular reflections result in an increase in particle density near the center.

### 3.2 Spin Tracking

Spins are treated quantum mechanically in the  $S_z$  basis, in which the  $z$ -axis is aligned axially with the cylinder length and parallel to the nominal magnetic field  $\vec{B}_0$ , and the  $x, y$  axes define the radial plane. A spinor composed of two complex numbers, decomposed into 4 real numbers, represents the spin state:

$$\Psi = \begin{pmatrix} \psi_u^r + i\psi_u^i \\ \psi_d^r + i\psi_d^i \end{pmatrix} \quad (3.6)$$

Initial polarization is along  $+\hat{z}$ ,  $\Psi = \begin{pmatrix} 1 \\ 0 \end{pmatrix}$ . The time-dependence of the spin is given by the Schrödinger equation:

$$i\hbar \frac{d\Psi}{dt} = H\Psi = -\vec{\mu} \cdot \vec{B}\Psi = \gamma \vec{S} \cdot \vec{B}\Psi = \frac{\hbar}{2} \gamma \vec{\sigma} \cdot \vec{B}\Psi \quad (3.7)$$

where  $\gamma$  is the gyromagnetic ratio and  $\vec{\sigma} = \sigma_x \hat{x} + \sigma_y \hat{y} + \sigma_z \hat{z}$  is the vector of Pauli matrices.

Equation 3.7 is the differential equation which is being integrated by the Bulirsch-Stoer algorithm. This general form is used; any magnetic field gradients and the motional term  $\propto \vec{v} \times \vec{E}$  are included in a total magnetic field  $\vec{B}$ . As a result, the position and velocity must be inputs for the differential equation. Integration is performed with increasing sub-steps  $n$  for a single time step until the maximum error per step (EPS) is achieved. The position and velocity are then set to the new values from kinematics and the resultant spin state is normalized.

Standard validation tests included velocity and position initialization histograms, and monitoring longitudinal and transverse polarizations as a function of time for the perfectly uniform field case. Testing the effects of gradients to confirm correct function is more difficult to test, as an analytical solution must exist which closely fits the parameters of the test.

The accuracy of this integrator has been validated by several test cases. First, validation was performed using neutrons polarized parallel and perpendicular to a perfectly constant magnetic field; with expected results that the polarization remain constant, and precessed at constant frequency respectively, were obtained. Additional tests included comparison of spin relaxation time results compared with some analytical approximations.

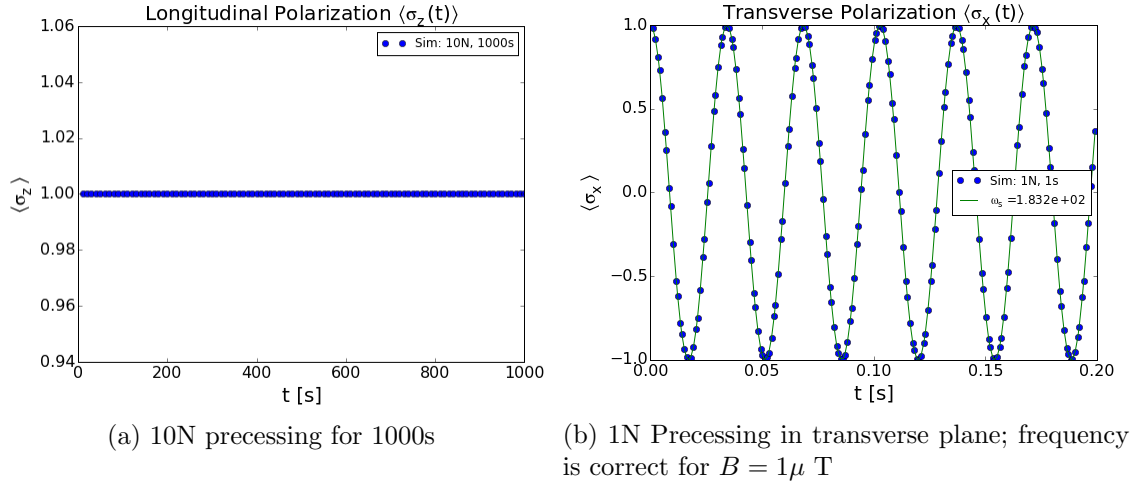


Figure 3.3: Testing the precession within a constant magnetic field.

### 3.3 Magnetic Field Modeling

A key goal of this simulation is to accurately model the spin precession in a realistic magnetic field. Two methods were included to execute this goal: trilinear interpolation of an input field map; and a polynomial approximation of the field. The polynomial approximation is more computationally efficient, and also can have accuracy advantages over the interpolation method, which assumes the field changes linearly within each sub-cube.

#### Map Interpolation

This method starts by outputting a field map in 1 mm increments for the fiducial volume into either a tab-delimited text file or binary. Using binary is faster and decreases the file size, though the latter is still  $O(1GB)$ . The map is loaded into a global hash table, that is a list of arrays with a unique index corresponding to each vertex, each containing only the magnetic field components  $B_x$ ,  $B_y$ , and  $B_z$ . Selection of coordinates  $(x, y, z)$  in integer units of [mm] determine a unique index corresponding to the array in the table containing the components at that grid point. Indices in an array begin at zero, so that the last element in the array has index  $(n_x n_y n_z - 1)$ . This can be shown for the index calculation shown.

$$i = i_x + i_y n_x + i_z n_x n_y \quad (3.8)$$

Using this data structure is far more efficient than looping through a multi-dimensional array and performing a check until the desired positions are found. Each

time the magnetic field is needed, the first step is to store the ceiling and floor value of each coordinate into an array. With these, the field components of the 8 nearest grid points surrounding the true position can be quickly retrieved from the hash table. A trilinear interpolation algorithm is then used for each component to approximate the field components at the true position. That is, the field is assumed to be linear in each axis within the region of each  $1 \text{ mm}^3$  cube.

Interpolation is not an efficient method for two reasons. First, discontinuities in the derivatives of the field at the face of each cube causes the adaptive stepsize controller to reduce the time steps by orders of magnitude, resulting in a severe increase in the computation time. Tricubic interpolation could be used to make the derivatives continuous, but it requires 64 rather than 8 nodes and considerably more calculations. The second reason is a weakness of trilinear interpolation which would be even worse for tricubic: the interpolation algorithm must be performed for each component of the holding field, spin-flipper field, and the electric field; that is at least 6 times for the magnetic field (assuming a perfect electric field). It is possible with analytical models to only calculate the polynomials related to the position a single time. Interpolation is a general method in that it can be used for any field profile. However, for fields which can be easily described with polynomials, it is not the best method for performance.

## Analytical Field

Suppose there existed a perfectly uniform magnetic field, with some linear gradient. This field can be quickly determined everywhere to machine precision by the equation:  $\vec{B} = (B_0 + G_z z \hat{z}) - \frac{G_z}{2} \rho \hat{\rho}$ , with constant  $G_z = \frac{dB_z}{dz}$ . This can be extended to arbitrary order in the gradients, then the coefficients  $G_i$  will uniquely define the field. This process would involve creating a map of the field (from theory, COMSOL, or an actual map) as in the interpolation case, though the mesh spacing can be much coarser. Then, a 3-dimensional polynomial fit to any chosen order can be used to characterize each component of the field using a small set of coefficients.

An important note regarding the fitting is interpolation error. In a single dimension, it is standard to use samples spaced at the Chebyshev nodes to minimize this error [40]:  $x_k = \cos(\frac{2k-1}{2n}\pi)$ , where  $n$  refers to the total number of sample points and  $k$  is an integer reference to the node  $k = 1, \dots, n$ . The goal here is to reduce Runge's phenomenon: the presence of large, erroneous oscillations which can occur with minimum  $\chi^2$  fits of polynomial functions with near evenly spaced samples. The theory of minimizing interpolation error becomes very complex for higher dimensions; for the

purposes here, it is sufficient to minimize the error in the independent polynomial axes individually. In order to verify that something akin to Runge’s phenomenon is not occurring, it is essential to split the data into a fit set, used to perform the fitting procedure, and a validation set, used to compare with the model constructed from the fit to check for errors. This can also be helpful in the fitting process, as superfluous data requires more calculation and reaches a point of diminishing returns.

### Field Expansion using Associated Legendre Polynomials

The analytical form of the magnetic field must obey Maxwell’s equations. It is well established in electrodynamics texts [41] that static electric and magnetic fields can be determined within a volume free of sources given the field is known on the boundary surface of the volume. For the case of magnetic fields, the requirements on Maxwell’s equations are  $\vec{J} = 0$  and  $\frac{\partial \vec{E}}{\partial t} = 0$ . In this case,  $\nabla \times \vec{B} = \mu_0 \vec{J} + \mu_0 \epsilon_0 \frac{\partial \vec{E}}{\partial t} = 0$ . By application of vector identity  $\nabla \cdot (\nabla \times \vec{B}) = 0$ ,  $\nabla^2 \vec{B} = 0$ . This is the Laplace equation with well known solutions.

$$f(r, \theta, \phi) = \sum_{l=0}^{\infty} \sum_{m=0}^l r^l P_l^m(\cos \theta) [a_{lm} \cos m\phi + b_{lm} \sin m\phi] \quad (3.9)$$

The general equation 3.9 is satisfied separately for  $f = [B_x, B_y, B_z, U]$ . There is a benefit to using the magnetic scalar potential  $U$ , as it is possible to extract information on the gradients along an axis based on measurements of the field components along a different axis. This is proposed as a method to monitor magnetic field conditions in-situ for neutron EDM experiments via boundary condition measurements [42]. For the purpose of field modeling in a simulation, the “vector” method is more desirable for its simplicity: at each evaluation of the derivatives for the purpose of integration, it is only required to calculate each basis function once at the current location, as these evaluations are common for all components of any field being modeled. e.g.- The vector components of the  $\vec{B}_0$ ,  $\vec{B}_1$ , and even  $\vec{E}$  can all be determined by using different coefficients with the same basis functions.

The application of this method to simulations starts with a field map, either from a theory calculation, COMSOL, or from a map of the actual field. The chi-squared is minimized in order to fit the general solution as expansions in  $\ell, m$  to find fit parameters  $a_{l,m}^i, b_{l,m}^i$  separately for each component  $B^i$ . The vector method is efficient because each expansion term in equation 3.9 can be calculated once for the current neutron position and stored in an array; it is then computationally trivial to determine all three components of the magnetic field.

An additional performance gain was obtained by writing a custom function to calculate the associated Legendre polynomials. For any order in  $(\ell, m)$ , these must be built up from recursion relations 3.10 [43], given an exact expression for the first few terms. A lookup table was populated by calling this function once for each position, thus a single calculation of  $P_{(l_{\max}, m_{\max})}$  gives the necessary associated Legendre polynomials for every basis function in 3.9.

$$(l - m)P_l^m(x) = x(2l - 1)P_{l-1}^m(x) - (l + m - 1)P_{l-2}^m(x) \quad (3.10)$$

$$P_{l+1}^{m+1}(x) - 2xP_l^{m+1} + P_{l-1}^{m+1}(x) = -(2m + 1)P_l^m(x) \quad (3.11)$$

Fitting the field in three dimensions is quite difficult to achieve. All fitting algorithms are highly dependent on the starting point for the parameters, and setting these initial conditions becomes increasingly complex as the degrees of freedom increase. Additionally, the designed field profiles are typically at least  $\mathcal{O}(\ell = 6)$ , and the chi-squared has many local minima in parameter space. Each order in  $\ell$  contains  $(2\ell + 1)$  parameters, resulting in 49 parameters for  $\ell = 6$ . Basin-hopping and simulated annealing optimization methods are better suited to finding estimates of the global minimum for a flat parameter space with many local minima; however, 49 parameters, which differ in sign and by several orders of magnitude, is too large a parameter space to reasonably use such methods.

The solution to this problem was to start by fitting single-dimension special cases to  $\ell = 6$  polynomials: the 3 main axes, and the cases  $z = 0$  with  $x = \pm y$ . Each coefficient of the polynomial fits will then correspond to a linear combination of the desired parameters, which can be solved using a least-squares fit. Consider equation 3.12, which gives the  $\ell = 2$  term in the general expansion (that is, the quadratic terms). The coefficient  $a_{20}$  can be extracted directly from a quadratic fit along the  $z$ -axis only, where every other term in the expansion is zero. A quadratic fit parameter along the  $x$ -axis,  $p_{x^2}$ , is a linear combination of two terms in the  $\ell = 2$  expansion:  $p_{x^2} = -\frac{1}{2}a_{20} + 3a_{22}$ .

$$B_i^{\ell=2} = a_{20}\left(z^2 - \frac{x^2 + y^2}{2}\right) - 3z(a_{21}x + b_{21}y) + 3a_{22}(x^2 - y^2) + 6b_{22}xy \quad (3.12)$$

For each power in  $\ell$  and each 1-dimensional fit axis, a linear equation was constructed in a systematic method by evaluating each term of the given power in equation 3.9, for  $(x, y, z)$  set to either 0 or 1 dependent on the current axis being evaluated.

This gives the relative weight for each term in the 3-dimensional fit relative to the 1-dimensional fit parameters; e.g. - the term  $a_{20}$  contributes to  $p_{z^2} = a_{20}$ , but along the  $x$  and  $y$  axes it contributes  $p_{x^2,y^2} = -\frac{1}{2}a_{20}$ . The system of equations can then be setup as a matrix equation  $p_j = C_{ij}a_i$  and directly solved to find the desired volume parameters  $a_i$ . However, any disagreement in the single axis fit parameters which are correlated with other single axis fits can create erroneous results. Therefore, it is preferable to use a coupled equation least squares fitter to smooth out any inconsistencies in the separate fits when they are combined into one. The NumPy least squares solver in the linear algebra module was selected for this purpose. Figure 3.4 demonstrates the polynomial fits along the axes for the COMSOL model of the  $B_0$  coil.

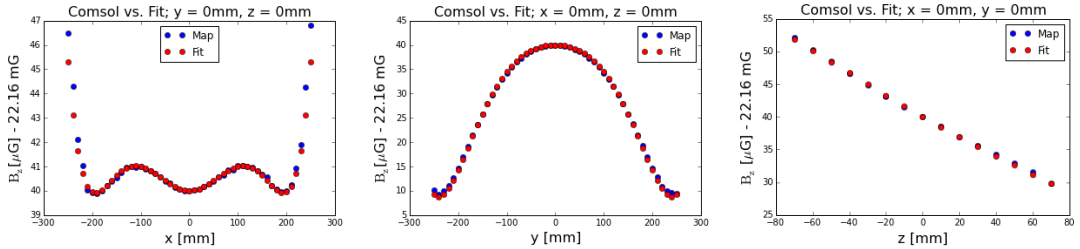


Figure 3.4: Polynomial fits along the main axes of the  $B_0$  COMSOL model.

Order  $\ell = 6$  is still an approximation, therefore care must be taken to ensure that the coefficients for the special cases are self-consistent to prevent a breakdown when the conversion from 1-D to 3-D parameters occurs. For example: the designed  $B_0$  profile from chapter 4 has inflection points in the transverse axes which limits selection of the signs and magnitudes for the  $\ell = 2, 4,$  and  $6$  terms. However, for the longitudinal  $z$ -axis, the field has only a single inflection point in the region of interest, such that very good fits can be achieved with multiple combinations of these terms. By the correlation of 1-dimensional to 3-dimensional parameters, the transverse and longitudinal components are related such that inappropriate fitting of the longitudinal axis prior to this conversion will result in a very poor fit for the volume expansion.

The reconstructions for this model are shown in figure 3.5. It should be noted that the axis chosen looks like it could be possibly fit by  $\ell = 4$ . However, the  $x$ -axis demonstrates clear  $\ell = 6$  features, as shown in figure 3.4. Additionally, the fit is progressively getting worse further from the  $y$ -axis, demonstrating higher order effects. For the  $B_0$  coil with nominal setting of  $2.22 \mu\text{T}$  used in the LANL prototype apparatus, the average magnitude of the residual was found to be  $R_{\text{ave}} = \langle B_z^{\text{Model}} - B_z^{\text{COMSOL}} \rangle = 0.07 \text{ nT}, \sim 31 \text{ ppm}$  (Fig. 3.6). The resulting set of coefficients was

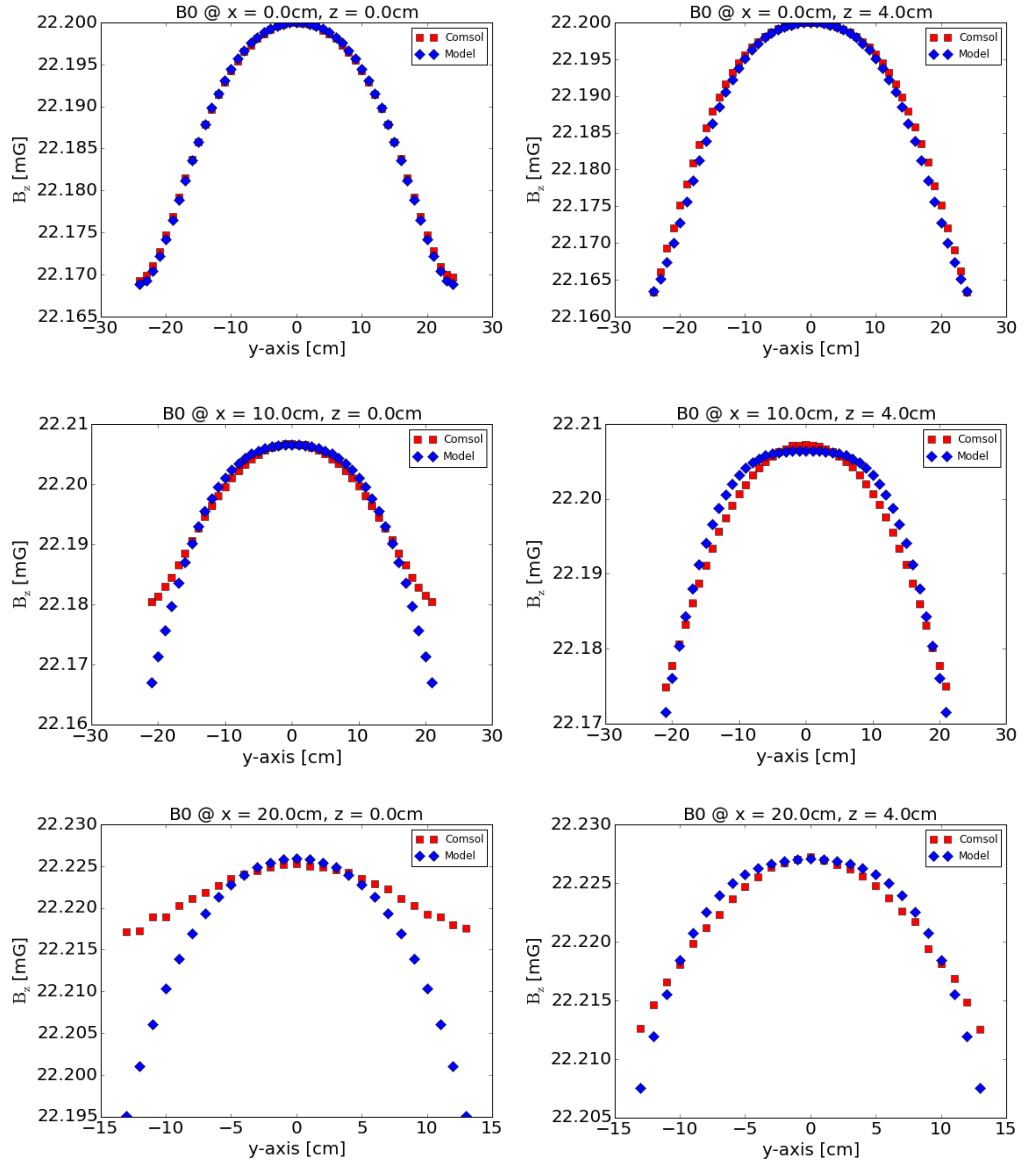


Figure 3.5: Comparison of the 49 parameter fit model to COMSOL along the  $y$ -axis at different positions in  $x$  and  $z$  for the optimized double-gap solenoid. Fiducial volume is  $z \in (-5 \text{ cm}, 5 \text{ cm})$  and  $\rho < 25 \text{ cm}$ .

used in simulation to study the systematic effects associated with the details of the magnetic field profile.

A single set of fit parameters for a typical  $B_0$  setting was used and scaled when testing different settings. The coupling of the magnetic field with the shield is a complex relationship because of the dependence on the relative magnetic permeability,  $\mu_r = \mu/\mu_0$ , changing with the magnitude of the field inside the shielding material.



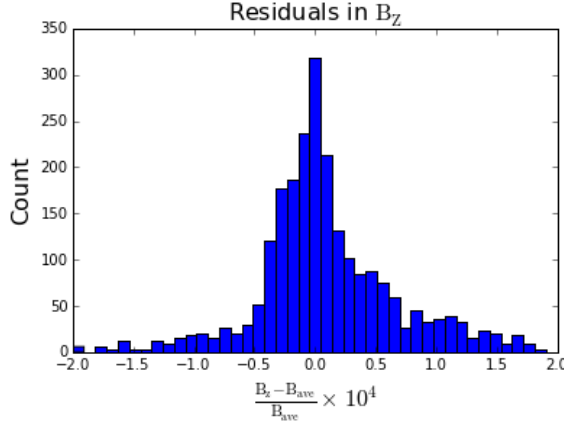


Figure 3.6: Histogram of the residuals comparing the  $\ell = 6$  expansion with the COMSOL model of the  $B_0$  prototype at  $2.2 \mu\text{T}$ .

As the shield saturates,  $\mu_r$  decreases, which will result in perturbations to the field profile. The COMSOL model accounts for this effect by using the hysteresis curve for a material similar to the real shield, but repeating the COMSOL model and the fitting procedure for each test is not practical. Though most of the coefficient fitting process is automated in Python, setting the initial parameters for the 1-dimensional fits is a very time consuming, manual process. For the ranges of  $B_0$  settings considered, the magnetic flux from the coils does not saturate the shield material as much as the external background fields. Consequently, for studies which change the  $B_0$  setting, the same set of coefficients were scaled to set the desired  $B_0$ .

### 3.4 Spin Relaxation

A neutron polarized along a perfectly uniform magnetic field will retain that polarization indefinitely in the absence of any interactions, e.g., collisions. Real fields will have non-uniform profiles, such that the direction and magnitude of the field will vary by position. For an experiment in which knowledge of the polarization is essential to the result, it must be well understood how long the spins remain polarized. There are two important spin orientations for experiments: 1. The case in which the polarization is along the nominal magnetic field such that  $\vec{S} \times \vec{B}_0 = 0$ ,  $T_1$ ; 2. The case in which the polarization is in the plane perpendicular to the magnetic field such that  $\vec{S} \cdot \vec{B}_0 = 0$ ,  $T_2$ . Longitudinal polarization must be maintained during the loading and unloading stages, typically on the order of 10's of seconds. Transverse spin relaxation must be sufficiently long that the neutrons do not depolarize during the free precession period,  $\sim 100$  seconds. Each of these would present in the Ramsey

method as decreased visibility of the fringes,  $\alpha$ .

### Longitudinal Spin Relaxation $T_1$

The longitudinal spin relaxation  $T_1$  can be determined by measuring the polarization as a function of time for an initial sample of neutrons ideally 100% polarized parallel to the nominal magnetic field. A sufficiently large number of completely unpolarized neutrons can be expected to have equal counts of spin-up and spin-down within statistical uncertainty. If these two states are counted as “+1” for up and “-1” for down, then the average “polarization” of an unpolarized sample would be 0, and 100% polarization would have an average of  $\pm 1$ . Using this model, the spin relaxation time can be determined by an exponential fit of the average polarization as a function of time.

$$P(t) = P_0 e^{-t/T_1} \quad (3.13)$$

In measuring  $T_1$  experimentally, it is unlikely that the initial polarization is perfect. This is accounted for by inclusion of  $P_0$ , the polarization at  $t = 0$  s, as an additional fit parameter. To determine  $T_1$  via simulation for the model  $B_0$  field profile, the spinor is initialized in the eigenstate  $\Psi = \begin{pmatrix} 1 \\ 0 \end{pmatrix}$ , corresponding to spin-up in the  $S_z$  basis. The expectation values for each component of spin are sampled at pre-determined times and stored in a data file for offline analysis. For each sample, the expectation value of  $\langle \sigma_z \rangle$  is averaged over all simulated particles. These are then fitted to equation 3.13 to determine  $T_1$  as a fit parameter, with the square root of the appropriate term in the covariance matrix used as the uncertainty  $\sigma_{T_1}$ .

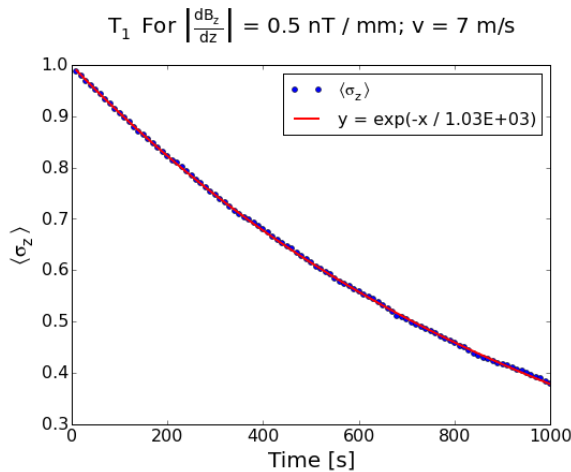


Figure 3.7: Example of simulation results fitted to exponential curve to extract  $T_1$ .

For validation purposes, simulations were run with  $N = 10000$  each for UCNs at different energies corresponding to velocities ranging from  $|\vec{V}| \in (3 \text{ m/s}, 7 \text{ m/s})$ . The magnetic field was assumed to be of the form

$$B(\vec{r}) = (10 [\text{mG}] - G_z z)\hat{z} + \frac{G_z}{2}\rho\hat{\rho} \quad (3.14)$$

with  $G_z = 5 \times 10^{-10} \text{ T mm}^{-1}$ . The intent was to choose a linear gradient comparable with that from the ILL experiment [1], which could be compared with the  $T_1$  measured by ILL and theoretical values from Redfield theory as applied by McGregor [31].

$$\frac{1}{T_1} = \frac{\delta B^2 k T \tau_c}{2mB_0^2 [1 + \gamma^2 B_0^2 \tau_c]} \tau_c \approx \frac{\rho L}{2(\rho + L)\sqrt{\frac{3kT}{m} - gL}} \quad (3.15)$$

where  $\tau_c$  is the approximate time between wall collisions,  $k$  the Boltzmann constant,  $g$  the acceleration due to gravity,  $m$  is the neutron mass, and  $T$  the temperature in Kelvin. This is originally derived for a low density gas; in order to compare with simulation results, the kinetic energy of the neutrons is converted to a temperature via  $\frac{1}{2}mv^2 = \frac{3}{2}kT$ .

When considering no wall interactions,  $T_1$  for this average gradient is  $\mathcal{O}(10^6 \text{ s})$ . The simulation result is extracted from an exponential fit, which would require considerable computation time. Also, the comparison to the ILL measurement would not be accurate, because loss / depolarization of neutrons due to wall interactions and free neutron decay prevents a reasonable measurement on this order of time. Therefore, an order of magnitude larger gradient was used, resulting in  $T_2$  reduced to  $\mathcal{O}(10^4 \text{ s})$ . The factor of  $100\times$  difference between the two for a gradient change of only  $10\times$  is expected, as  $T_1$  is inversely proportional to  $|\frac{dB_z}{dz}|^2$  in the McGregor formulation.

Simulation results give a higher  $T_1$  for “realistic” and random reflections than the gas model of [31]. Diffusive motion is associated with local confinement of a particle to some region, which would create groups of particles akin to domains, where they only sample the fields in that region. Consider the limit in which the neutrons are effectively stationary: the magnetic field vector is constant, and so the polarization will not change. Modeling diffusion with random wall collisions rather than a true “random walk” creates an isotropic distribution within the chamber similar to diffusion, but does not locally confine neutrons. This might also explain why there is not a large difference in the “realistic” and random wall reflections; one is more isotropic, but they both sample the cell volume extensively.

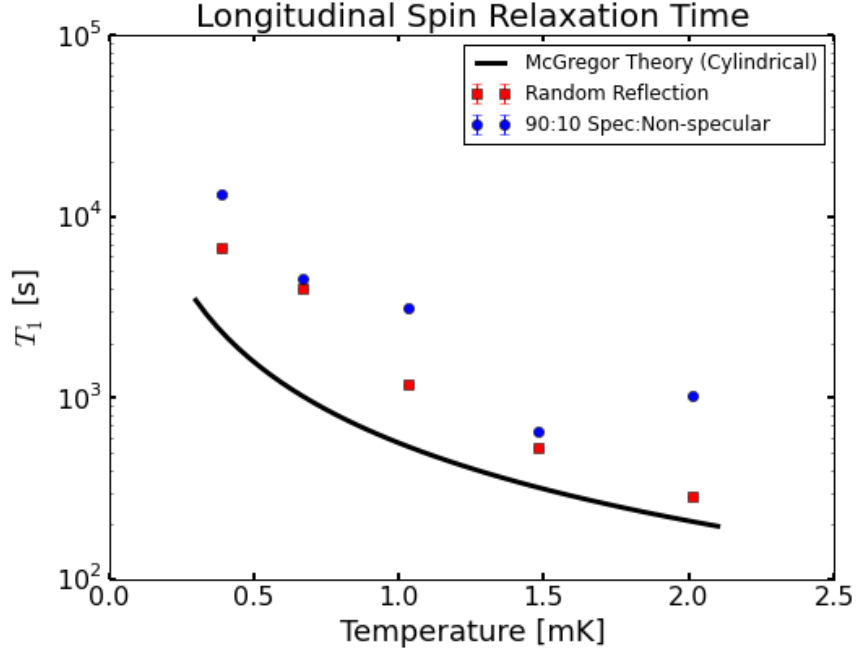


Figure 3.8: A comparison of  $T_1$  as a function of UCN energy for “realistic” and random wall reflections compared to the Redfield / McGregor model for a gas given as a function of temperature.

It is also interesting to note the fluctuations in the “realistic” reflection simulations as a function of energy. This is possibly related to the Ramsey-Bloch-Siegert shift, used to derive the false EDM in section 2.3. Recall in section 2.3 that the transverse fields alone cause longitudinal depolarization. Specular reflections at large radius can be approximated as circular orbits, such that the neutrons will experience a rotating transverse field at angular frequency  $\omega \approx \frac{\pi\rho}{v_\phi}$ . The orbital velocity  $v_\phi$  is different for each energy sampled in this simulation and changes within each energy due to the velocity also containing a vertical component, which results in a complicated ensemble average  $\omega$ . There is also a RBS shift to the resonant frequency  $\omega_0$  which differs for each velocity, which also affects the probability of a spin-flip as given in the Rabi formula, equation 2.15. For random reflections, circular paths are not taken such that the assumptions for the RBS shift and rotating field breaks down, which explains why these fluctuations are not present for random reflections.

### Transverse Spin Relaxation $T_2$

For transverse spin relaxation, the particle is considered to be polarized in the  $xy$  plane. Because the polarization is precessing in the  $xy$  plane for this state, the straightforward analysis used for longitudinal polarization is not applicable. Depo-

larization in this case can be thought of as the accumulation of different amounts of phase amongst the sample of neutrons in the plane of precession. An additional effect is depolarization out of the transverse plane, i.e. - the polarization rotates out of the transverse plane as a result of the coupling to transverse fields, which then affects the rate of phase accumulation. This effect was discussed in section 2.3.

In this experiment, the transverse spin relaxation can be determined very similarly as the longitudinal case. The neutrons must first be polarized longitudinally, then a  $\pi/2$  spin-flip is applied to polarize the spins in the transverse plane. After some free-precession time,  $t$ , then a second spin-flip is applied and the spins are transported to an analyzer. Repeating for multiple different holding times  $t$  and fitting the polarization to equation 3.13 will yield  $T_2$ .

For the simulation, it is easier to use a different analysis. The initial spin state used for these tests is the eigenstate  $\Psi = \frac{1}{\sqrt{2}} \begin{pmatrix} 1 \\ 1 \end{pmatrix}$ , such that every simulated neutron has the same spin state corresponding to  $\langle \sigma_x \rangle = 1$ . If a histogram were made of the polarization angle in the  $xy$  plane, this initial state would be a delta function at the initial phase,  $\phi = 0$ . By comparison, a fully depolarized sample would be a perfectly flat histogram with equal probability of every angle from  $\phi \in (-\pi, \pi)$ . Taking a snapshot at some time  $t$  between these two asymptotes and assuming the distribution of angles is Gaussian,  $T_2$  can be extracted directly using the relation 3.16.

$$P(t) = P_0 e^{-t/T_2} = P_0 \exp\left(\frac{\sigma_\phi^2 + \sigma_\theta^2}{2}\right) \quad (3.16)$$

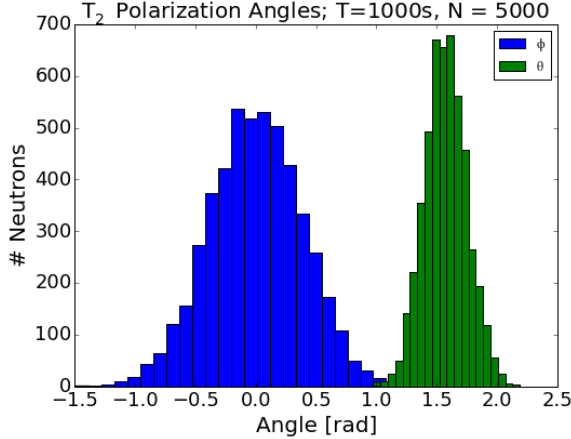


Figure 3.9: Sample histogram used to extract  $T_2$  from simulation for  $\left| \frac{dB_z}{dz} \right| = 5 \times 10^{-11}$  T mm<sup>-1</sup>, using random wall collisions and velocity  $v = 7$  m/s.

As a leading order test of the simulation,  $T_2$  was simulated for different discrete energies of the UCN and compared with the theoretical models of Cates, Schaefer, and

Happer [32] and McGregor [31]. This model gives an analytical solution for diffusive motion through a magnetic field with constant gradients as in equation 3.14.

$$\frac{1}{T_2} = \frac{1}{2T_2} + \frac{\gamma^2 L^4}{120D} \left( \frac{\partial B_z}{\partial z} \right)^2 + \frac{7\gamma^2 a^4}{96D} \left( \frac{\partial B_z}{\partial \rho} \right)^2 \quad (3.17)$$

$$D \approx |v| \frac{aL}{2(a+L)} \quad (3.18)$$

where  $a$  is the radius of the cylindrical chamber,  $L$  is the length, and the diffusion constant  $D$  is estimated using the volume, surface area, and velocity to determine the average distance and time between wall collisions. Using the wall reflections based on the model of Steyerl et al. results in a  $T_2$  which differs significantly from the McGregor model.

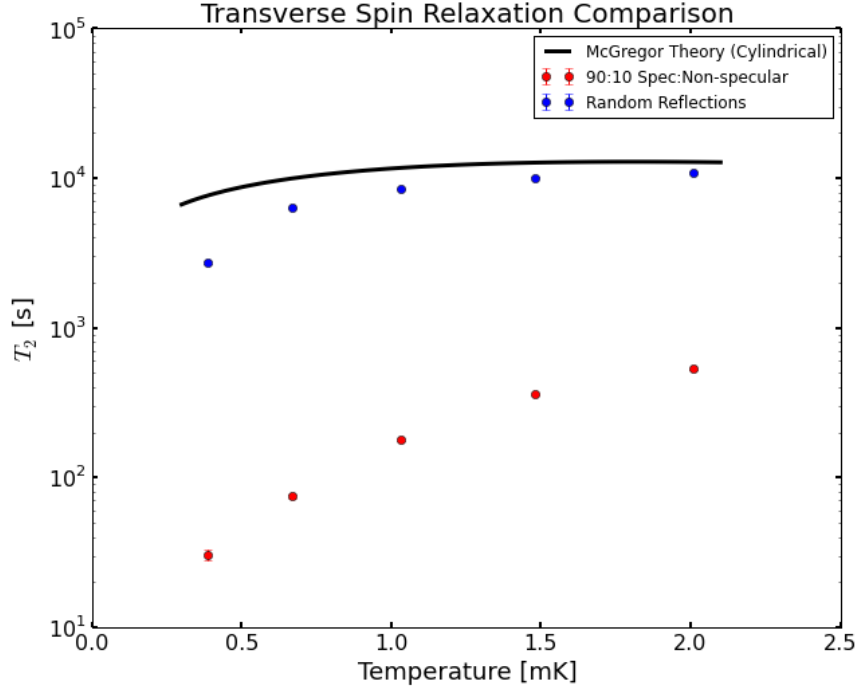


Figure 3.10: A comparison of  $T_2$  as a function of UCN energy for “realistic” and random wall reflections compared to the McGregor model for a low density gas as a function of temperature.

Intuitively, this is to be expected for a high percentage of specular wall collisions. As discussed in section 2.3 for the approximation of circular paths inside a cylindrical chamber, field profiles which are even in  $\ell$  result in the Larmor frequency being a function of the radius, whereas field profiles which are odd in  $\ell$  see an averaging of

the field such that the Larmor frequency is independent of the radius. As previously shown, the neutron distribution changes substantially from specular to non-specular reflections. The McGregor model assumes a low density gas which diffuses through the chamber. A better comparison with the McGregor solution would use a random walk to model diffusion. For simplicity, this was approximated by simulating  $T_2$  for random wall reflections, which is shown to agree very closely with the McGregor model. They diverge at lower energies, which is an artifact of using the wall reflections to approximate a “random walk”. For lower speeds, the neutron spin accumulates more phase before sampling a different trajectory. As an additional validation of the simulation, the constant gradient used here was comparable to the gradient of the most recent ILL nEDM measurement.  $T_2$  was measured to be  $\sim 600$  s for their apparatus [44], which agrees very well with simulation results for “realistic” reflections. Recall that the UCN energies have an approximate distribution  $P(v) \propto v^2$ , such that the weighted average of  $T_2$  is closer to the values near the maximum velocity.

The sharp decrease in  $T_2$  at lower energies is also interesting. Consider the limit that kinetic energy goes to zero, i.e. - static neutrons, for an isotropic spatial distribution. In this limiting case, there is no sampling of different field regions, such that depolarization occurs instantly. Local confinement is problematic for  $T_2$  because the rate at which phase accumulates is a function of position, and there is no averaging when the neutrons are confined. Likewise, very slow neutrons do not sample enough of the field for substantial averaging to occur.

### 3.5 Studying the Effects of Non-Constant Gradients

Systematic effects are often analytically quantified by working with leading order terms in an expansion of the relevant fields. Attempting to correct these effects term-by-term may be insufficient. For example, the primary focus in designing the  $B_0$  coil for the LANL nEDM experiment was to minimize the average magnitude of the gradient component  $\frac{dB_z}{dz}$  in the entire volume of interest. A gapped solenoid, i.e. - two solenoids separate axially by a gap, can have the gap spacing optimized to reduce the axial gradient in the magnetic field. Analytical solutions employ an expansion of the axial component of the field near the center, and set the gap length such that the leading order term in the gradient is zero [45]. With increased computational resources, it is feasible to numerically calculate the average of  $\frac{dB_z}{dz}$  within a volume of interest and use optimization algorithms to find the gap length which minimizes this metric. It is proposed that this method is a better option, because it is possible that

setting a low order term to zero has a severe negative affect on higher order terms, which may become significant within a volume. This raises an interesting topic to be explored in simulation: how much of an effect can be expected due to non-constant magnetic field gradients? Is it sufficient to look at leading order terms, or should a method to consider the cumulative effect of all terms be developed?

In deriving analytical solutions to the spin relaxation times, it is common practice to assume a simple magnetic field profile approximated as a constant gradient in the region of interest, e.g.,  $\vec{B} = (B_0 + G_z z \hat{z}) - \frac{G_z}{2} \rho \hat{\rho}$ , with constant  $G_z = \left(\frac{dB_z}{dz}\right)$  [31][32]. In designing the prototype  $B_0$  coil in chapter 4, the primary goal in optimization was to minimize the volume average of  $\langle \frac{dB_z}{dz} \rangle$  in order to minimize the false EDM effect discussed in section 2.3. This may not be an effective strategy if the systematic effects are immune or susceptible to different symmetries of the simple model which was used in the derivation.

Simulation studies were conducted using a 10cm long, 25cm radius cylindrical storage chamber. Magnetic fields with an even and odd profile were designed with the same average gradients inside this fiducial volume. Designing magnetic fields which satisfy Maxwell's equations,  $\vec{\nabla} \cdot \vec{B} = 0$  and  $\vec{\nabla} \times \vec{H} = \vec{J} + \frac{\partial \vec{D}}{\partial t} = 0$  (no currents or time-dependent electric fields in the volume), becomes difficult at higher orders due to an increase in the degrees of freedom, giving more potential field profiles using a given order in  $L$  with the same average gradient. To reduce these complications, simple linear and quadratic profiles were compared.

### Comparing Linear and Quadratic Fields

The magnetic field in this study is designed to have the same nominal field value of 10 mG = 1  $\mu$ T, the same average magnitude of the gradient over the chamber volume  $\left|\frac{dB_z}{dz}\right| = 3.0 \times 10^{-13}$  T mm<sup>-1</sup>, and must satisfy Maxwell's equations, requiring the divergence  $\vec{\nabla} \cdot \vec{B} = 0$  and  $\vec{\nabla} \times \vec{B} = 0$  (for  $\vec{J} = \frac{d\vec{D}}{dt} = 0$ ). For the quadratic field profile and higher-order terms, there are excessive degrees of freedom compared to the constraints used, meaning that additional magnetic field anisotropies are possible. For the quadratic case, I used azimuthal symmetry as an additional constraint to finalize the field profile. It is worth future study to determine what effects might have been missed by the azimuthally symmetric quadratic example chosen.

$$\vec{B}_{\text{linear}} = g_l x \hat{x} + g_l y \hat{y} + (B_0 - 2g_l z) \hat{z} \quad (3.19)$$

$$\vec{B}_{\text{quad}} = -\frac{g_q}{3} x z \hat{x} - \frac{g_q}{3} y z \hat{y} + (B_0 + g_q z^2) \hat{z} \quad (3.20)$$



where  $g_l = 1.5 \times 10^{-13}$  [T / mm],  $g_q = 1.2 \times 10^{-14}$  [T / mm<sup>2</sup>], and  $B_0 = 1 \mu\text{T}$ .

An analysis is made of the transverse spin relaxation time, which is more significant than the longitudinal spin relaxation in the method of separated oscillatory fields. In general,  $T_1$  is larger than  $T_2$ , and  $T_1$  is only important during loading and unloading of the storage cell, which is on the order of 10's of seconds compared with the target 100's of seconds in which the neutrons will precess in the transverse plane. In the case of purely specular wall reflections, the neutrons sample some average radius, which for this argument we can consider the trajectories approximately circular in the  $xy$  plane of the cylinder. This approximation becomes increasingly true as the average radius gets nearer the edge of the cell wall. Even fields are azimuthally symmetric such that precession frequency will be a function of radius (for approximately circular trajectories). The precession frequency for odd fields will oscillate as a function of the orbit angle, all averaging about the central field value. Thus, at leading order it is expected that for purely specular reflections, the odd field will not depolarize the neutrons, and the even field will very quickly depolarize them.

The general trend of this argument is found in simulation to be true as shown in Figure 3.11, where 'smooth' wall indicates reflections are 100% specular. The dephasing at 10 s for the quadratic field is an order of magnitude worse than the linear field dephasing at 100 s. An interesting feature of these results is that the angles dephase asymmetrically, which is expected if the precession frequency is a function of the radius with a uniform distribution. The differential area is  $dA = \rho d\phi d\rho$ , so that more neutrons are at a larger radius if the density is constant. This feature begins to disappear once wall collisions include a small percentage of non-specular reflections ('rough'), which will periodically shift the neutron to a different average radius.

Linear fields are demonstrated to also cause depolarization, though the argument made previously was that they would not. This dissonance is the result of the 'constant radius' approximation. For a given state in phase-space, the neutron will not remain at a constant radius, but will instead move in straight-line chords, as shown in Figure 3.2, which vary from a minimum radius  $\rho > 0$  to a maximum radius at the cell wall. The circular orbit argument was dependent on the additional phase accumulated due to the magnetic field shift sampled on one side of the chamber to be exactly canceled by the magnetic field shift on the opposite side,  $\Delta B(\phi) = -\Delta B(\phi + \pi)$ , where  $\Delta B$  is the shift in the magnetic field from the central value  $B(\rho = 0)$ . This is not true for chords; in general, the radius of the neutron at a given angle in the cylinder plane  $\rho(\phi) \neq \rho(\phi + \pi)$ , so that  $\Delta B(\phi) \neq -\Delta B(\phi + \pi)$ .

These simulation results indicate that the even terms in the magnetic field impact

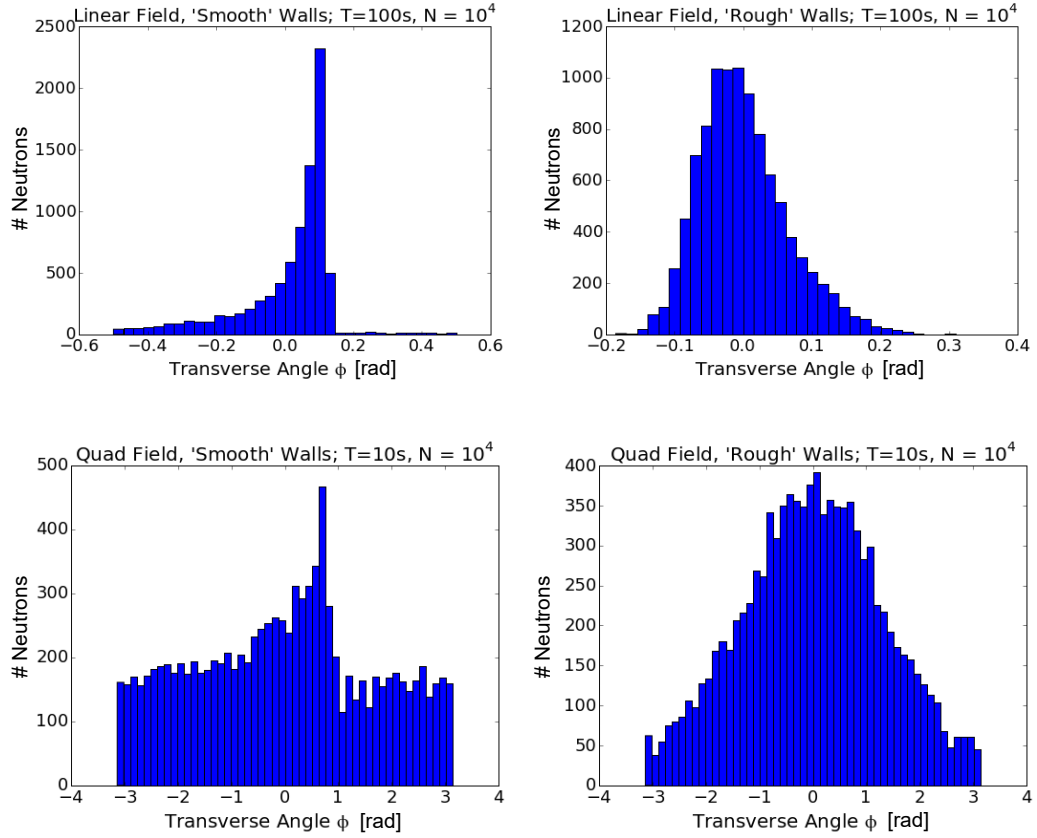


Figure 3.11: Comparison of  $T_2$  for a linear and quadratic field profile, with purely specular reflections and a mix of non-specular.

the transverse spin relaxation time,  $T_2$ , significantly more than the odd terms. It is important to note the underlying cause of this mechanism: the radius of the neutrons are restricted within some range; and a single term in an even field profile will only either increase or decrease as a function of radius. The latter argument is concerning, since most magnetic field sources are built with a symmetry which will result in even field profiles. The qualifier ‘single term’ is important here, because even field profiles including multiple terms of different even powers in  $\ell$  with differing signs can result in oscillations in the field as a function of the radius. Neutrons sample a region from some minimum to maximum radius, so that this oscillation can reduce the dephasing substantially. As an example, the prototype coil in chapter 4 has a quadratic term of  $g_q = -3.0 \times 10^{-14}$  T / mm<sup>2</sup>, but a simulated  $T_2 > 800$  s, resulting from  $\ell = 4, 6$  terms which smooth out the magnetic field profile.

In summary, depolarization is determined by a complex relationship between the gradients in the field and the phase-space of the neutrons. For a cylindrical chamber, the even terms contribute more significantly to transverse spin relaxation, especially when the wall reflections are primarily specular. Perhaps it is even beneficial to include as many observable even powers in the field as possible, such that the field rapidly oscillates as a function of position, but never differs by an appreciable amount. This could help by averaging out over shorter characteristic times. It could also be beneficial to use a less symmetric storage chamber in order to promote a more thorough sampling of the magnetic fields. These are questions which can be studied best via simulation.

## Chapter 4 $B_0$ Coil Design

### 4.1 Gapped Solenoid

Many experiments require some constant, uniform magnetic field, and a long solenoid of helically wound wire is the most simple method used to produce such a field. An obvious problem with this in practice is the requirement to have apparatus inside the center, where the field is most uniform. It is possible to route equipment through the open ends, though for a uniform field this length can be considerable. Splitting the solenoid into two smaller solenoids with a gap between them allows easier access to the center, and also generally increases the uniformity of the magnetic field. As discussed in section 2.3, field uniformity is of the utmost importance due to systematic effects in EDM searches.

A gap introduces a degree of freedom which can be tuned to improve the magnetic field uniformity. A conceptual picture showing the mechanism which reduces the magnetic field gradients of a gapped solenoid can be seen in Fig. 4.1.

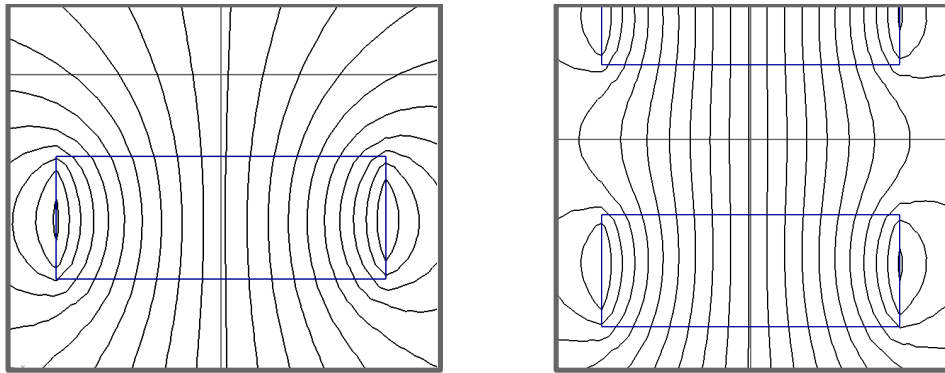


Figure 4.1: A demonstration of the magnetic flux density between split solenoids (blue lines). Magnetic field lines (black lines) are plotted for simple bar magnets. Left: A single magnet’s magnetic field diverges in a dipole pattern. Right: Aligned with an opposite pole and with a gap, the flux is pushed inward, straightening the magnetic field lines along the length and decreasing the magnetic field gradients over a greater distance.

Often in magnetic coil design, a “flux return” may be used to reduce the magnetic field extending into other regions, to prevent saturating an external shield, or to increase the uniformity of the interior field. A flux return in this sense is a layer of material with high magnetic permeability which acts as a sink for magnetic flux

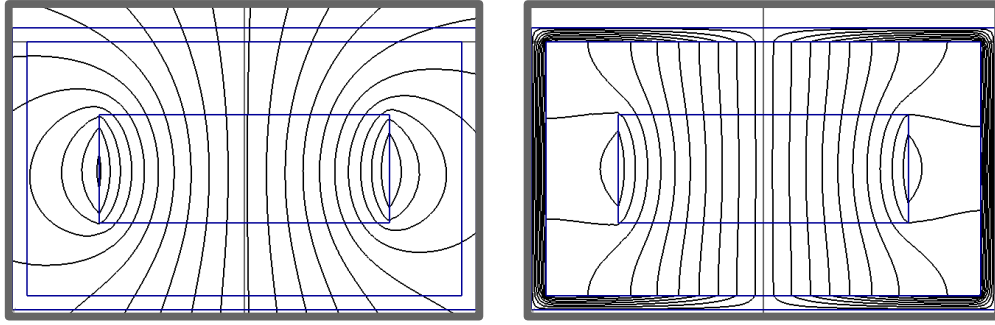


Figure 4.2: A demonstration of the increased magnetic field uniformity when a solenoid is placed within a magnetically shielded enclosure using 2D FEA. Left: A single magnet’s magnetic field diverges in a dipole pattern. Right: Surrounded by a material with high magnetic permeability which draws in magnetic flux density.

from the source. A gapped solenoid can be thought of as two magnetic sources which return flux to each other at the adjacent ends (not the exterior region, as in the stated analogy). A comparison of 2D finite element analysis (FEA) results for a gapped solenoid in vacuum and a single solenoid inside an external shield flux return (figures 4.1 and 4.2) demonstrates the similar effect each of these have on the interior field. Due to this flux return type of mechanism, the concavity of the magnetic flux (i.e.- the degree of inward / outward curvature of the vector potential contours) can be tuned with the gap-length. The field uniformity advantage of the gapped solenoid may also be used to substantially shorten the length compared to a solid solenoid.

Gapped solenoids have in fact been extensively used for a very long time: a Helmholtz coil could be considered a solenoid with a gap composed of two loops of wire with spacing designed to set  $\frac{\partial^2 B}{\partial z^2} |_{\vec{r}=0} = 0$ , with the axis running through the coils defined as  $\hat{z}$ . There is still a benefit to using traditional solenoids compared with thin current loops: the larger area with a current density “smooths” out the magnetic field in a volume. Effectively, this decreases the sensitivity to wire placement while also increasing uniformity. Unfortunately, optimization of a continuous current distribution is more difficult to achieve compared with discrete current loops.

In an interesting paper discussing the advantages of optimizing the gap length between two solenoids (as opposed to current loops), Gosling and Cunningham proposed a straightforward method to optimize the gap depending on the half-length and radius of the coils [45]. It could be considered a generalization of the Helmholtz condition for coils of finite length.

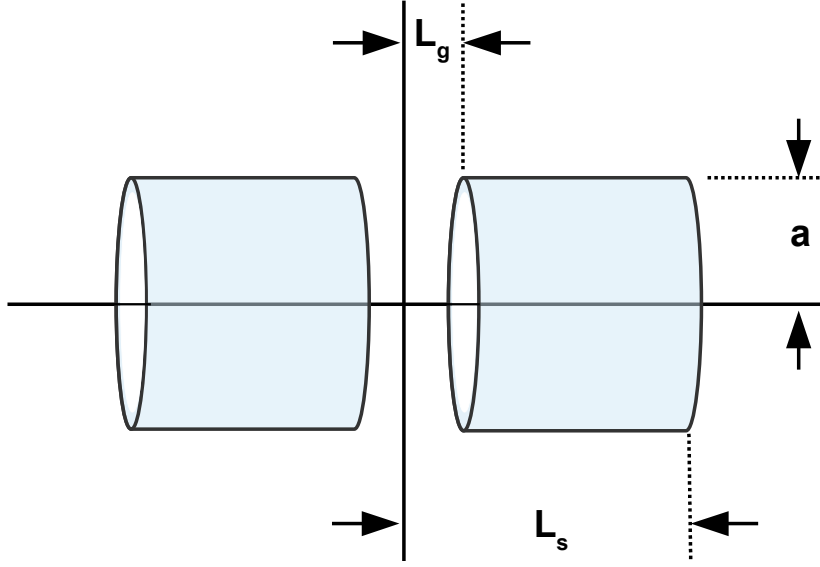


Figure 4.3: Concept used by Gosling and Cunningham [45]. A gapped solenoid is built of a cylindrical shell sheet of current with half-length  $L_s$  and radius  $a$ . The gap is modeled as a cylindrical shell sheet of current with half-length  $L_g$ , identical radius, and opposite current. By superposition, this is equivalent to two individual solenoids of length  $(L_s - L_g)$  with a gap of total length  $2L_g$  and total coil length  $2L_s$ .

As shown in figure 4.3, the authors considered the gapped solenoid to be composed of a single large cylindrical shell sheet of current, and the gap is a single cylindrical shell of current in the opposite direction. This was done for simplicity, and is allowed by the property of superposition. The gap sheet cancels out the large sheet current to produce zero net current on the sheet in the gap region. Consider the expansion of the axial field  $H_m$  due to one of these sheets in terms of Legendre Polynomials, normalized to be unit-less.

$$H_m = A_m - \frac{3}{2}B_m\rho^2P'_2(\cos(\theta)) + \dots \quad (4.1)$$

$$A_m \equiv \chi_m (1 + \chi_m^2)^{-1/2} \quad (4.2)$$

$$B_m \equiv \chi_m (1 + \chi_m^2)^{-5/2} \quad (4.3)$$

$$\chi_m \equiv L_m/a \quad (4.4)$$

Here,  $L_m$  refers to the half length of either the total solenoid or the gap,  $a$  is the radius. The authors considered field homogeneity near the center, such that

radial fields will be negligible and the axial component of the field can be written as an expansion 4.1. In this picture, the total field is the difference between the large solenoid sheet and the gap sheet:  $H = H_s - H_g = (A_s - A_g) - \frac{3}{2}(B_s - B_g)\rho^2 P_2'(\cos(\theta)) + \dots$ . The second term is the leading order in the gradient, which can be tuned to zero by optimizing the gap length to the condition  $\chi_s (1 + \chi_s^2)^{-5/2} = \chi_g (1 + \chi_g^2)^{-5/2}$ . They found that for a properly optimized gapped solenoid, the equivalent field uniformity in a volume of interest would require a continuous solenoid four to five times longer. This paper was a great proof of the potential benefits for optimized gapped solenoids.

One important aspect which was not addressed in [45] was the coupling of magnetic shielding to a gapped solenoid. A conceptual argument can be made that, because shielding acts as a sink for magnetic flux, the shield would draw the field through the gap, making gradients worse than for a continuous solenoid. An analytical formalism using Fourier transformations for determining the coupling of a source solenoid and shielding was given in a paper by Turner and Bowley [46]. They consider some cylindrical solenoid inside of an infinitely long, cylindrical shield of infinite magnetic permeability. The total current density is written as the sum of a known current distribution solenoid at radius  $a$ ,  $\vec{F}$ , and the undetermined response current in the shield at radius  $b$ ,  $\vec{f}$ :

$$\vec{J} = \vec{F}(z, \phi)\delta(\rho - a) + \vec{f}(z, \phi)\delta(\rho - b) \quad (4.5)$$

Starting with the vector potential  $\vec{A}$ , the authors re-wrote using a Green's function the term:

$$\frac{1}{|\vec{r} - \vec{r}'|} = \frac{1}{\pi} \sum_{m=-\infty}^{\infty} \int_{-\infty}^{\infty} dk \exp[im(\phi - \phi')] \exp[ik(z - z')] I_m(k\rho^<) K_m(k\rho^>) \quad (4.6)$$

where  $I_m$  and  $K_m$  refer to the modified Bessel function of the first and second kind, respectively. The exponential terms of this expansion can be absorbed into the Fourier transform of the source current density. As an example,  $A_z$  is shown.

$$f_z^m(k) = \frac{1}{2\pi} \int_{-\pi}^{\pi} d\phi \exp(-im\phi) \int_{-\infty}^{\infty} dz \exp(-ikz) f_z(\phi, z) \quad (4.7)$$

$$A_z = \frac{\mu_0}{4\pi} \int \frac{J_z(\vec{r}')}{|\vec{r} - \vec{r}'|} dv' \quad (4.8)$$

$$= \frac{\mu_0}{2\pi} \sum_{m=-\infty}^{\infty} \int_{-\infty}^{\infty} dk \exp(im\phi) \exp(ikz) I_m(k\rho) [bf_m^z(k)K_M(kb) + aF_m^z(k)K_M(ka)]$$

They then use the conditions

$$\vec{\nabla} \cdot \vec{J} = 0$$

$$B_\rho(\rho = b) = \left[ \frac{1}{\rho} \frac{\partial A_z}{\partial \phi} - \frac{\partial A_\phi}{\partial z} \right]_{\rho=b} = 0$$

to find the shield current as a function of the source current.

$$f_z^m(k) = -F_z^m(k) \frac{a^2 I_m'(ka)}{b^2 I_m'(kb)} \quad (4.9)$$

This allows for the field everywhere inside the shield to be found using only the Fourier transform of the source current, which is known. The same procedure is carried out for the other components,  $f_\phi$  and  $f_\rho$ . This method was extended in a paper by Bidinosti et al. [47] to consider finite permeabilities and thickness of the shield, though still only for the case of “infinite” length, cylindrical shields. This paper also worked out an optimization to the gapped solenoid problem using a similar method to [45], in which the leading order term in  $k$  was set to zero by careful selection of the gap length, and found a slightly different result, which is expected now that the shield contributes to the magnetic field.

In designing a scale prototype gapped solenoid for the LANL nEDM experiment, I utilized the formalism of Bidinosti et al. [47], using the high permeability limit for the shield, which is a reasonable approximation for an unsaturated mu-metal shield with relative magnetic permeability  $\mu_r \sim \mathcal{O}(10^4)$ . Rather than minimizing the leading order gradient term in an expansion of the field near the center, I considered the average magnitude of the gradient within the volume of interest. An analytical form of the gradient can be taken from the general solution from [47]. Of particular interest is the  $\hat{z}$  component of the gradient, which, as discussed in section 2.3, is the



most significant contributor to a false EDM effect, and is easily calculated. Since the solenoid's wires will have discrete thickness, and thus the gap length around the edge circumference of the helically-wound coil will likely vary on the order of this width, it then becomes reasonable to perform a grid-search for the optimum gap length using this average gradient.

### Gapped Solenoid Theoretical Design

The starting point for my optimization of a gapped solenoid is the equation for the magnetic field inside an infinitely long cylindrical shield using the formalism of Bidinosti et al. [47], with  $R_m(k)$  as given in the high permeability limit and in the region  $\rho < a < b$ :

$$\begin{pmatrix} B_\rho \\ B_\phi \\ B_z \end{pmatrix} = -\frac{\mu_0 a}{2\pi} \sum_{m=-\infty}^{\infty} e^{im\phi} \quad (4.10)$$

$$\times \int_{-\infty}^{\infty} dk e^{ikz} [K'_m(ka) + R_m(k)] F_\phi^m(k) \begin{pmatrix} \frac{k}{i} I'_m(k\rho) \\ \frac{m}{\rho} I_m(k\rho) \\ k I_m(k\rho) \end{pmatrix}$$

$$R_m(k) = -\frac{I'_m(ka)K_m(kb)}{I_m(kb)} \quad (4.11)$$

A benefit of this analytical form is the simple solution to the  $\hat{z}$  component of the gradient, which is the metric used to optimize the gap length. Having an analytical form for the gradient reduces the computation time relative to numerically calculating the derivatives at each integration step.

$$\begin{pmatrix} \frac{dB_\rho}{dz} \\ \frac{dB_\phi}{dz} \\ \frac{dB_z}{dz} \end{pmatrix} = -\frac{\mu_0 a}{2\pi} \sum_{m=-\infty}^{\infty} e^{im\phi} \quad (4.12)$$

$$\times \int_{-\infty}^{\infty} dk ik e^{ikz} [K'_m(ka) + R_m(k)] F_\phi^m(k) \begin{pmatrix} \frac{k}{i} I'_m(k\rho) \\ \frac{m}{\rho} I_m(k\rho) \\ k I_m(k\rho) \end{pmatrix}$$

$$R_m(k) = -\frac{I'_m(ka)K_m(kb)}{I_m(kb)} \quad (4.13)$$

For approximate coil diameters 1 m and wire diameter 1 mm, the pitch of the wires is so small that the constant current density sheet model shown in Fig. 4.3 is a suitable approximation which reduces substantial complexity. The Fourier transform of the current density for this case is, where  $L_g$  is the half-length of the gap, and  $L_s$  is the half-length of the completed solenoid (i.e.- the full length of one of the coils, plus  $L_g$ ):

$$F_\phi^m(k) = \frac{I \cos \theta}{\pi k} [\sin(L_s k) - \sin(L_g k)] \quad (4.14)$$

A Python script was written to numerically integrate  $\frac{dB_z}{dz}$ , calculated from equation 4.10, over the region of interest to determine the average gradient. The integration is repeated in increments of 1 mm added to the gap-length, chosen on the basis that the gap length can reasonably be controlled to the approximate size of one loop of wire. The volume average is then minimized via least squares. It is important to note that this method is general for any fiducial volume, which is significant in that there is no single optimum gap length for any and all volumes of interest.

### Gapped Solenoid Prototype Test

In order to validate this optimization method, a gapped-solenoid was constructed at approximately half scale to that expected in the full LANL nEDM experiment. The purpose of this test was to compare the measured field profiles and average gradients of a real coil to the model as calculated using Python. The coil was constructed with readily available materials and designed to fit within existing shielding, and likewise the average gradient in this test was not expected to be near the requirements for a nEDM experiment.

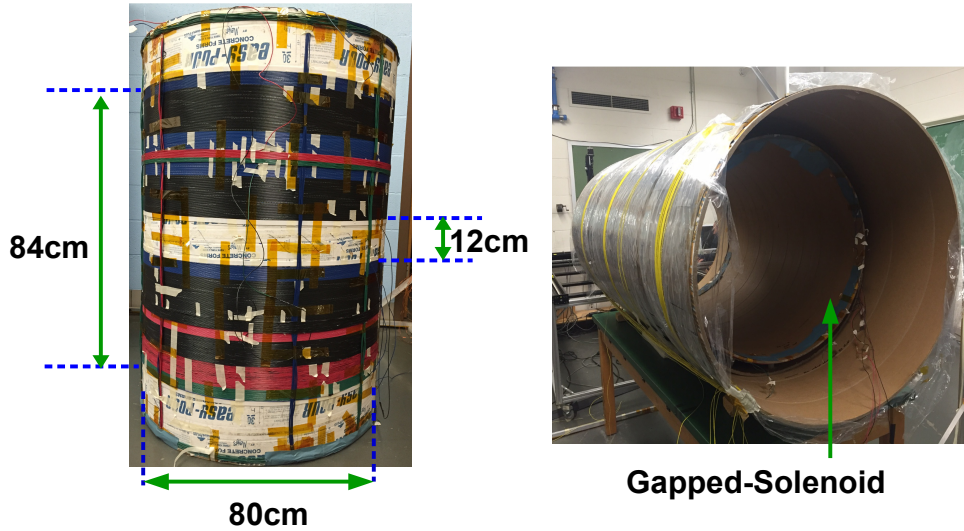


Figure 4.4: 4:7 Scale Gapped-Solenoid. Included are a set of saddle coils to reduce backgrounds. The field was mapped inside a cylindrical shield of axially-aligned strips of Metglas, a material with very high permeability used for magnetic shielding.

The shielding was comprised of a 180 cm long, 94 cm diameter sonotube form (a dense cardboard material forming a cylindrical shell, used for pouring concrete columns) with 2 layers of Metglas strips aligned with the length. The coil was wound on an 80 cm diameter sonotube form; the dimensions can be seen in Fig. 4.4. The backgrounds inside the shield remained on the  $\mathcal{O}(100 \text{ mG})$ , largely due to penetration through the large, open ends. Consequently, saddle coils were wound on each axis of the gapped solenoid to shim backgrounds with the coil turned off, and the gapped solenoid was set to a nominal field of 1 Gauss in order to raise the produced field above the remaining background. Saddle coils are a method to produce an approximately constant field along a transverse axis of a cylinder. They are similar to a Helmholtz coil in that they can be wired with the same current to produce a constant field, or with the opposite current in a pair to produce a zero central field with a linear gradient. Here, the pairs were wired to separate DC current supplies so that the current could have the same direction but different magnitude. Such an “asymmetric” mode produces a transverse field with a central offset and linear gradient. The shim coils were able to reduce the backgrounds by a factor of ten.

The resulting average fractional gradient is very close to the theory prediction, without giving consideration to the uncertainty. A direct comparison of these is difficult to achieve: there were non-linear background gradients which considerably

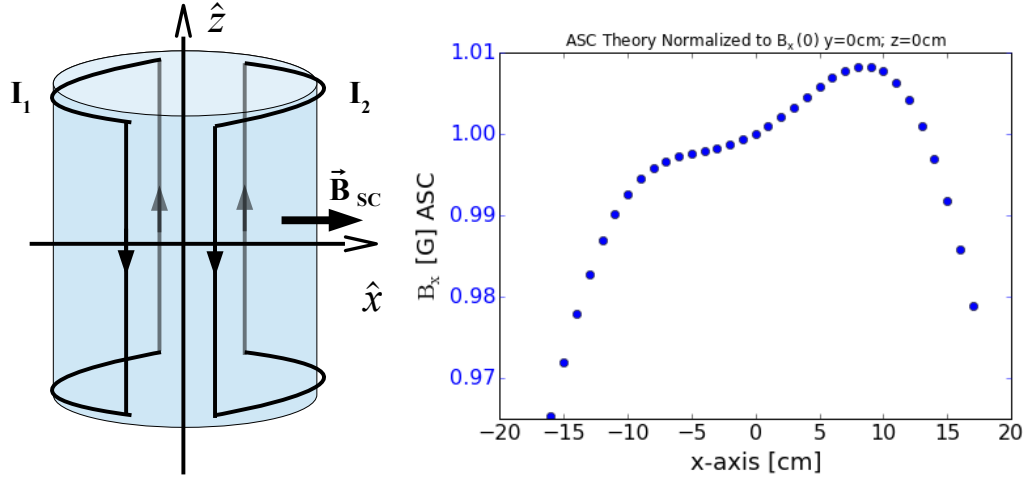


Figure 4.5: Diagram for asymmetric saddle coils, used to produce a transverse field capable of shimming constant field with a linear gradient.

polluted the desired intrinsic gradients of the coil; and the theory assumes an infinitely long shield of infinite permeability. The error in the map is dominated by the backgrounds, therefore it is more suitable to view this measurement as an upper limit on the average gradient.

Table 4.1: Comparison of theory to measured average fractional gradients for half-scale prototype  $B_0$  coil.

$$\left\langle \frac{\frac{dB_z}{dz}}{B(\vec{r}=0)} \right\rangle$$

Theory	$2.33 \times 10^{-4} \text{cm}^{-1}$
Map	$3.05 \times 10^{-4} \text{cm}^{-1}$

It is prudent to check the field profiles along main axes to validate the model calculations. Fig. 4.6 makes this comparison for the same current in coil used for the theory (no normalization used). The map along the z-axis agrees very well with the theory, though there is clearly still an un-shimmed linear gradient. The x-axis map includes a linear gradient as well, and an artifact of the perfect shield limit used in the theory. Note how the symmetric peaks are in nearly the same positions along the x-axis for theory and map, but the peak-to-trough amplitude is smaller in the map. A “perfect” shield would have an induced surface current density sufficient to cancel the radial component of the magnetic field inside the bulk of the shield (by the boundary condition  $B_\rho(\rho = \rho_{\text{shield}}) = 0$ ). An imperfect shield will have less surface current density, but located at the same radius. Thus, the higher-order gradients

caused by the induced current in the shield will be softer, but the relative positions of these features will be unchanged.

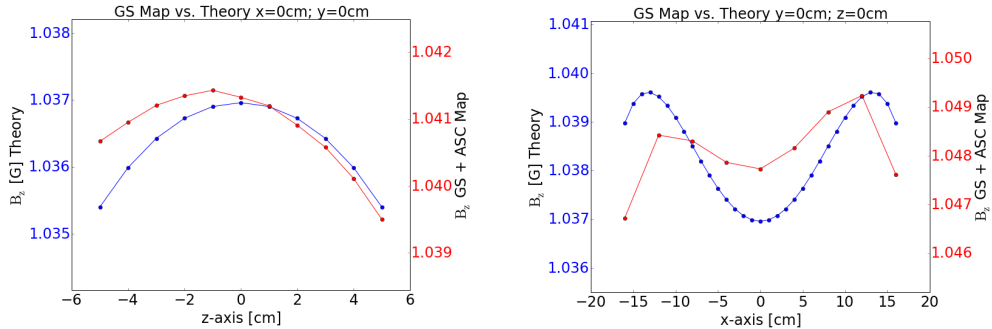


Figure 4.6: Theory vs. Map along the  $x$  and  $z$  axes of the gapped solenoid. The left axis scale is for the field map, the right axis scale is for the theory plot. The saddle coils used to trim the background field are included in the theoretical gapped solenoid plot.

The theory code is effective at predicting the general features of the field profile, but its limitations are evident. Furthermore, the “infinite, cylindrical” shield assumption is not accurate for finite shields with rectangular prism geometry, as will be used for the nEDM experiment. This dictates that the full design be performed in a more robust and general method, e.g., finite element analysis. Optimization using an FEA package, such as COMSOL, can be more time-consuming than this analytical model using Fourier transforms in Python. Thus, this method has value in setting a starting set of parameters and limiting the parameter space to be evaluated in COMSOL.

## 4.2 Current Optimizations in a Double-Gap Solenoid

It has been shown that adding a gap to a solenoid can increase the magnetic field uniformity by a “flux-return” type mechanism. A logical evolution is to then add more gaps to increase the axial length along which the magnetic field retains the desired uniformity. This geometry makes even more sense in the context of a double-chamber experiment as proposed: if the field is highly uniform in the gap region between two solenoids, and there are two volumes of interest, then having two gaps makes sense. A double-gapped solenoid (DGS) can be thought of as an inner coil and two axially symmetric outer coils. This symmetry for a centrally located fiducial volume then presents a new degree of freedom: modifying the current in the outer coils relative

to the inner coil. This can be thought of as a “flux focusing” type of mechanism, analogous to optics, capable of further reducing the average magnetic field gradients by a factor of  $10\times$ . This mechanism is identical to that shown in figure 4.1; however, by changing the magnetic flux from the outer coils relative to the inner coil, the flux inside the inner coil can be either compressed inward or expanded outward (“focusing” the flux) to further increase the magnetic field uniformity. A DGS geometry was thus chosen for the prototype apparatus built for a demonstration of the Ramsey method of separated oscillatory fields conducted at LANL.

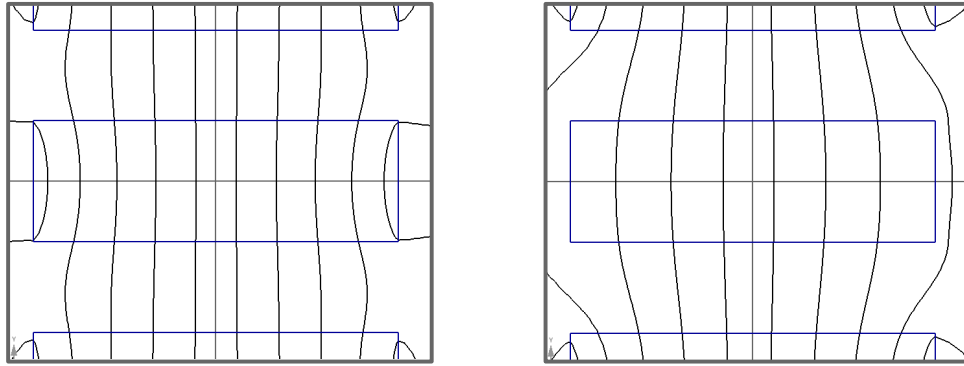


Figure 4.7: Contours of the vector potential are plotted for a DGS configuration of magnets. The blue lines represent edges of permanent magnets. Left: Inner and outer currents are equal. Right: Example with a substantially larger current in the outer coils relative to the inner coil. Note how the vector potential lines have gone from diverging to converging within the central coil.

For the Ramsey cycle demonstration  $B_0$  coil, an order of magnitude decrease in the volume average magnetic field gradients was predicted in COMSOL for the outer coils having a range 8% to 10% more current than the inner coil, as shown in figure 4.8. The current optimization of a DGS improves magnetic field uniformity comparable to the improvement the DGS provides relative to a solid solenoid.

Similar optimizations have been used in recent experiments, notably involving  $^{129}\text{Xe}$  EDM measurements [48].

A  $\cos\theta$  coil is typically used in experiments where magnetic field uniformity is important, because a current distribution on an infinitely long cylindrical shell which is proportional to the cosine of the azimuthal angle will produce a perfectly uniform field. When the length of the coil is comparable to the radius this approximation breaks down considerably. Nevertheless, it produces a very uniform field for finite lengths such that it is commonly used, and thus should be the benchmark for the

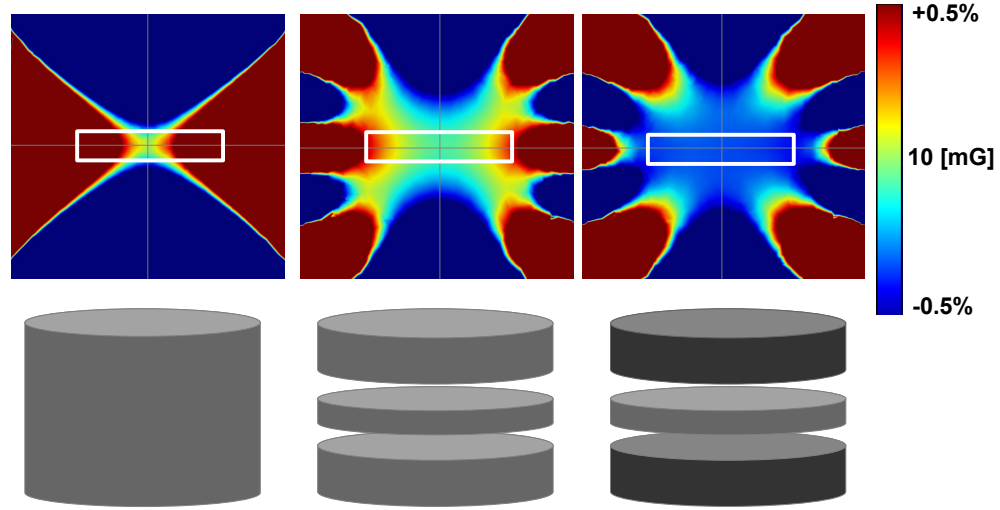


Figure 4.8: Comparison of a COMSOL model of the prototype  $B_0$  coil design for a solid solenoid (left), double-gapped solenoid (middle), and current optimized DGS with  $I_{\text{Outer}} = 1.1I_{\text{Inner}}$  (right). The colormap scale has a range of 1% of the central magnetic field value  $B_z = 10$  mG. The white box indicates the fiducial region.

optimized double-gap solenoid. For the same geometry as the DGS, a  $\cos \theta$  coil will produce a field transverse to the DGS; as a result, comparisons are made for a 30-turn  $\cos \theta$  coil in the same configuration as the DGS and rotated 90 deg as shown in figure 4.9.

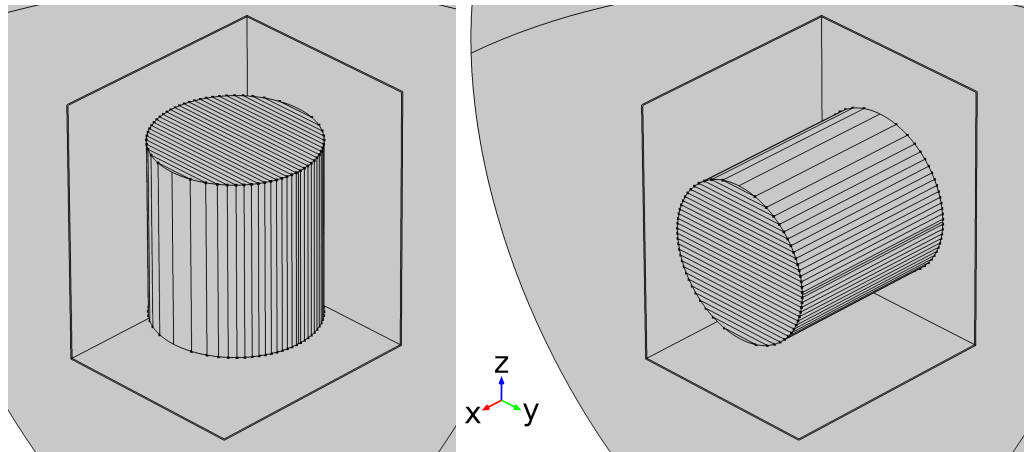


Figure 4.9: Geometry used for benchmark  $\cos \theta$  coils: The left geometry will produce a magnetic field along the  $x$ -axis; the right will produce a magnetic field along the  $z$ -axis.

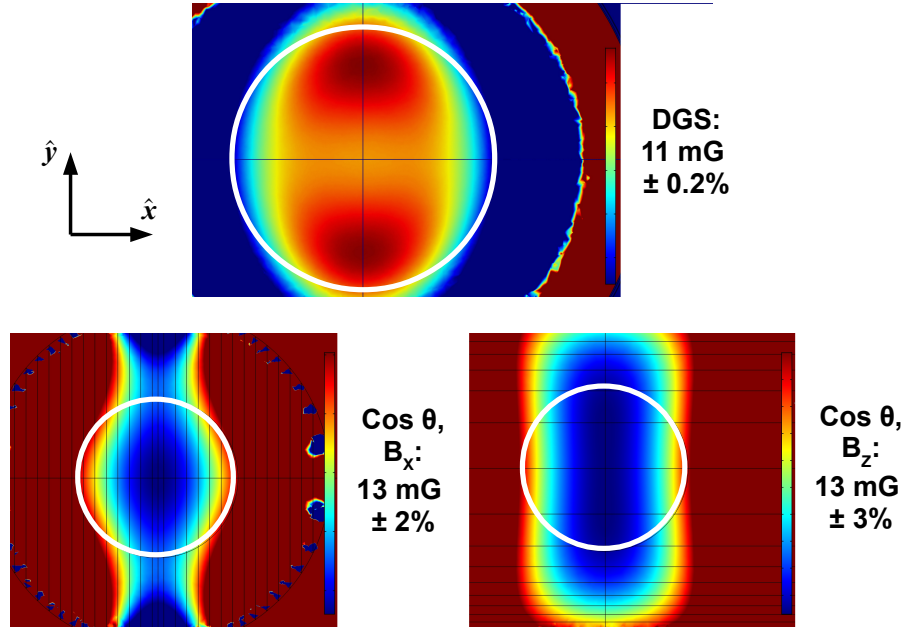


Figure 4.10: COMSOL model comparing a  $\cos \theta$  coil with the same dimensions and shielding as the prototype DGS (top) in the transverse ( $xy$ ) plane. The  $\cos \theta$  coil produces nominally a field perpendicular to the longitudinal axis (left); it can be turned on its side (right) to produce a field in the same direction as the DGS. The white lines indicate the fiducial region under consideration for a double-chamber experiment, for which the DGS is proposed to be superior.

Along the  $y$ -axis, the  $\cos \theta$  coil has a variance in the magnetic field  $\approx 4\times$  that of the DGS; however, along the  $x$  and  $z$ -axes, the DGS is easily an order of magnitude more uniform. Note this is a comparison to the DGS optimized for a single, central storage chamber rather than the 2-chamber design.

### 4.3 Ramsey Demonstration $B_0$ Coil

As a proof of capability towards a full neutron EDM measurement, an experiment designed to measure the Ramsey method of separated fields fringe was conducted at Los Alamos Neutron Science Center (LANSCE). In order to suppress the false EDM effect due to the motional  $\vec{v} \times \vec{E}$  field in the full EDM measurement, the specification for magnetic field uniformity is  $\left\langle \frac{dB_z}{dz} \right\rangle_{B_z(\vec{r}=0)} < 3.0 \times 10^{-6} \text{ cm}^{-1}$ . COMSOL models indicated it was possible to optimize the fractional gradient to  $\left\langle \frac{dB_z}{dz} \right\rangle_{B_z(\vec{r}=0)} < 1.0 \times 10^{-6} \text{ cm}^{-1}$  if the coil was built to just barely fit inside of the shield. It was determined that for this demonstration, the level of performance did not need to



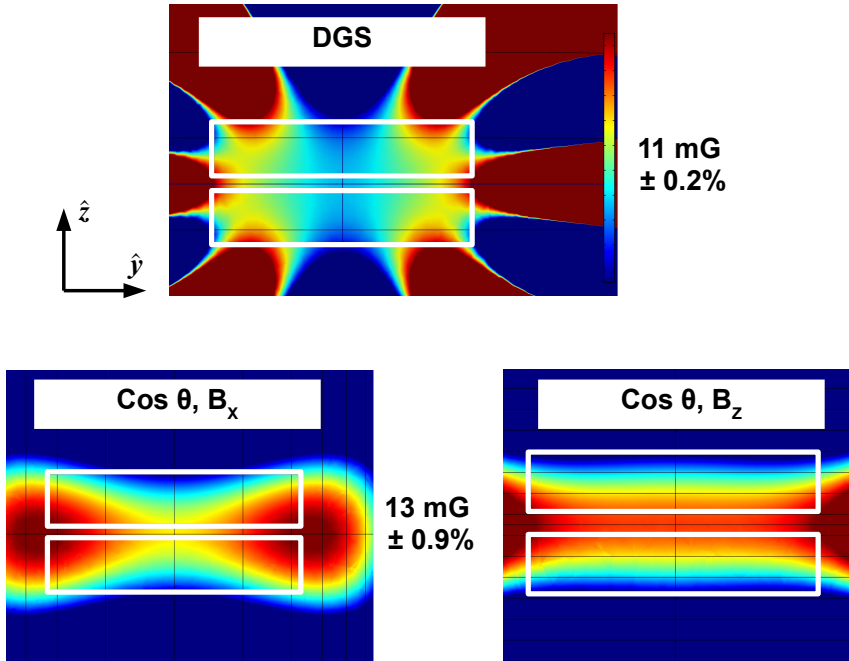


Figure 4.11: COMSOL model comparing a  $\cos \theta$  coil with the same geometry and shielding as the prototype DGS (top) in the longitudinal  $(yz)$  plane. The  $\cos \theta$  coil produces nominally a field perpendicular to the longitudinal axis (left); it can be turned on its side (right) to produce a field in the same direction as the DGS. The white lines indicate the fiducial region under consideration for a double-chamber experiment, for which the DGS is proposed to be superior.

meet the full experiment specification, considering only the magnetic field resonance is being measured and it is the false EDM effect which requires such a strict specification. The focus was then on a more easily constructed coil which nevertheless improves upon technical expertise for the full experiment.

### Prototype $B_0$ Design

An additional consideration is the interior dimensions of the shield. For this first demonstration, an existing shield was selected to accelerate the timing and minimize costs over having a new shield custom built. The interior dimensions of this shield are  $52 \frac{3}{4}$  in (W)  $\times$   $60 \frac{1}{4}$  in (L)  $\times$  70 in (H). Ideally, the coil should be as large as possible to improve the uniformity; however, there must be additional space to allow for maneuvering the coil inside the shield and to allow for working room inside the shield.

The coil dimensions were set at a diameter of 42 in and a total length of 47 in.

Constraints for the inner coil and gap lengths were set by the positions and dimensions of the UCN guide and storage cell. Using the techniques of sections 4.1-4.2, the dimensions were optimized within the allowable range: inner coil length = 7 in; gap length = 6 7/16 in; outer coil lengths = 12 3/4 in. The winding surface frames were composed of fiberglass-reinforced plastic (FRP) from a vendor. To provide additional structure, a set of flanges was cut from 1.5 in thick laminated bamboo sheets with an inner diameter matching the outer diameters of the FRP frames to within 1/16 in, and outer diameter 1.5 in larger. These were attached to the top and bottom of the FRP tubes using brass screws. 18AWG gauge, solid core copper, enamel-coated magnet wire was wound on the outer surface of the FRP frames between the two flanges. The separate pieces were connected via fiberglass threaded rods, using thick fiberglass tubes cut to the required gap length to support the weight of each section. The complete  $B_0$  coil assembly inside the shield is shown in 4.12.



Figure 4.12: Double-gapped solenoid inside shield. The two vertical struts in the foreground, resting on the top of the  $B_0$  frame, are rectangular fiberglass frames which support the spin-flipping  $B_1$  coils.

## Simulated $T_2$

Using the simulation discussed in chapter 3, the transverse spin relaxation time was determined for the theoretical coil. As discussed in section 3.4, the spin relaxation is highly dependent upon the velocity distribution of the neutrons. Figure 4.13 compares the distribution of the transverse plane polarization angle  $\phi$  for the prototype  $B_0$  coil, using the analytical fit model discussed in section 3.3, for maximum UCN velocities of 7 m/s and 5 m/s, both using a  $P(v) \propto v^2$  distribution.

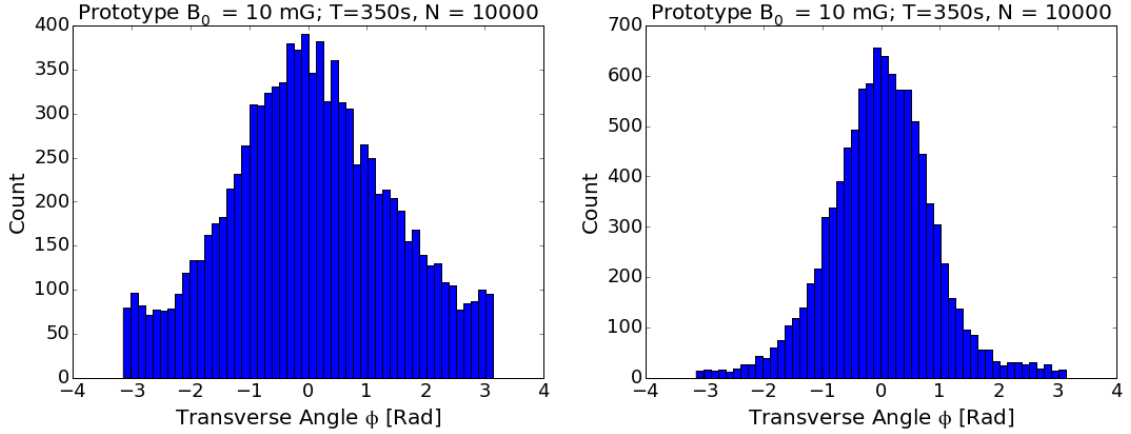


Figure 4.13: Histogram of the transverse polarization angle,  $\phi$ , after 350 s of free precession for the prototype  $B_0$  coil set to produce a 10 mG field. The left histogram is for the upper velocity cutoff of the velocity distribution  $v_{\max} = 5$  m/s; the right histogram is for  $v_{\max} = 7$  m/s.

As expected from the discussion in section 3.4, the spin relaxation time is shorter for slower neutrons. The results of these simulations are: for  $v_{\max} = 7$  m/s,  $T_2 \sim 850$  s; for  $v_{\max} = 5$  m/s,  $T_2 \sim 350$  s.

## Preliminary $B_0$ Mapping

After fabrication and assembly of the prototype  $B_0$  coil, a series of magnetic field maps were collected using a Bartington MAG-03MSESL triple-axis fluxgate magnetometer mounted along a rail which defines the x-axis, with 6 available positions along the y-axis and 3 positions along the z-axis. This map was collected upon coil completion and prior to assembly of the storage chamber, so that only the  $B_0$  coil was inside the shieldhouse, which itself was in a staging area separate from the experiment hall. After degaussing the shield, a background map was taken with the  $B_0$  coil turned off. A set of field cancellation coils was not used for the Ramsey demonstration, so

that background reduction was only dependent on the shield. The manufacturer label indicated a minimum performance for field attenuation of  $\frac{H_{\text{Outside}}}{H_{\text{Inside}}} \geq 100$ , which was confirmed by comparisons of the field measured inside and outside of the shield. As shown in 4.14, the result is background fields on the order of several percent of the nominal  $B_0 \approx 10$  mG, with gradients an order of magnitude larger than the designed  $B_0$  field gradients.

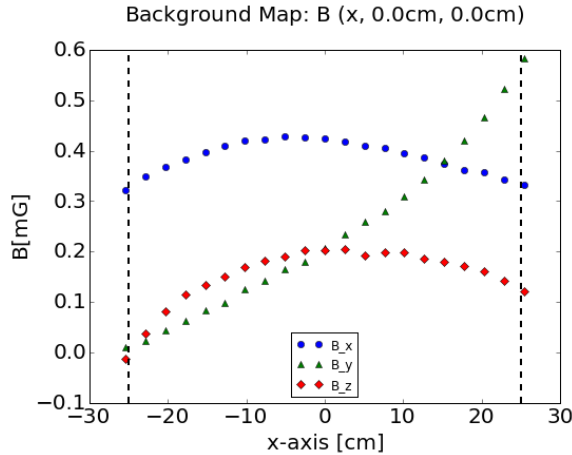


Figure 4.14: Measured background inside shield after degaussing. Dashed lines indicate the edge of the fiducial region.

In order to evaluate the performance of the  $B_0$  coil, the nominal field was increased an order of magnitude to increase the magnetic field profile above the backgrounds. To verify the performance of the current optimization, maps were taken with the current ratio at 100% ( $I_{\text{outer}} = I_{\text{inner}}$ ) and 110% ( $I_{\text{outer}} = 1.1I_{\text{inner}}$ ).

The results clearly indicate the effectiveness of the optimization techniques: adding appropriate gaps in a solenoid will substantially improve the uniformity in a larger volume as compared with a solid solenoid, especially useful along the length or as a method to shorten a solenoid; and the flux can be focused to further increase the uniformity within a specific region by altering the current in respective sections of coils. The magnetic field profile along the mapping axis shows very good agreement with the COMSOL model. The other axes did not have enough resolution to make any statement regarding their comparison with theory.

A statement on the volume average gradient could not be made for two reasons: 1. The background gradients still contributed a gradient which was on the order of the designed gradients in  $B_0$  even with the magnetic field scaled; 2. There was a large gradient along the vertical axis which was discovered in the analysis process that had not been shimmed.

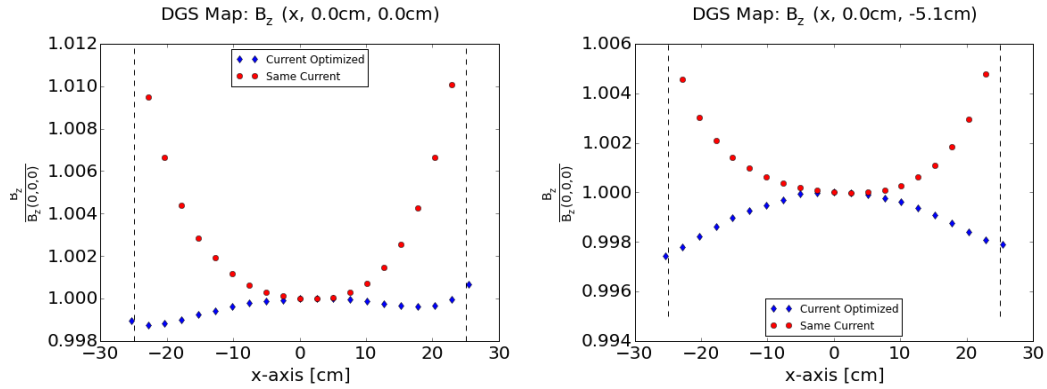


Figure 4.15: Comparison of DGS with current optimization and without (current in inner and outer coils is the “same”) along x-axis. Dashed lines indicate the edges of fiducial volume, and fields are normalized to the central value.

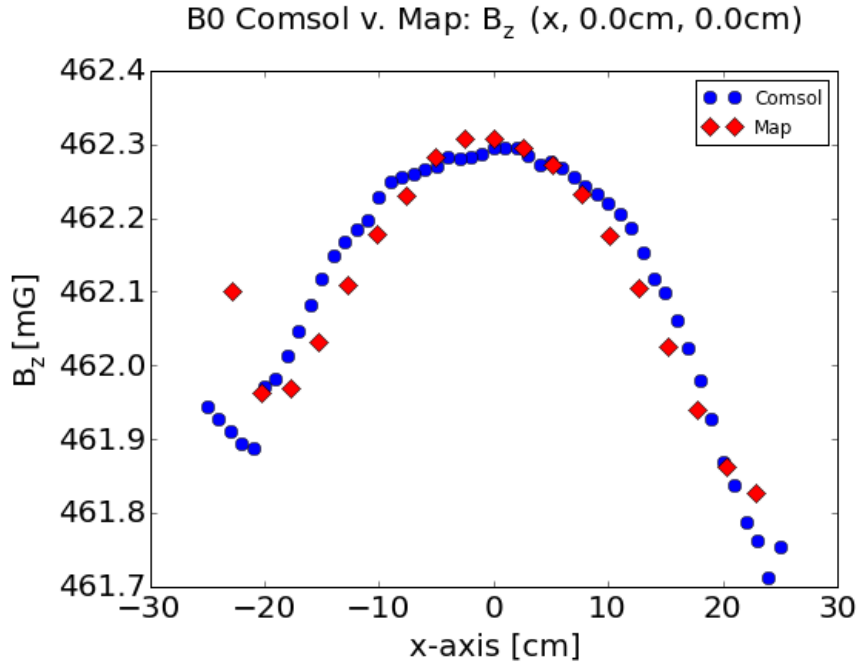


Figure 4.16: Measured  $B_0$  coil at 110% current ratio compared to COMSOL model.

The vertical gradient was studied after the data collection, and is the result of the  $B_0$  coil not being centered within the shield as designed. The offset was  $\sim 3$  in, and due to the requirement that the static UCN guide be aligned with the solenoid gap it could not be centered. The sources of this gradient are the induced surface currents in the magnetic shield which distort the magnetic fields similar to the “flux focusing” mechanism discussed previously. This can be used to the advantage of

magnetic field design by use of magnetic endcaps as previously discussed. However, when the magnetic source is not centered relative to the shield, the symmetry of the magnetic field is broken resulting in stronger magnetic fields where the coil is nearer the shield and weaker in the region farthest from the shield. In the fiducial region, this produced a linear gradient along the length of the coil. This was subsequently shimmed via addition of 10-turn coils to the top and bottom of the  $B_0$  coil and wired in an anti-Helmholtz configuration (though not at Helmholtz spacing by constraints).

The vertical offset had a severe negative impact on the magnetic field uniformity. The current loop pair shim produced an approximately linear field along the z-axis, but it also produces gradients along the transverse axes which are considerably larger than those resulting from the  $B_0$  coil. Additionally, the linear gradient it does produce is only approximately linear for a narrow region along the z-axis, until higher order terms contribute at a larger radius.

Table 4.2: Target nEDM uniformity compared with the prototype COMSOL models, centered and 3-in offset with z-shim.

$$\left\langle \frac{\frac{dB_z}{dz}}{B(\vec{r}=0)} \right\rangle$$

nEDM Target	$\leq 3.0 \times 10^{-6} \text{cm}^{-1}$
Centered	$5.6 \times 10^{-5} \text{cm}^{-1}$
Offset	$7.3 \times 10^{-4} \text{cm}^{-1}$

Placement of the coil offset from the center of the shield is a problem, but study of this effect demonstrates an interesting potential method of shimming magnetic fields in future experiments. If the addition of linear gradients or the cancellation of stable background gradients are desired, the coil could be mounted on adjustable kinetic mounts. By adjusting the position of the coil relative to the center of the shield, the induced currents in the shield can be used to produce very uniform linear gradients. Figure 4.17 demonstrates this effect, producing linear gradients in the  $\hat{z}$  component of the field.

It is interesting to note that the radial offset results in a far smaller gradient than the vertical offset. The reason for this is that the magnitude of the magnetic field on the top / bottom is  $\approx 100\times$  the magnitude on the sides, which means the induced surface currents in the shield will be similarly smaller on the sides. Addition of coils to shim  $\frac{dB_z}{dz}$  is simple via addition of large circular loops wound on each end of the coil. Shimming  $\frac{dB_z}{dx}$  and  $\frac{dB_z}{dy}$  requires shim coils with more complex geometry, which also tend to produce undesirably large off-axis components. Controlling the

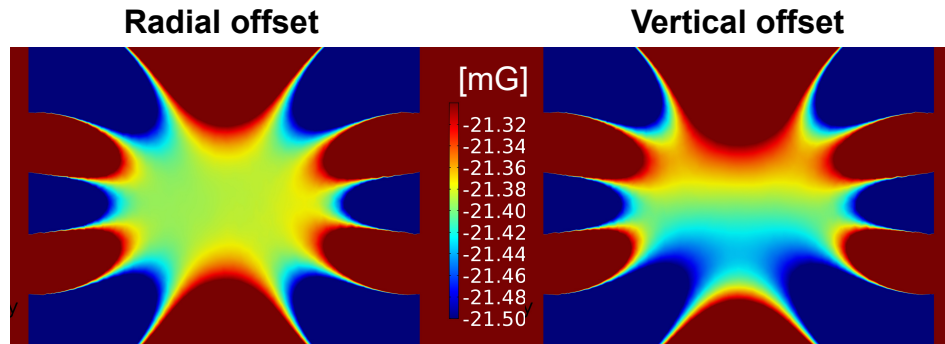


Figure 4.17: Comparison of separate radial and vertical offsets of 1 in between the center of the coil and the shield. The same color scale is used for each.

offset is a promising method of avoiding such side-effects. The effective range of uniformity must be considered for the  $B_0$  coil if this method were used. e.g., If the field only achieves the uniformity specification in a radius of  $\rho_{\max}$ , then the maximum displacement for shimming purposes must be limited to  $\Delta_{x,y} \leq |\rho_{\max} - \rho_{\text{cell}}|$ . Based on studies of asymmetric v. symmetric magnetic field profiles, it may actually be beneficial to have a slight offset so that the magnetic fields are no longer azimuthally symmetric (see section 3.5). For the two-chamber experiment design, there might be some concern about vertical offsets creating different Larmor frequencies in each chamber. Co-magnetometers are used so that the leading order resonant frequency due to the magnetic fields alone can be determined. However, separate spin analyzers must be used for counting the neutrons in the top and bottom chambers separately in order to account for the systematic shift induced by these gradients. Use of separate analyzers is a good idea in general because it is likely there will be some very small shift in the average magnetic field for each chamber.

#### 4.4 In-Situ Mapping

##### Mapper Design

In the experiment hall, the shield was elevated  $\sim 6$  ft above the floor to align it with the UCN source guide. Combined with the presence of the UCN storage chamber, the manual mapper using a rail was not achievable. A custom triple-axis mapper was designed and built so that the magnetic field could be measured in-situ with all of the equipment in place. There were two discrete sections of hardware components:

a setup inside the shield which would support and move the probe and required all non-magnetic materials; and an external setup which contained the stepper motors used to actuate motion.

The internal setup of the mapper is comprised of an aluminum plate supporting a rotating sub-assembly, shown in figure 4.18. A cylindrical shaft made of UHMW, a grade of plastic with a low coefficient of friction, passes through a 4 in hole in the aluminum plate, connecting top and bottom plates made from acrylic on each side with brass bolts. A teflon thrust bearing is placed between the acrylic top plate and aluminum base to support the rotating assembly weight. Kevlar string is wound on the top of this shaft, with ends exiting on opposite sides of the shaft to enable rotation in either direction via tension. The kevlar string is guided out of the shield through a small port using a system of bronze pulleys. A single stepper motor, a Velmex PK296, can then control the angle of the rotating assembly relative to the aluminum plate. This motor has discrete steps of 1.8 degrees; with a 2 in spool mounted to the motor shaft used to wind the string, this corresponds to 0.9 degree steps in the rotating assembly.

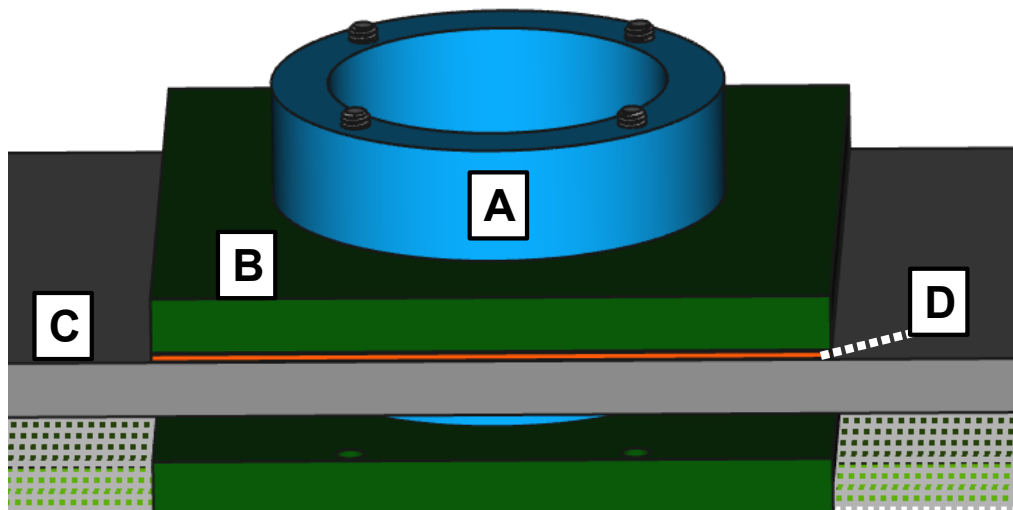


Figure 4.18: Rotating assembly: A) Hollow UHMW shaft; B) Acrylic top / bottom plates; C) Aluminum base; D) Teflon thrust bearing.

Mounted on the bottom plate of the rotating assembly is a frame made of 1/4 thick G10 strips, shown in figure 4.19, which supports one of two mapper styles. For field monitoring during data collection, fluxgate magnetometers are directly mounted to slits in the vertical G10 rails. Kevlar strings support the weight of the magnetometers, using the balance of weight and tension to control the height via adjustments to



the string length. Individual Velmex P264 stepper motors control the string lengths, with 1.8 degrees per step and 1.5 in spools resulting in 1.1 mm per step control. In this configuration, multiple sets of boundary conditions sampled from a cylindrical shell can be taken per data collection cycle.

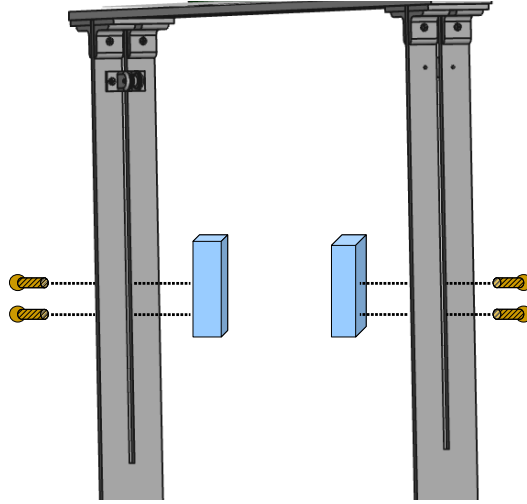


Figure 4.19: Diagram showing how the triple-axis magnetometers mount to slits in the vertical rails via brass screws for boundary value measurements. Screws hold the probe flush to the vertical rail, and there is clearance between the slit and the screws so that they are free to slide vertically. String connects at the top of the probe to set height.

For in-situ volume mapping, the configuration is as shown in Fig. 4.20. UHMW end caps are mounted to and free to slide along each vertical rail. A horizontal rail made of UHMW is clamped on each end to the endcaps, and a holder made of PVC, which supports a single magnetometer, is supported by and free to slide along the rail. Kevlar string from individual stepper motors is routed through additional bronze pulleys mounted to the end caps, and connects to each side of the PVC probe holder. In this configuration, coordinated motion of the two PK264 motors can be used to change the vertical position of the end cap / rail / probe sub-assembly, or to control the radial position of the PVC probe holder along the rails.

Consider the strings connected to each end of the PVC holder to have lengths  $l_1$  and  $l_2$ . For the ideal case, in which the lengths of each string are simultaneously changed at the same rate and by the same amount, then the position can be “easily” controlled as in equations 4.15.

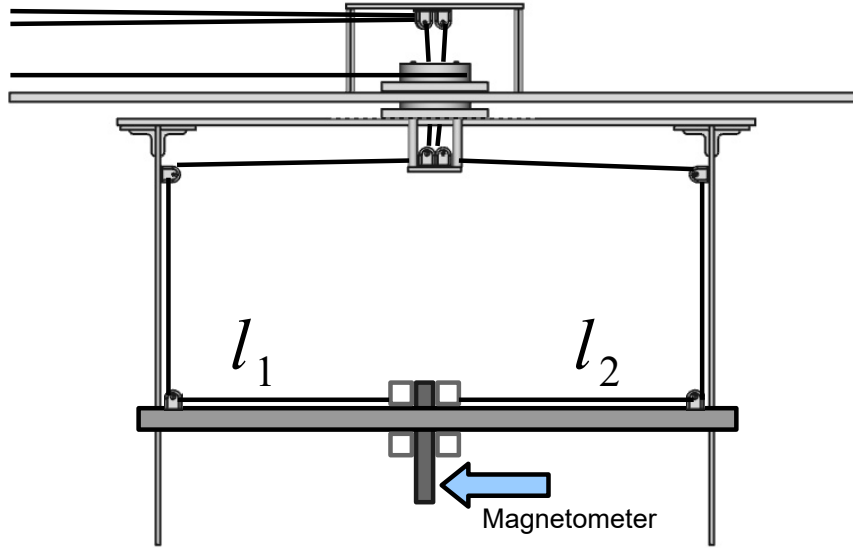


Figure 4.20: Overview of internal assembly as setup for collecting volume maps.

$$\begin{aligned}\Delta z &= \Delta l_1 = \Delta l_2 \\ \Delta \rho &= \Delta l_1 = -\Delta l_2\end{aligned}\tag{4.15}$$

Appropriately synchronized motion was achieved, but difficulties arose as a result of motor backlash for vertical motion and horizontal rail tilting for radial motion.

When moving the sub-assembly vertically up, backlash in the motor between the moving state and holding state would cause an inconsistent amount of drop in the position. This seemed to be a consequence of the torque applied during the moving state being higher than the holding state when the string was wound onto the spool. When unwinding, the motors never had any backlash (i.e.- when the moving state of the motor had lower torque than the holding state). This allowed for a software countermeasure: when moving up, the motors were instructed to take additional steps above the desired position, then to step back down. This allowed all vertical adjustments to finish with a transition to the holding state from the lower torque unwinding condition, preventing all backlash.

A similar countermeasure was applied to the problem of rail tilting. Due to some slight looseness between the end caps and the vertical G10 rails, the horizontal mapping rail could tilt up to 1 degree, with the direction of motion being the side which

tilts up (i.e.- the end at which the string is decreasing in length). The maximum angle was not immediately reached but rather took several centimeters of radial motion to peak. This allowed the rail to be effectively leveled by using a decaying oscillation about the desired radial position.

A controlling program was written in C++. Bartington Mag-03MSESL triple axis magnetic field probes were used, connected to Bartington signal conditioning units. The SCU output was wired to a Measurement Computing USB-2416 ADC in single-ended mode with all grounds connected to the ADC ground. Two Velmex stepper controller units were used to control the motors. The ADC and controllers were connected to a computer via separate USB cables. Firmware was available with the controller and ADC for Windows, but was not Linux compatible. A Windows graphical interface was written to adjust settings and manually control the motors for calibration. A routine was written to automate the boundary value and volume map functions. At each data collection point, a series of 10 measurements of the magnetic field, separated by 5 ms each, was used to validate stability of the reading. The average and standard deviation of each measurement for all three components and the probe coordinates were output to a tab-delimited text file for offline analysis.

## **In-Situ Results**

After installation and calibration of the volume mapper, a series of maps were collected with the UCN storage cell top-plate removed. This allowed for measurements close to the cell walls and valve to check for local perturbations caused by potential magnetic material contamination. The center of the storage cell was set as the origin of the coordinate system. Initial results along the “x-axis”, defined as the axis parallel to the UCN guide, indicates some asymmetric perturbation that gets stronger near the bottom of the storage cell, as displayed in Fig. 4.21.

This same feature is present in the background, and appears to have the same amplitude in both cases. Fig. 4.24 shows the  $B_0$  field with background subtracted at various heights, which results in a very flat magnetic field profile as designed.

Volume maps were also collected for  $B_0 = 222$  mG, which included the same characteristic perturbation as shown in Fig. 4.25, increasing in amplitude near the bottom center of the cell. Such a feature, which is independent of the applied magnetic field, is characteristic of a magnetically saturated material. The UCN port is in the center bottom, and a valve apparatus directly below the port. It was discovered that the valve bellows was a grade of stainless steel, and was subsequently replaced with a titanium bellows.

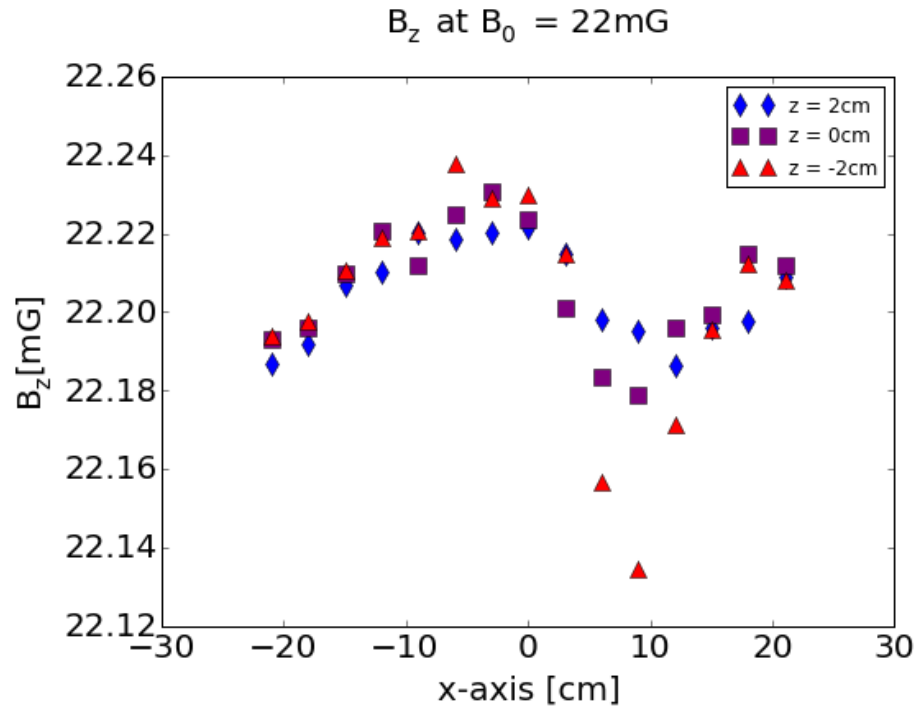


Figure 4.21: Comparison of  $B_0 = 22$  mG along the x-axis at different heights.

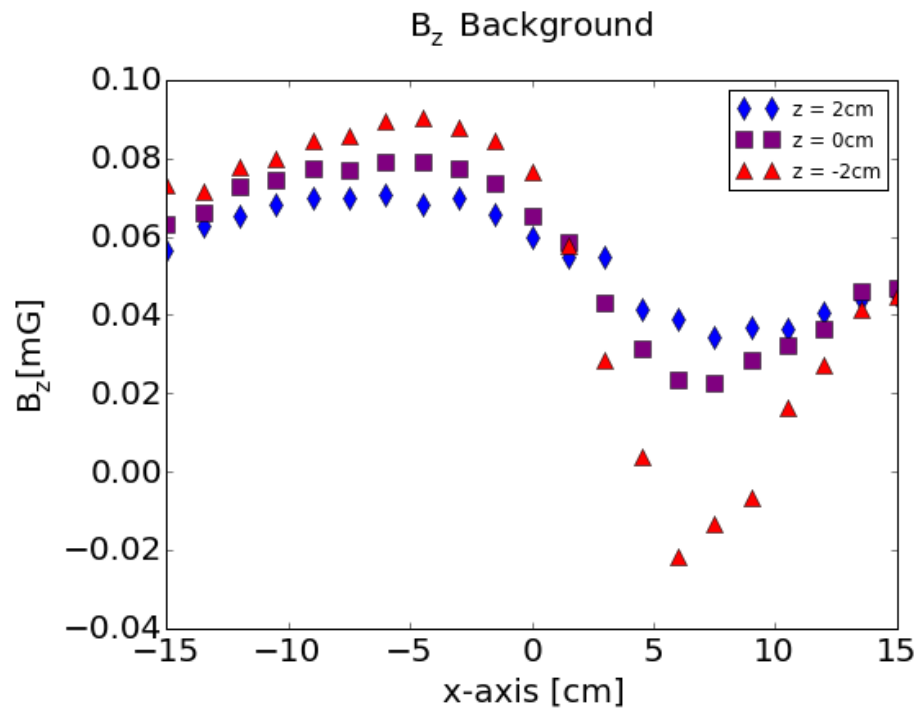


Figure 4.22: Comparison of background along the x-axis at different heights.

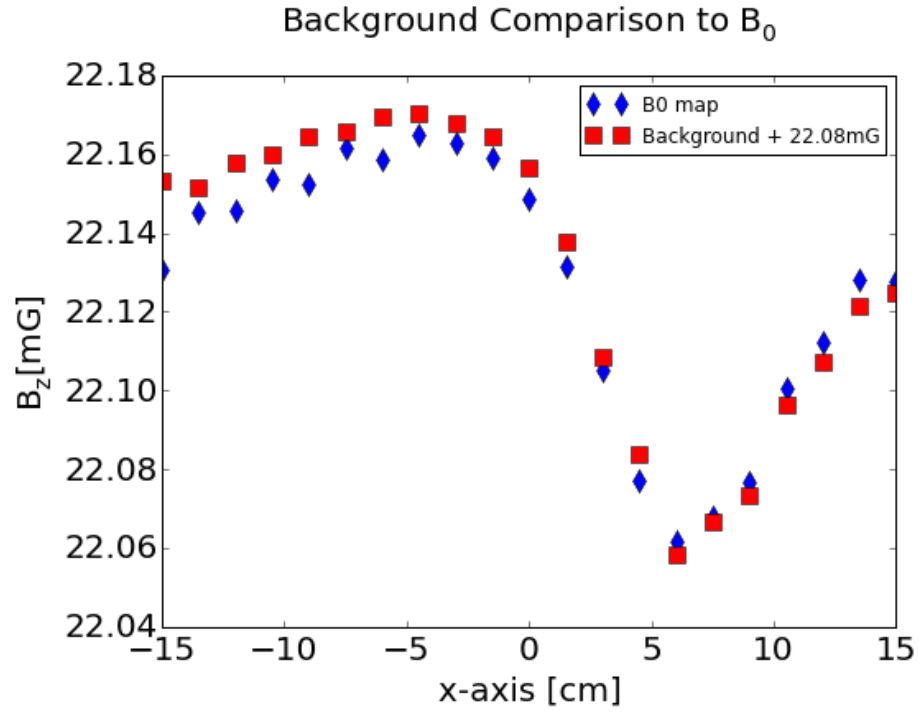


Figure 4.23: Comparison of  $B_0$  to the background with a constant 22.08 mG offset.

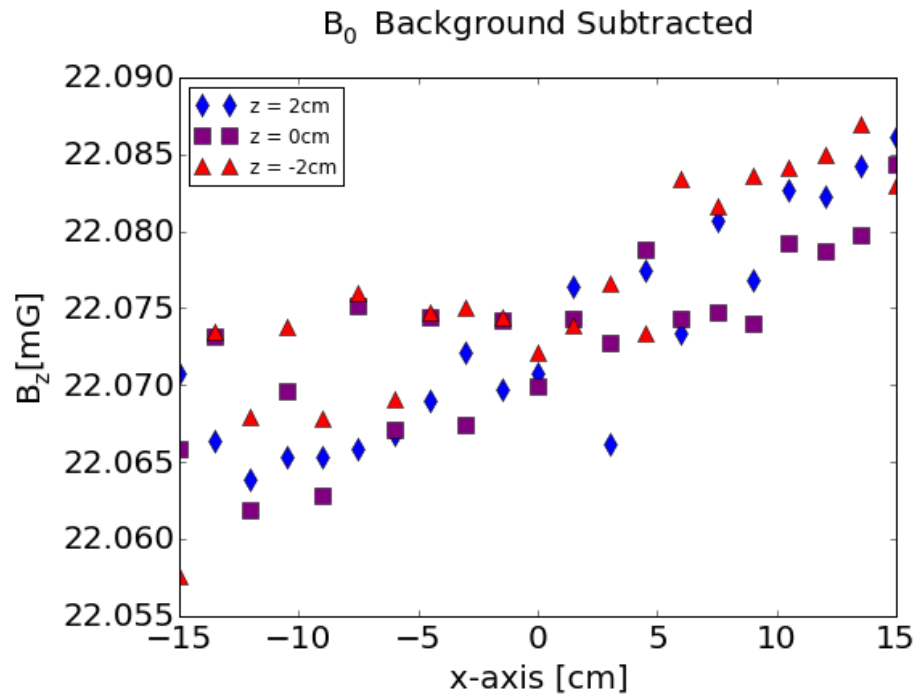


Figure 4.24:  $B_0$  with background subtracted at different heights.

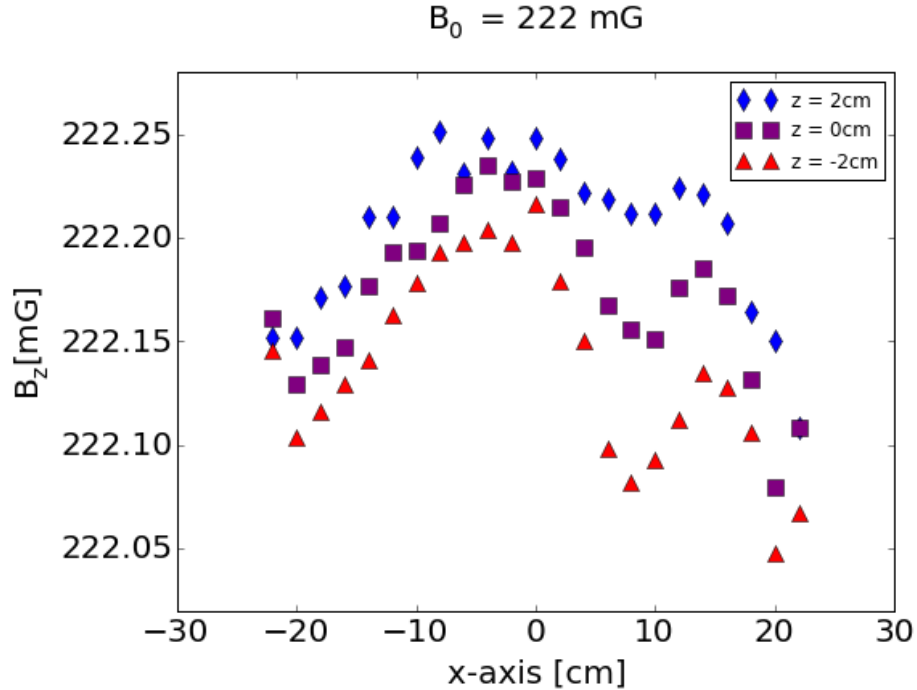


Figure 4.25:  $B_0 = 222 \text{ mG}$  at different heights.

#### 4.5 Full-size Neutron EDM $B_0$ Design Recommendations

Magnetic shields can be very expensive, upwards of \$1M, which makes efficient use of the volume crucial. It is also important to have as large a storage container as possible in order to minimize the number of wall collisions, which can cause depolarization or loss of neutrons through upscattering and absorption. Multi-gap solenoids using current optimization can help to reconcile these conflicting considerations. Flux focusing reduces the importance of solenoid length for field uniformity requirements, which makes the footprint, i.e.- the circular area for a cylindrical cell, the more critical parameter for setting the dimensions of a coil. A shorter shield with a wider footprint is beneficial for several reasons.

Higher order terms in the field expansion result in large gradients near the coil, e.g.,  $B \propto r^6$ . When the radius of the fiducial region is similar in size to the radius of the coil, higher order terms will always have an impact. Additionally, due to the  $\rho^2$  dependence on area, the higher radius regions make up more area per differential segment  $d\rho$ . Increasing the footprint of the solenoid reduces this effect.

An added benefit lies in spin-transport. A UCN guide passing from outside to inside the coil will experience a zero crossing, which will cause depolarization. A coil with sufficiently large radius allows enough space for a holding field to be maintained

up to the coil, then tapered to zero toward the center of the coil to promote adiabatic spin transport.

Preliminary work has been completed in designing a full-size, multi-gap solenoid for implementation of a full double-chamber neutron EDM experiment. A full optimization cannot be completed yet, as the chamber, electrode, guide, and shield designs have not been finalized as of this writing; thus, the related constraints on the gap positions are undetermined. Meeting the uniformity requirements to suppress the false EDM effect should be easily accomplished used multi-gap solenoids with current and gap length optimizations.

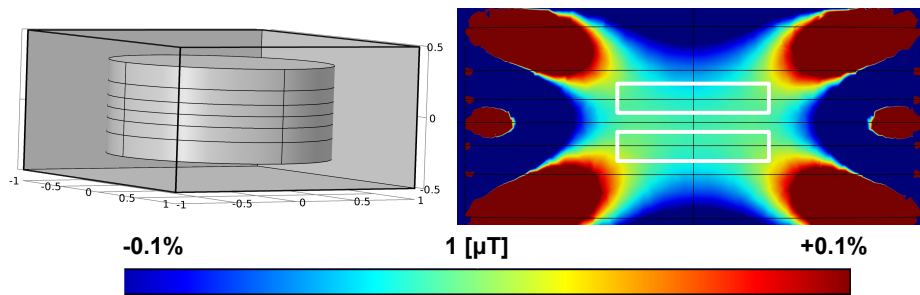


Figure 4.26: Concept multi-gap solenoid with current optimizations. Colormap indicates the nominal field component with a scale of  $\pm 0.1\%$ . Shield dimensions are  $2\text{ m} \times 2\text{ m} \times 1\text{ m}$

## Chapter 5 LANL Ramsey Cycle Demonstration

As a proof of capability to perform a neutron EDM measurement prior to the final design of the experiment, a prototype apparatus was built to measure the Larmor precession frequency for neutrons in a magnetic field using the Ramsey method of separated oscillatory fields. A summary of the experiment setup is presented, followed by a brief discussion of the results [49].

### 5.1 Setup

One key component driving design considerations for this test, especially important to the magnetic field source, was the magnetic shield. There was an existing, unused shield at Los Alamos which was loaned to this test with interior dimensions 52 3/4 in (W)  $\times$  60 1/4 in (L)  $\times$  70 in (H). This constrained the dimensions of any coils to maximum radius  $r < 64$  cm and total length  $L < 177$  cm, without giving extra space between the coil and the shield wall. Considering the magnetic field only needed to be uniform enough to maintain polarization for this test and in order to allow extra space for working and support structures, the decision was made to use a smaller coil with radius  $r = 21$  in  $\approx 53$  cm and total length  $L = 120$  cm.

The  $B_0$  gap lengths were optimized as discussed in chapter 4, with the UCN guide diameter and position setting constraints on the gap lengths and positions, resulting in the optimized inner coil half-length of 9 cm and gap length of 16 cm. Current was supplied by a Keysight B2962A low noise, 2-channel DC power supply; one channel was used to power the center section of the coil at 2.45 mA, and the other channel powered the outer coils at 2.6705 mA, the optimum current ratio being 9% more current in the outer coils relative to the inner.

For simplicity, the  $B_1$  coil used to generate the transverse oscillating field for the  $\pi/2$  spin flips was constructed as a rectangular coil pair of dimensions 48 in  $\times$  52 in, separated by 30 in. A Stanford Research DS345 signal generator synchronized to a Stanford Research FS725 rubidium frequency standard is used to apply voltage for the RF pulses with precise frequency and phase control [49]. The spin-flip efficiency was simulated using a model of the  $B_1$  coil and found to be  $\approx 99.995\%$ . Simulation was used in lieu of measurement due to polarization losses in spin-transport; the magnitude of the on-resonance asymmetry measurement of the Rabi fringe shown in figure 5.6 agrees with the asymmetry measurement for similar holding times in the



$T_1$  measurement shown in figure 5.5, supporting the simulation results for spin-flip efficiency.

An aluminum frame supports the UCN storage chamber and  $B_0$  coil. The lower section of the coil is installed prior to the UCN chamber, which is then connected to the guide. The middle and upper sections of the coil are then attached, and the mapper is fastened with aluminum dowel pins to the top of the  $B_0$  frame.

The UCN source is surrounded by lead and concrete biological shielding, and UCNs are piped out via a stainless steel guide coated with nickel-phosphorus to decrease UCN losses. A gate valve is upstream of a superconducting 5 T polarizing magnet. As shown in section 2.2, magnetic fields coupling to the spin changes the energy of UCNs such that nearly 100% polarization can be obtained with a 5 T field. A rotating switcher is between the polarizer and magnetic shield, and connects the UCN guide from the source to the storage chamber during loading, then “switches” at unloading to connect the chamber guide to an analyzer. This overall setup is displayed in Fig. 5.1.

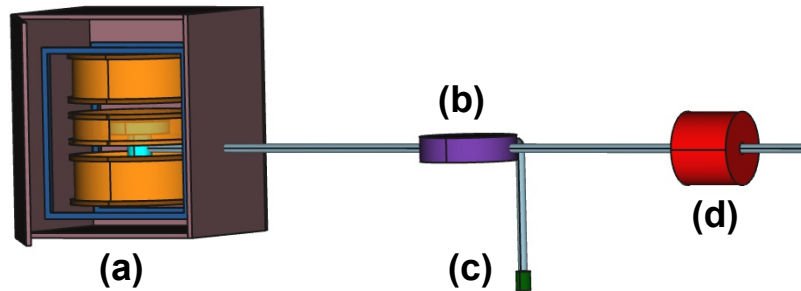


Figure 5.1: Ramsey measurement general apparatus: (a) magnetic shield; (b) switcher; (c) analyzer; (d) polarizer.

The UCN guide passes through a hole in the shield aligned with the lower gap of the  $B_0$  coil, approximately 17 cm below the center. Outside of the shield, there are holding coils mounted onto the guide in multiple locations which produce a nominal field of  $\approx 5$  Gauss along the length of the guide to maintain longitudinal spin polarization. The  $B_0$  field is oriented perpendicular to the guide, so that the polarization must be rotated as UCNs enter the cell. An argument was made that the fringe fields from the coil would be sufficient to perform this task. However, there is an abrupt change in the field from just outside to inside the shield which can cause depolarization, and the  $B_0$  coil produces a zero crossing in the gap between sections. Early

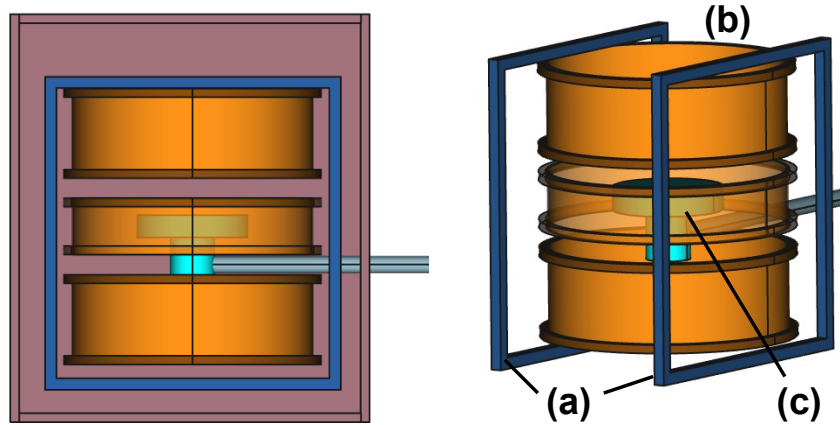


Figure 5.2: Apparatus inside shield (excludes support structures), side view (Left) and angle view (Right): (a)  $B_1$  coils; (b)  $B_0$  coil; (c) storage cell.

tests indicated that neutrons were not maintaining polarization during loading and unloading, demonstrating poor spin transport.

The simplest solution was to use a series of solenoids along the guide with radii a few centimeters larger than the guide, each  $\approx 5$  cm in length, as shown in Fig. 5.3. Two solenoids were used between the  $B_0$  frame and the shield wall to produce a constant holding field. Three more solenoids were inside of the  $B_0$  frame and produced a field which decreased linearly to zero at the center. Superimposed with the  $B_0$  field, this results in a magnetic field vector which points radially inward at the  $B_0$  coil frame and rotates along the guide until it is axial with the  $B_0$  frame at the center. This slow rotation along the guide allows for nearly adiabatic spin transport, that is the spins slowly rotate from polarization longitudinal to axial with the coil. Using these spin-transport coils (STC) produced a measurable polarization of  $\sim 30\%$  after loading then unloading the cell with no holding time.

Several novel spin analyzers are proposed for the full nEDM experiment; for this prototype apparatus, a well established method similar to that used in the previous ILL result was used. A thin film of iron is deposited on a silicon substrate attached to an ionization chamber filled with  $^3\text{He}$  gas. The iron is magnetized using permanent magnets attached to the edges. The magnetization is not enough to produce a large external field, but on the scale of nanometers from the surface, this field can be as large as several Tesla. The result is that spin-up neutrons are passed through the thin film, and spin-down neutrons are rejected (within some efficiency).  $^3\text{He}$  captures neutrons with a large cross-section, releasing  $\sim 764$  keV via  $^3\text{He} + n \rightarrow ^3\text{H} + p$ .

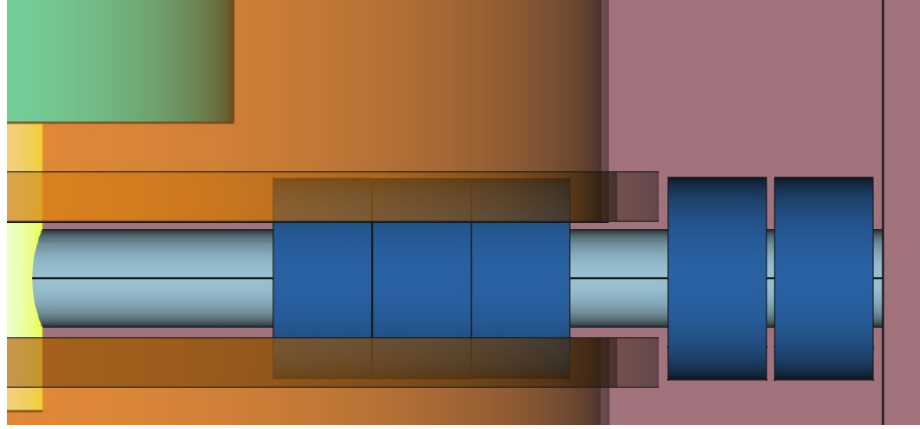


Figure 5.3: Spin transport coil placement (five total, blue).

## 5.2 Measurement Cycle

A single measurement cycle begins with a 50 s loading period. The spin-transport coils are turned on, the cell-valve is opened, and UCNs are guided from the source into the storage chamber. The current in the STCs is linearly decreased to zero over 5 s once the cell valve closes, to prevent perturbations to the magnetic field in the chamber which might cause depolarization. What occurs next is dependent on the measurement being conducted. Common to all measurements is the unloading process.

Five seconds prior to the cell valve opening, the current in the STCs is linearly ramped up to prepare for spin transport. The switcher rotates to the appropriate position to connect the storage chamber to the spin analyzer. Only a single spin state can be counted at a time, as the wrong polarization is reflected by the analyzer foil. In order to count both spin states, unloading is split into two discrete times of length  $t_1$  and  $t_2$ . During one of these, a spin-flipper just above the analyzer will be turned on which converts spin-up to spin-down and vice versa. Depolarization and neutron losses in wall collisions will cause the second spin state measured to be under-counted. To correct this, measurements are made in “quads”, four consecutive measurement cycles where the spin state measured first will be changed, e.g., “up, down, down, up”. A composite measurement for a quad is shown in figure 5.4.

Loading and unloading were unchanged for different measurements. To measure  $T_1$ , quads are collected with different holding times. An exponential fit of the asymmetry as a function of holding time will give the longitudinal spin relaxation time,  $T_1$ . Transverse spin relaxation,  $T_2$ , can be measured similarly to the longitudinal spin relaxation, with the addition of on-resonance  $\pi/2$  spin flips at the start and end of

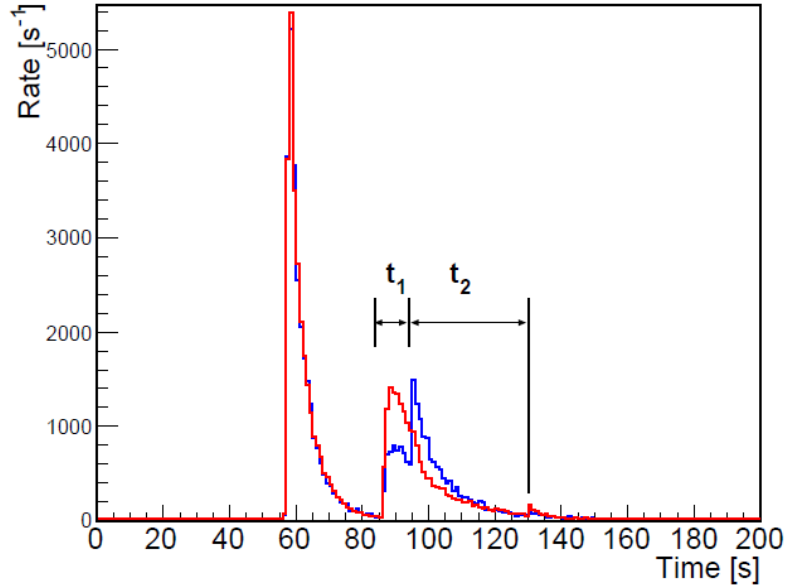


Figure 5.4: Combined quad measurement for a 30 s holding time. The initial peak near 55 s is due to the switcher connecting the chamber, with the cell valve closed, to the analyzer. The result is any UCNs left in the guide and valve assembly pass into the analyzer. The cell valve is opened at 85 s; the final peak at 95 s is due to the analyzer spin-flipper turning on, allowing the remaining UCNs of opposite spin-state to be counted.

the holding time.

The resonant frequency was measured for  $B_0 = 22.2$  mG using both the Rabi and Ramsey methods. For the Rabi method, a  $\pi$  pulse is applied, after the STCs have ramped down. For the Ramsey method, two  $\pi/2$  pulses are separated by some free precession time  $T$ . The STCs ramp back up and the cell is unloaded to complete the Rabi measurement.

The analysis of the Ramsey method was detailed in chapter 2. Of interest was the discussion of using the co-magnetometer as a leading order estimate of the precession frequency. This was not implemented for this prototype test, so instead a pair of QuSpin scalar magnetometers were utilized, one located on the top center and the other on the bottom off-center of the exterior of the storage chamber. The average of these determined the  $\nu_0$  of equation 2.44, and was used to set the measurement frequencies  $\nu$ . Rather than perform a high-precision measurement of the resonant frequency, the Rabi and Ramsey fringes were measured by sweeping through a wide range in  $\nu$ .

### 5.3 Results

The results for  $T_1$  and  $T_2$  were extracted from exponential fits of the data shown in figure 5.5. Fits for  $T_1$  were conducted separately for each counting time  $t_1$  and  $t_2$ .

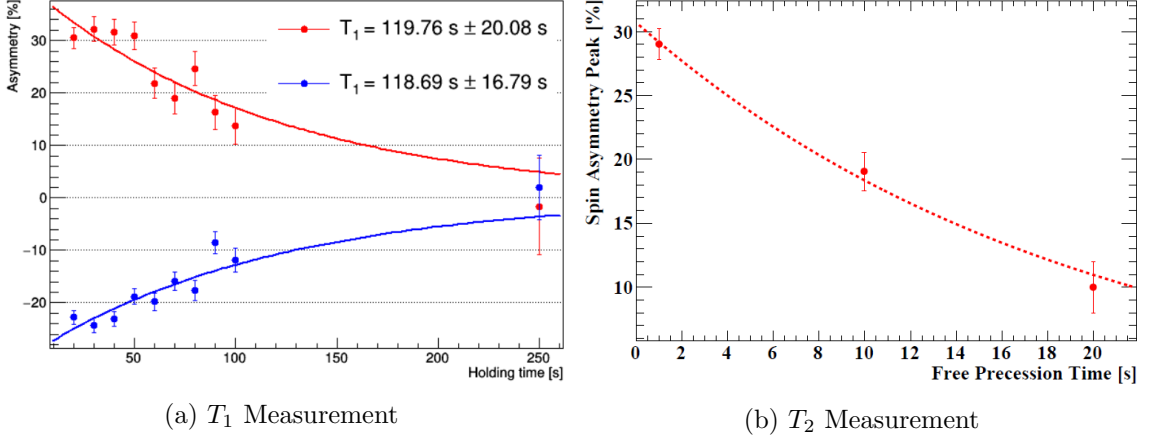


Figure 5.5: Measurements for spin relaxation times  $T_1$  and  $T_2$ .

$$T_1 = 119(13) \text{ s} \quad (5.1)$$

$$T_2 = 19.5(2.7) \text{ s} \quad (5.2)$$

where  $T_1$  is the combined result for the counting periods  $t_1$  and  $t_2$ . It should be noted that the data for  $T_2$  is extracted from the maximum polarization measured for each free precession setting for the Ramsey fringe data. Essentially, the  $T_2$  measurement cycle is the same as a Ramsey cycle, but the frequency must be on resonance. It is easier to sweep through a large set of frequencies to measure the Ramsey fringe, then extract the  $T_2$  as performed here.

The results for  $T_1$  and  $T_2$  were lower than expectations based on simulations using the magnetic field profile model. One large factor in this was the presence of a stainless steel bellows in the cell valve assembly, which produced local field gradients in the center of the storage chamber  $> 25 \mu\text{G cm}^{-1}$  as measured 1-2 cm above the cell bottom, independent of applied magnetic fields. The offset between the center of the  $B_0$  coil and the center of the shield also reduced the designed field uniformity by a factor of  $10\times$ . The coil was designed, for the setting  $B_0 = 22.2 \text{ mG}$ , to have a volume average gradient magnitude of  $\leq 1.2 \mu\text{G cm}^{-1}$  for the centered case, which increased to  $\leq 15 \mu\text{G cm}^{-1}$  for the vertically offset and shimmed case. The magnitude of

external background magnetic fields inside of the shield was  $\sim 1\%$  of the  $B_0$  setting; though it should be noted that measurements indicate the background was dominated by perturbations due to the bellows.

An additional consideration for the discrepancy between simulated and measured  $T_2$  is the UCN spectrum used. Simulation used a velocity distribution  $P(v) \propto v^2$ , with  $v_{\max} = 7$  m/s. Measurements have indicated that the average velocity magnitude was  $\sim 5.7$  m/s [49], substantially lower than the distribution used in simulation. As shown in section 3.4, the theoretical models and simulation both predict a sharp decrease in  $T_2$  at lower energies.

The Rabi and Ramsey fringes were measured and are shown in figures 5.6, 5.7, 5.8, and 5.9. For each of these, the red data corresponds to counting time  $t_1$  and blue to  $t_2$ . For the Rabi measurement, the  $B_1$  field was turned on for  $\tau = 1$  s to apply a  $\pi$  spin flip; for the Ramsey method, this was separated into two  $\pi/2$  spin-flips for 0.5 s each.

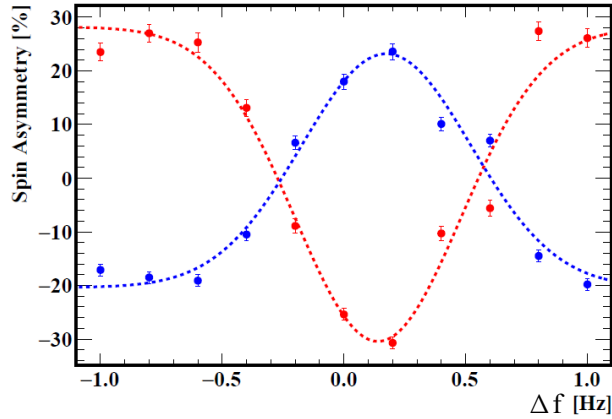


Figure 5.6: Measurement of the Rabi resonance envelope.

Using the central fringe full width at half maximum determined in section 2.1,  $\delta\nu \approx \frac{1}{2T+8t/\pi}$ , the expected full width for  $T = 1$  s, 10 s, and 20 s are: 0.306 Hz, 0.047 Hz, and 0.024 Hz. These agree well with the measurements, though it should be noted that the  $T = 10$  s and 20 s fringes are likely not the central, on resonance fringes. There appears to be a linear trend for the  $T = 10$  s and 20 s fringes, which is expected if there was a systematic shift in the leading order  $\nu_0$  determined by magnetometry. This is very likely due to the use of two magnetometer samples rather than a co-magnetometer which gives an estimate for the entire volume. The resonance frequencies were all  $\sim 65$  Hz, so that the width of the fringes for which

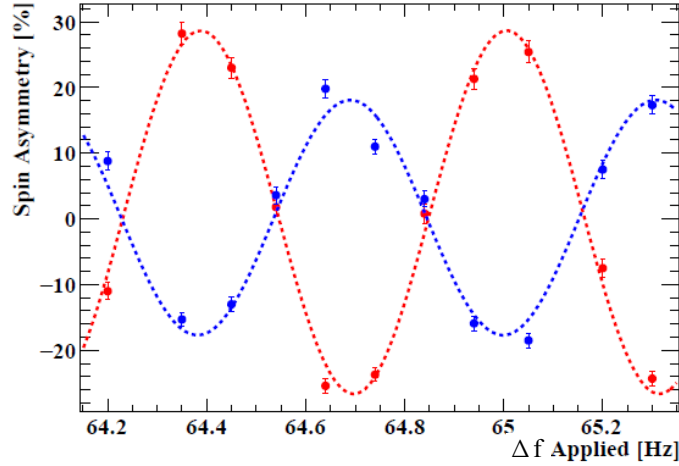


Figure 5.7: Central Ramsey fringe for  $T = 1$  s,  $\tau = 0.5$  s.

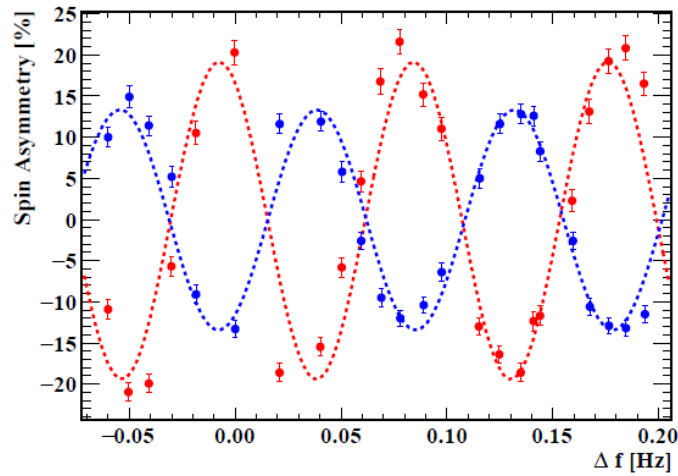


Figure 5.8: Ramsey fringe for  $T = 10$  s,  $\tau = 0.5$  s.

data was collected are  $\frac{\Delta\nu}{\nu_0} < 1\%$ . For the method of magnetometry used, it is not surprising to measure several fringes from the central.

This met the original goal to measure the Ramsey fringe with a prototype apparatus. More importantly is the technical expertise acquired. The most critical lessons pertinent to the magnetic field design involve the requirement to center the  $B_0$  coil relative to the shield in order to reduce the gradients which require shimming, and the need to incorporate the spin transport into the coil designs.

Copyright© James Ryan Dadisman, 2018.

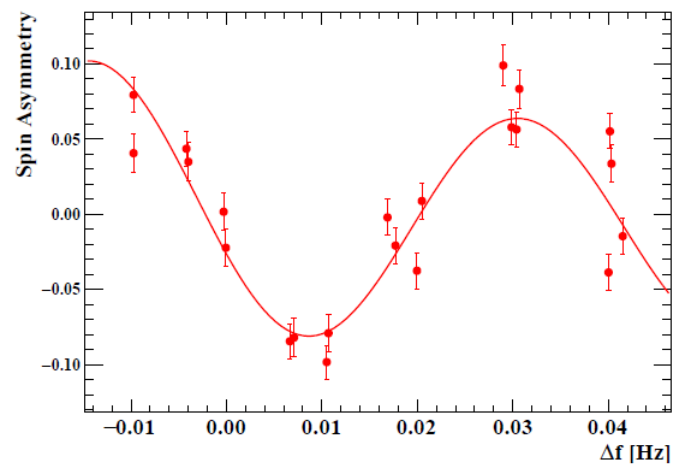


Figure 5.9: Ramsey fringe for  $T = 20$  s,  $\tau = 0.5$  s.



## Chapter 6 Time-Reversal Violation in B-Mesons

As discussed in the opening chapter, discrete symmetries have a central role in fundamental physics and is a strong motivator for many experimental searches. Time reversal is the most difficult to realize experimentally, thus the BaBar collaboration should be recognized for their achievement. I contributed to a phenomenology paper [50] which studied the interpretation of the BaBar result and proposed an analysis method which no longer tests for a  $T$ -asymmetry, but may be used to elucidate small SM or new physics effects using the novel CP and T-tagging methods which BaBar developed.

### 6.1 BaBar Experiment

The BaBar Collaboration was the first to definitively measure a time-asymmetry, with T-violating parameters  $\Delta S_T^+ = -1.37 \pm 0.14_{\text{stat}} \pm 0.06_{\text{syst}}$  and  $\Delta S_T^- = 1.17 \pm 0.18_{\text{stat}} \pm 0.11_{\text{syst}}$  [8]. CPLEAR was a previous experiment which purported to measure TV, but was criticized for the lack of detailed balance in  $K_0 - \bar{K}_0$ , a low statistics result of  $\{A_T^{\text{exp}}\} = (6.6 \pm 1.3_{\text{stat}} \pm 1.0_{\text{syst}}) \times 10^{-3}$  [51], and whether it was in fact a true test of TV. There were three key elements which enabled the successful result by BaBar: Einstein-Podolsky-Rosen (EPR) entanglement [52]; CP / flavor tagging; and neutral meson oscillations.

The B-factories produced EPR entangled  $B\bar{B}$  via  $e^-e^+$  collisions at the  $\Upsilon(4S)$  resonance [53], with center of mass energy 10975 MeV. The entanglement of the initial state holds as the particles propagate in time.

$$|\Psi_i\rangle = \frac{1}{\sqrt{2}} \left( |B^0(\vec{k}), \bar{B}^0(-\vec{k})\rangle - |\bar{B}^0(-\vec{k}), B^0(\vec{k})\rangle \right) \quad (6.1)$$

The branching ratio to  $B\bar{B}$  is  $> 96\%$ , which breaks down to  $B_+B_-$  CP eigenstates (51.4 %) and  $B^0\bar{B}^0$  flavor eigenstates (48.6 %) [54]. The quark content of the flavor eigenstates  $B^0(\bar{B}^0)$  are  $d\bar{b}$  ( $\bar{d}b$ ). The below description of CP eigenstates uses the formalism of the seminal paper by Bañuls and Bernabéu [55] which set the foundation for the BaBar experiment.

$$|B_{\pm}\rangle = \frac{1}{\sqrt{2}}(I \pm CP)|B^0\rangle = \frac{1}{\sqrt{2}}(|B^0\rangle \pm CP_{12}^*|\bar{B}^0\rangle) \quad (6.2)$$

where  $CP_{12}^*$  is a phase from the charge conjugation operator. It is evident that a neutral B-meson may exist and decay from flavor or CP eigenstates, with unique decay products which allow for identification of the eigenstate from which the particle decayed. Combining this with the EPR entanglement of the system allows for a “tagging” of the surviving meson after the first decays.

The neutral B-meson, and similarly the neutral kaon, can oscillate between particle and anti-particle via the weak interaction box diagram.

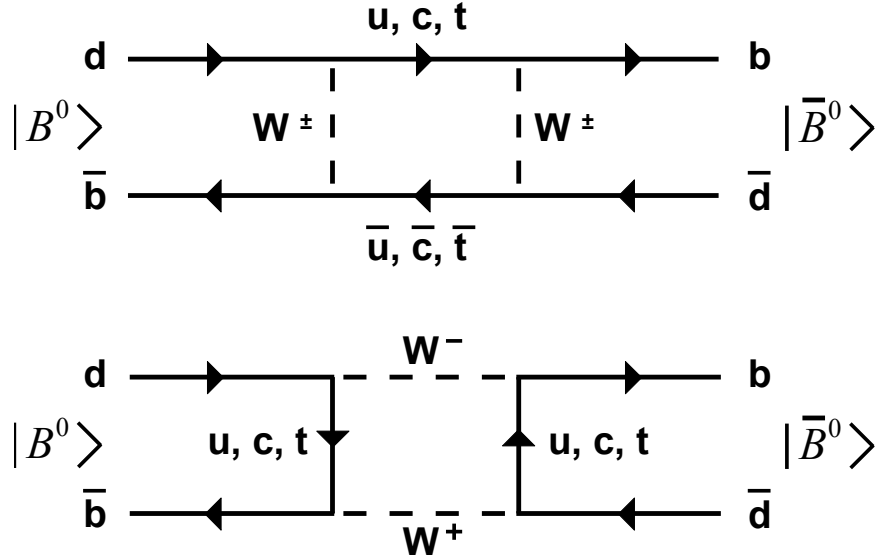


Figure 6.1: Lowest order “box” Feynman diagrams for  $B\bar{B}$  mixing. By exchange of two charged  $W^\pm$  bosons, the final state is the initial state under charge-conjugation:  $d\bar{b} \rightarrow b\bar{d}$ . The diagrams are identical for the opposite oscillation.

This process is one source of CP violation, commonly referred to as “CPV from mixing”. The weak interaction is also responsible for the decay of the neutral B-meson.

The specific decay of  $\bar{b} \rightarrow c\bar{c}\bar{s}$  and its CP conjugate are of central importance to the BaBar experiment, and will equivalently be referred to as  $B_0 \rightarrow J/\psi K^0$ . It is important to note that the B-meson may also decay from a CP eigenstate  $B_\pm$ , in which case it will decay to a CP eigenstate of the kaon  $K_\pm$ , or commonly referred to as  $K_{S,L}$ . Here the ‘S’ and ‘L’ subscripts refer to the ‘short’ and ‘long’ lifetime of the CP eigenstates, which differ by a factor of 555, so that  $\tau_L \approx 555\tau_S$  [54].

Consider a single  $B\bar{B}$  entangled pair. At some initial time  $t_0$ , one of these will decay. The products can be analyzed to determine exactly which flavor or CP eigenstate from which this particle decayed. Due to entanglement, this means the state of the surviving B-meson can be “tagged” at the time  $t_0$ . This is the power of this

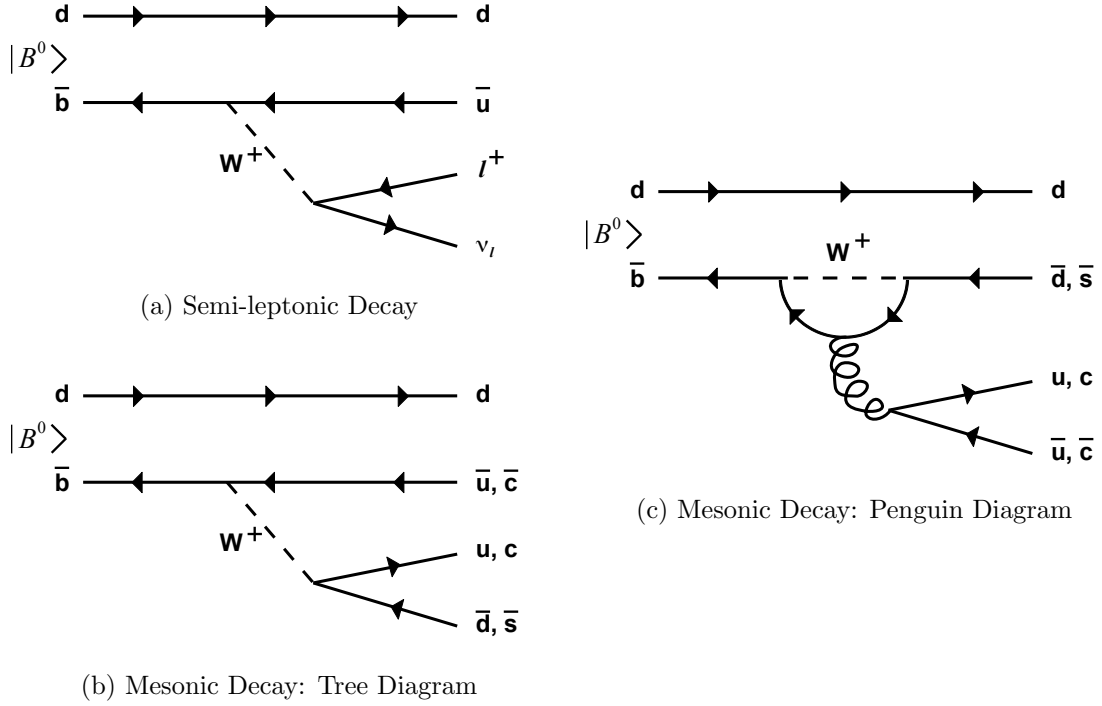


Figure 6.2: Leading order decay modes for the neutral B-meson. Of special interest to CKM unitarity angle  $\beta$  is the decay of  $b \rightarrow c\bar{c}\bar{s}$ .

experimental method: the initial state of a B-meson can be known due to EPR entanglement, and the meson mixes such that it can decay from a different flavor or CP eigenstate. There are 4 unique initial states and final states which can be used to measure CP, T, and CPT asymmetries. An example is given in table ??.

Table 6.1: Sample of initial and final state CP, T, and CPT asymmetries.

Control	CP	T	CPT
$B^0 \rightarrow B_+$	$\bar{B}^0 \rightarrow B_+$	$B_+ \rightarrow B^0$	$B_+ \rightarrow \bar{B}^0$

The time-dependent decay probabilities were worked out by Bañuls and Bernabéu [55]; for simplicity, I shall use a formalism first used by Applebaum et al. [56]

$$\Gamma_{(f_1)_\perp, f_2} = \mathcal{N}_1 \mathcal{N}_2 e^{-\Gamma(t_1+t_2)} [1 + C_{(1)_\perp, 2} \cos(\Delta m_B t) + S_{(1)_\perp, 2} \sin(\Delta m_B t)], \quad (6.3)$$

with the conditions from [50]:  $\Gamma \equiv (\Gamma_H + \Gamma_L)/2$ ,  $\Delta m_B \equiv m_H - m_L$ ,  $t = t_2 - t_1 \geq 0$ ,  $S_{(1)_\perp, 2} \equiv C_1 S_2 - C_2 S_1$ , and  $C_{(1)_\perp, 2} \equiv -[C_2 C_1 + S_2 S_1]$  [56]. Moreover,  $C_f \equiv (1 - |\lambda_f|^2)/(1 + |\lambda_f|^2)$  and  $S_f \equiv 2\Im(\lambda_f)/(1 + |\lambda_f|^2)$ , where  $\lambda_f \equiv (q/p)(\bar{A}_f/A_f)$ , noting

$A_f \equiv A(B^0 \rightarrow f)$ ,  $\bar{A}_f \equiv A(\bar{B}^0 \rightarrow f)$ ,  $\mathcal{N}_f \equiv A_f^2 + \bar{A}_f^2$ , and  $q$  and  $p$  are the usual  $B\bar{B}$  mixing parameters such that  $(q/p) \approx \frac{V_{td}V_{tb}^*}{V_{td}^*V_{tb}}$  [57]. Note that  $f_1, f_2$  refer to the initial and final decay products respectively. An additional simplification follows by neglecting wrong-sign semileptonic decays:  $C_{\ell+X} = -C_{\ell-X} = 1$ . For the CP and T cases of importance to the BaBar experiment, e.g., table ??, the asymmetries become:

$$A_{CP} = A_T = -|S_f| \cos(\Delta m_B t) \quad (6.4)$$

$$S_f \equiv 2\Im(\lambda_f)/(1 + |\lambda_f|^2) \quad (6.5)$$

$$\lambda_f \equiv (q/p)(\bar{A}_f/A_f) \quad (6.6)$$

One note on notation: BaBar actually performs a likelihood fit, in which the coefficient is  $\frac{\Delta S_f}{2}$ . For the ‘‘golden mode’’ decays  $B \rightarrow J/\Psi K_{S,L}$ ,  $\lambda_{J/\Psi K_S} = -\lambda_{J/\Psi K_L}$  and the coefficient reduces to equation 6.4. The result from BaBar found this TV term to be non-zero at  $14\sigma$  confidence [8].

## 6.2 Sensitivity to BSM Effects

Any beyond standard model (BSM) physics would appear as a relatively small effect. However, the non-dominant SM effects must first be well understood before any claims regarding BSM can be considered valid. One important test is the ‘‘universality’’ of the CKM unitarity angle  $\beta \equiv \arg\left[-\frac{V_{cd}V_{cb}^*}{V_{td}V_{tb}^*}\right]$ , where the  $V$ 's are elements of the CKM matrix. Looking more closely at the composition of  $\lambda_f$  reveals how  $\beta$  becomes an observable. The mixing term  $(q/p) \approx \frac{V_{td}V_{tb}^*}{V_{td}^*V_{tb}}$  to leading order. The tree diagrams in figure 6.2b dominate the decay amplitudes, such that  $\frac{\bar{A}_{J/\Psi K_S}}{A_{J/\Psi K_S}} \approx \eta_{CP} \frac{V_{cb}V_{cd}^*}{V_{cd}V_{cb}^*}$  [53], where  $\text{CP}|f\rangle = \eta_{CP}^f|f\rangle$ . The result:  $\lambda \approx \eta_{CP} e^{-2i\beta}$ . Inserting this into  $S_f$  and considering the sign difference in  $\eta_{K_S} = -\eta_{K_L} = -1$ , then  $|S_{J/\Psi K_{S,L}}| = \sin(2\beta)$ . Likewise,  $|\lambda_f|^2 = 1$  and  $C_f = 0$ .

The results discussed thus far ignore the contributions of higher order terms, namely the penguin decay diagrams shown in figure 6.2c, which are small and difficult to separate from the leading order processes. It was proposed by Dadisman et al. [50] that the smaller SM contributions might be better understood by constructing asymmetries in which the leading order tree diagrams cancel out.

## Interpretation of T-Asymmetry

A discussion of the interpretation of  $A_T$  measured by BaBar is required for this concept. Figure 6.3 a) shows the ideal picture of  $A_T$ , in which an exact time-reversed

process is measured uniquely. Using the formalism of Applebaum et al. [56], the tagging process at the initial time of the remaining meson can be thought of as an inverse decay from the opposite CP or flavor tag. The picture is muddled by the fact that the decay products are not directly detected. The CP tag of the B-meson is determined by its decay to the  $K_S$  or  $K_L$  CP eigenstates of the kaon, which is in turn detected by the kaon decay products. CP-violation in the kaon mixing and decay can break the picture of a perfect time-reversal process, as shown in figure 6.3. For a complete discussion of the conditions for  $A_T$  to be interpreted as a true test of T, see [50, 56].

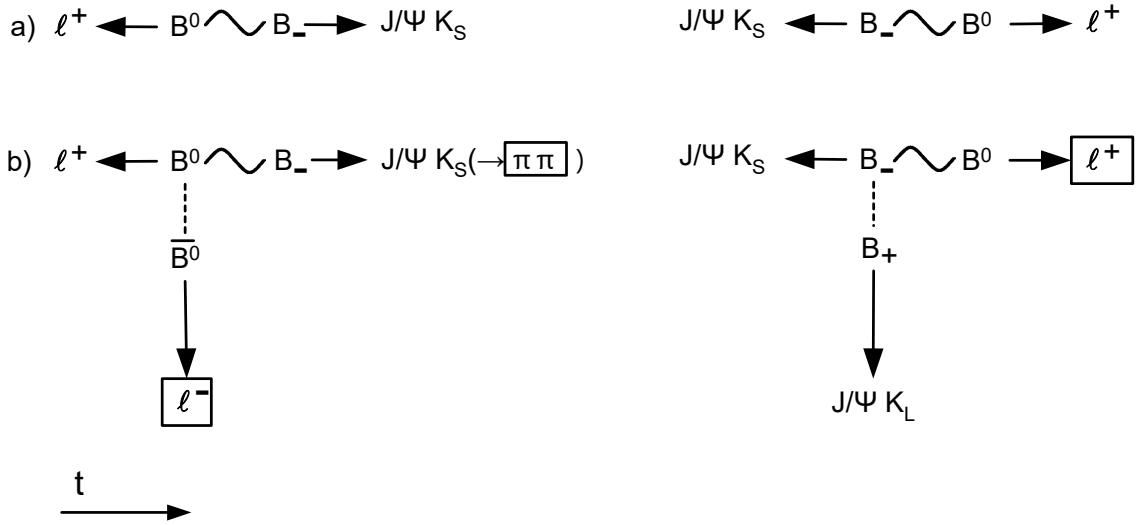


Figure 6.3: The transition  $B^0 \rightarrow B_-$  and the construction of its time-conjugate  $B_- \rightarrow B^0$ . a) Idealized: the initial detection of  $l^-$  projects the surviving  $B$  into the orthogonal flavor state, realizing  $B^0 \rightarrow B_-$  upon subsequent detection of  $J/\psi K_S$ , whereas the initial detection of  $J/\psi K_L$  projects the surviving  $B$  into the CP = - state. In this latter case subsequent detection of  $l^+ X$  realizes  $B_- \rightarrow B^0$ , the time-reversed process associated with  $B^0 \rightarrow B_-$ . The initial-state projections can be thought of as inverse decays of  $l^+$  and  $J/\psi K_S$ , respectively [56]. b) Expanded to include the particles that are detected (boxes) to tag the initial and final states of the  $B$ -meson. The second process is not the time conjugate of the first once direct CP violation in the tagging decay is included. The CP state of the  $B$ -meson prepared through inverse decay is not identical to that of the  $B$  which decays to  $J/\psi K_S(\pi^+\pi^-)$ .

From here, “ $T$ ”-asymmetries can be constructed using  $B\bar{B}$  looking for specific combinations of CP tags which are indisputably no longer a true test of  $T$ . However, these pseudo-asymmetries could be useful by selecting such pairs that will produce a cancellation of the tree-level decay contributions.

## “Trapping Penguins” by Construction of Pseudo-‘T’ Asymmetries

Looking at general decay products of CP eigenstates  $f \neq J/\Psi K_{S,L}$  such that  $\lambda_o \neq \pm\lambda_e$ , with “ $e(o)$ ” corresponding to CP even (odd) states, the general form of these pseudo-asymmetries change:

$$\begin{aligned} A_{CP}^{e+} &\equiv \frac{\Gamma'_{(\ell^-X)_\perp, f_e} - \Gamma'_{(\ell^+X)_\perp, f_e}}{\Gamma'_{(\ell^-X)_\perp, f_e} + \Gamma'_{(\ell^+X)_\perp, f_e}} \\ &= C_e \cos(\Delta m_B t) - S_e \sin(\Delta m_B t), \end{aligned} \quad (6.7)$$

$$\begin{aligned} A_{CP}^{e-} &\equiv \frac{\Gamma'_{(f_e)_\perp, \ell^-X} - \Gamma'_{(f_e)_\perp, \ell^+X}}{\Gamma'_{(f_e)_\perp, \ell^-X} + \Gamma'_{(f_e)_\perp, \ell^+X}} \\ &= C_e \cos(\Delta m_B t) + S_e \sin(\Delta m_B t), \end{aligned} \quad (6.8)$$

where  $A_{CP}^{e+} \rightarrow A_{CP}^{o+}$  and  $A_{CP}^{e-} \rightarrow A_{CP}^{o-}$  follow by replacing  $f_e \rightarrow f_o$ , and the time ordering of the tags is now explicitly stated via the notation  $+(-)$ . Moreover,

$$\begin{aligned} A_T^{o+} &\equiv \frac{\Gamma'_{(f_o)_\perp, \ell^-X} - \Gamma'_{(\ell^+X)_\perp, f_e}}{\Gamma'_{(f_o)_\perp, \ell^-X} + \Gamma'_{(\ell^+X)_\perp, f_e}} \\ &= \frac{(C_e + C_o) \cos(\Delta m_B t) + (S_o - S_e) \sin(\Delta m_B t)}{2 + (C_o - C_e) \cos(\Delta m_B t) + (S_o + S_e) \sin(\Delta m_B t)}, \end{aligned} \quad (6.9)$$

$$\begin{aligned} A_T^{o-} &\equiv \frac{\Gamma'_{(\ell^-X)_\perp, f_o} - \Gamma'_{(f_e)_\perp, \ell^+X}}{\Gamma'_{(\ell^-X)_\perp, f_o} + \Gamma'_{(f_e)_\perp, \ell^+X}} \\ &= \frac{(C_e + C_o) \cos(\Delta m_B t) - (S_o - S_e) \sin(\Delta m_B t)}{2 + (C_o - C_e) \cos(\Delta m_B t) - (S_o + S_e) \sin(\Delta m_B t)} \end{aligned} \quad (6.10)$$

$$\begin{aligned} A_T^{e+} &\equiv \frac{\Gamma'_{(f_e)_\perp, \ell^-X} - \Gamma'_{(\ell^+X)_\perp, f_o}}{\Gamma'_{(f_e)_\perp, \ell^-X} + \Gamma'_{(\ell^+X)_\perp, f_o}} \\ &= \frac{(C_e + C_o) \cos(\Delta m_B t) - (S_o - S_e) \sin(\Delta m_B t)}{2 - (C_o - C_e) \cos(\Delta m_B t) + (S_o + S_e) \sin(\Delta m_B t)} \end{aligned} \quad (6.11)$$

$$\begin{aligned} A_T^{e-} &\equiv \frac{\Gamma'_{(\ell^-X)_\perp, f_e} - \Gamma'_{(f_o)_\perp, \ell^+X}}{\Gamma'_{(\ell^-X)_\perp, f_e} + \Gamma'_{(f_o)_\perp, \ell^+X}} \\ &= \frac{(C_e + C_o) \cos(\Delta m_B t) + (S_o - S_e) \sin(\Delta m_B t)}{2 - (C_o - C_e) \cos(\Delta m_B t) - (S_o + S_e) \sin(\Delta m_B t)}, \end{aligned} \quad (6.12)$$

Each time-dependent asymmetry has four parameters made distinguishable by the various time-dependent functions, and they can be measured experimentally. Indeed

the individual asymmetries can be simultaneously fit for  $S_o + S_e$ ,  $S_o - S_e$ ,  $C_o + C_e$ , and  $C_o - C_e$ . Note that if  $C_o = C_e$  and  $S_o = -S_e$ ,  $A_{CP}^{e+} = A_{CP}^{o-} = A_T^{o+} = A_T^{e-}$  and  $A_{CP}^{e-} = A_{CP}^{o+} = A_T^{o-} = A_T^{e+}$ , as before. Recall that to leading order,  $S_f \approx -\eta_{CP}^f \sin 2\beta$  and  $C_f \approx 0$ . The leading order contributions cancel from the parameter  $S_o + S_e$ , such that small effects, e.g., from penguin contributions, and any BSM effects would be directly determined. To determine whether BSM effects are present, it is necessary to correlate the observable deviations in  $S_f$  from  $\sin 2\beta$  due to the penguin contributions.

Revisiting the previous calculation of  $\lambda$ , let us consider amplitudes from the tree and penguin diagrams while retaining the approximate form of the mixing term ( $q/p$ ). By CKM unitarity, a single decay amplitude can be written in terms of two weak mixing angles, for this example the ‘‘charm’’ angle  $\theta_c = 0$  and ‘‘up’’ angle  $\theta_u = \gamma$ . If we combine the topological amplitudes for each weak phase up to penguin diagrams into terms  $a_f^c$  and  $a_f^u$ , in which the  $f$  refers to the final decay state and  $c, u$  indicate the corresponding weak mixing angle, then the total amplitude may be written  $A_f = a_f^c e^{-i\theta_c} + a_f^u e^{-i\theta_u} = a_f^c + a_f^u e^{-i\gamma}$ . Now  $\lambda$  may be rewritten:

$$\lambda_f = -\eta_{CP}^f e^{-2i\beta} \frac{1 + d_f e^{-i\gamma}}{1 + d_f e^{i\gamma}}, \quad (6.13)$$

$$d_f \equiv \left| \frac{V_{ub}^* V_{us}}{V_{cb}^* V_{cs}} \right| \frac{a_f^u}{a_f^c}, \quad (6.14)$$

Completing the calculation for the time-dependent asymmetry parameters yields:

$$\begin{aligned} S_f &= -\eta_{CP}^f \frac{\sin(2\beta) + 2\Re(d_f) \sin(2\beta + \gamma) + |d_f|^2 \sin(2\beta + 2\gamma)}{1 + |d_f|^2 + 2\Re(d_f) \cos(\gamma)}, \\ C_f &= \frac{-2\Im(d_f) \sin(\gamma)}{1 + |d_f|^2 + 2\Re(d_f) \cos(\gamma)}. \end{aligned} \quad (6.15)$$

Noting that the dominant phase contribution comes from  $a_f^c$  such that  $d_f \approx 0$  restores the results for  $S_f = -\eta_{CP}^f \sin(2\beta)$ ,  $C_f = 0$  previously given to leading order. These expressions reveal the fundamental difficulty in separating the tree diagrams from the penguin contributions, therefore a common simplification is used in theoretical studies [58–60]:  $S_f = -\eta_{CP}^f (\sin(2\beta) + \Delta S_f)$ . Because  $d_f$  is small, the denominator can be expanded to account for the  $\sin 2\beta$  cancellation, but there remains the added complication of terms mixed with  $d_e$  and  $d_o$  such that it is more accurate to state that  $S_o + S_e = \delta_{S_e} - \delta_{S_o}$ .

It is worrisome to extract a result from the difference of two small numbers. However, the decay  $b \rightarrow c\bar{c}s$  is considered the ‘‘golden mode’’, because penguin contributions are expected to be  $\leq 1\%$  [53]. Other decay modes have calculated and

measured penguin contributions  $\mathcal{O}(10\%)$  [53, 58], but with very large uncertainties comparable to the contribution's magnitude. Using the “golden mode” as one of the CP tags will result in  $S_o + S_e \approx \eta_{CP}^f \delta_{S_f}$ , where  $f$  corresponds to the non-“golden” decay amplitude. The error introduced by this  $\delta_{S_{b \rightarrow c\bar{c}s}} = 0$  approximation is  $\leq \mathcal{O}(10\%)$ ; a considerable improvement in the determination of the penguin contributions is thus dependent on how well the fit parameters can be determined.



## Chapter 7 Summary of Progress Toward a Neutron EDM Measurement

The overarching theme of this dissertation is the complex relationship between magnetic field profiles and systematic effects in spin-resonance experiments, especially neutron electric dipole moment searches. Even the simplest magnetic field sources produce fields which, if written as an expansion in the spatial coordinates, require a high order in the expansion to properly describe inside a fiducial volume which is on the same order of magnitude as the magnetic field source. These higher order terms in the field may have a larger effect on the systematics dependent on the phase-space. For a perfectly uniform distribution of neutrons inside a cylindrical chamber, the number of neutrons at a given radius is a function of the radius, i.e., there are more neutrons at the edges of the fiducial region than at the center. It is likely that the neutrons are not uniformly distributed; unfortunately, the density as a function of position is highly dependent on the type of wall collisions, which is difficult to characterize for the storage chamber. Additionally, the geometry of the chamber and the location where the UCN guide connects to it will affect the phase-space of the neutrons.

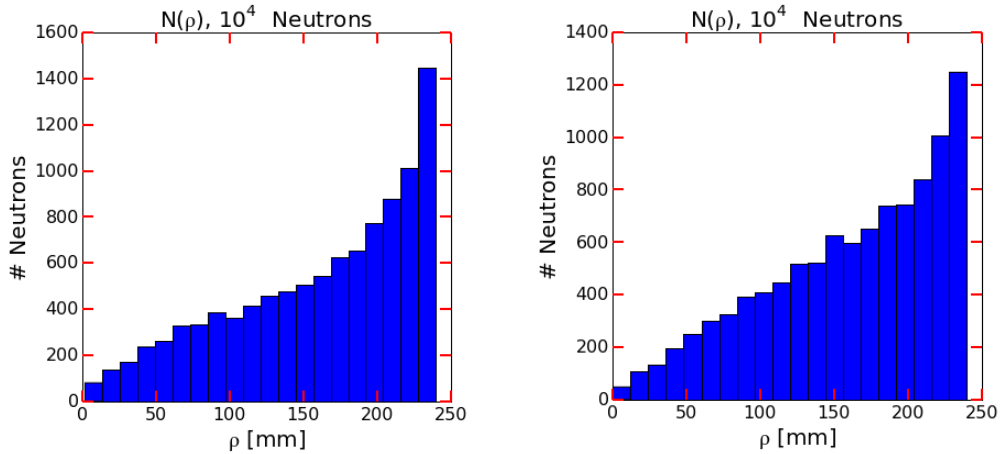


Figure 7.1: Histograms showing the simulated neutron distribution as a function of radius for roughness parameters  $b = 2\text{nm}$ ,  $w = 10\text{nm}$  (left), and  $b = 25\text{nm}$ ,  $w = 125\text{nm}$  (right).

As shown in figure 7.1, using the Steyerl model with larger roughness parameters, corresponding to a higher percentage of non-specular reflections, results in the neutron distribution being approximately a linear function of the radius. This result is

expected for a uniform neutron density. For more specular reflections, there seems to be a more exponential increase in density at increasing radius. At this level of comparison, these differences are subtle; however, combined with the different trajectories, this can have an appreciable effect in simulated results. Simulations in section 3.4 demonstrated that the transverse spin relaxation time,  $T_2$ , is highly dependent on the percentage of specular reflections; in fact, it seems having rougher walls to introduce more non-specular reflections can increase  $T_2$ . However, this could result in an increase in additional wall losses [36], so that further studies are warranted.

At the outset of this research, these complexities were not clear to the author. The experimental research starting point was optimization of a gapped solenoid for use in the LANL nEDM prototype apparatus. The strategy selected was to minimize the volume averaged magnitude of the gradient term  $dB_z/dz$ , in order to reduce the false EDM effect. It became clear that adding more gaps created more degrees of freedom which could be optimized: gap lengths between, and the current within, each section. The most significant advantage to this is the increase in uniformity along the longitudinal axis of the coils, particularly useful for a double-chamber experiment. This advantage over traditionally used coils cannot be overstated: the strategy typically used to increase magnetic field uniformity is to either make the coil bigger, which can substantially increase the cost of the experiment primarily due to the cost of a larger magnetic shield, or by using special coil geometry at the endcaps to reduce distortion due to end-effects, which is very sensitive to misplacement of the wires. In contrast, multi-gap solenoids can achieve the required uniformity with reduced length, and are less sensitive to wire misplacement because a single wire in a solenoid contributes a smaller percentage to the total field than, say, a discretized  $\cos\theta$  coil. Optimization of the current in each section is a novel technique which has value in any experiment which requires highly uniform magnetic fields, and should be explored as a more easily tuned parameter compared with precise wire spacing.

Construction and study of the multi-gap solenoid concept is the greatest contribution of this dissertation. This type of design has been perhaps overlooked due to its simplicity, which is unfortunate because it is easy to optimize and it is very effective at producing highly uniform magnetic fields. The novel contribution here is the idea to optimize the current in different sections of the coil as a fine-tuning parameter, and to use numerical methods to optimize the total uniformity for a volume of interest rather than selectively reducing certain terms in an expansion. The argument here is that, for a volume, only reducing a lower order term may result in an accidental increase in a higher order term which, for a large volume, may be worse for system-

atic effects. The multi-gap solenoid concept demonstrates the capability to exceed the magnetic field specifications for a neutron electric dipole moment experiment.

A simulation was written to evaluate the expected performance of the resulting magnetic field of the prototype  $B_0$  coil. It was through these studies that the complex relationship between the magnetic field and phase-space became apparent to the author. The initial goal of the simulation was high accuracy; in retrospect, more emphasis should have been placed on a faster simulation so that more of the phase-space was sampled. Due to the complexities, it is advantageous to use such a simulation for the optimization of experiment design parameters, e.g., the geometric design of the storage chamber, guides, and for magnetic field design.

Mapping hardware was built to map in-situ the magnetic field of the prototype, and to study the effectiveness of magnetic field reconstruction methods. Reconstruction methods show promise, at a minimum, to supplement co-magnetometers by providing information on gradients which may be used in improving analysis of systematic effects. Further refinement of the method may be capable of fully replacing co-magnetometers.

## 7.1 Evaluation of the Multi-gap Solenoid Concept

The theoretical models for multi-gap solenoids with gap length and current optimizations demonstrates great promise for use in a neutron EDM experiment. As demonstrated by comparisons with  $\cos\theta$  coils in chapter 4, the prototype DGS which was optimized for a single chamber produces a field for a double-chamber configuration which varies by  $< 0.2\%$  of the value inside the center of the chamber. Notably, this coil was designed to be an order of magnitude less uniform than what could have been accomplished if the coil were the maximum size allowable by the interior dimensions of the shield.

An additional benchmark which is suitable is the  $B_0$  coil being designed for a similar nEDM experiment currently being developed at the Paul Scherrer Institute [61]. The design for this coil is a rectangular solenoid with dimensions  $\sim 2.7\text{ m} \times 2.7\text{ m} \times 2.7\text{ m}$ , and wires spaced 15 mm apart. Special wire-routing for pass-through holes is included, and additional wire “endcaps” are used to increase the uniformity. For a double-chamber configuration, the magnetic field is expected to be within 0.01% of the central field value everywhere within the 40 cm radius chambers. This level of uniformity has been achieved for a cylinder of 25 cm radius and 10 cm in length, the dimensions to be used in the LANL experiment, in a 4-gap solenoid COMSOL model

with 1 m radius and 1.5 m total length, inside of a magnetic shield with dimensions  $2.5 \text{ m} \times 2.5 \text{ m} \times 2 \text{ m}$ . It should be noted that, because constraints on the design are still undetermined, minimal effort has been put into the optimization for the full-size coil.

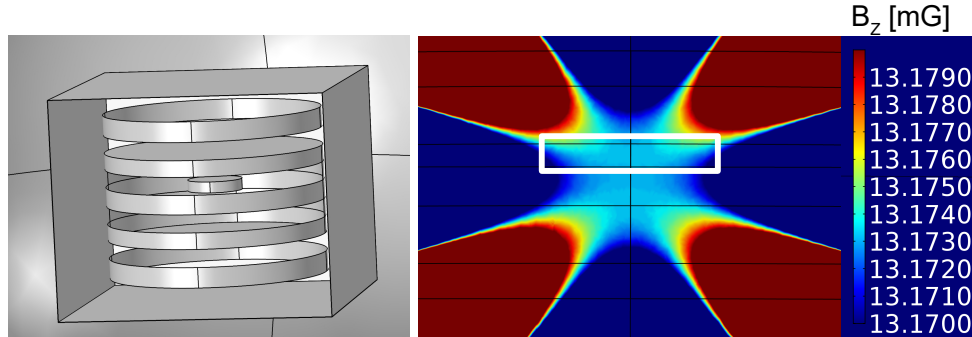


Figure 7.2: A model 4-gap solenoid, lightly optimized for a double-chamber configuration. Model is shown on the left,  $B_z$  is shown on the right. The white box indicates the edges of the fiducial volume. Note the heatmap scale is  $(1 \pm 7.6 \times 10^{-5}) \times 13.175$  [mG].

The model indicates that the uniformity requirements for a neutron EDM experiment can be achieved using a multi-gap solenoid. However, additional studies must be conducted to determine the sensitivity to gradients induced by vertical displacements. As was shown in the prototype coil, vertical offsets on the order of inches will result in an order of magnitude degradation in the uniformity. This has also been noted by the PSI collaboration [61], where strict limits have been set on individual terms in the multipole expansion of the magnetic field. They found that a vertical displacement of the coil relative to the shield of 0.25 mm produces a gradient term  $dB_z/dz$  greater than specification; a vertical displacement of 1 mm causes multiple other multipole expansion terms to be out of specification.

## 7.2 Improvements in Simulation of Neutron Electric Dipole Moment Experiments

Several recommendations can be made for improving the simulations presented in chapter 3. It may be beneficial to use a simplified model of wall reflections, a more general method of detecting wall collisions, and using a Runge-Kutta integrator for the spin. Modeling of the magnetic fields using the method outlined in section 3.3 is

very effective at capturing the complexities of the magnetic field and is computationally efficient, and should be used for future simulations.

The method of Steyerl et al. [36] is one of the more advanced models of UCN wall reflections; however, it is dependent on “roughness” parameters which are not very well understood. If these properties are characterized for samples of the surface materials used in the guides and storage chamber, then this method of modeling reflections is preferable; the reflected angles and the absorption coefficient can both be calculated, and are dependent on the incident angles and momentum. However, if they are not characterized, it would be better to set the percentage of non-specular wall collisions in simulation as a tunable parameter, as this percentage is difficult to control using the roughness parameters. The non-specular reflected angle can then be sampled from a  $\cos\theta$  distribution from normal, as required by detailed balance [36]. This method would be computationally more efficient than the method of Steyerl et al., though some of the phase-space dependence on reflections is lost.

Consideration should also be given to improving the accuracy of the geometry model and a more general method of detecting wall collisions. In the region where the storage cell valve and the cell wall meet, there are chamfers to the geometry to facilitate smooth valve actuation. These may have appreciable effects on the trajectories of the neutrons. Simple cylindrical walls were used in simulation, as it was easier to detect wall collisions by direct comparison of the location of the neutrons relative to the dimensions of the cylinder. By implementing a more general method of wall collision detection in the simulation, more complex geometries can be constructed. This is especially significant for the problem of simulating the spin transport into and out of the chamber, as the valve assembly which connects the UCN guide to the storage chamber is more geometrically complex. Such a simulation would be a great benefit to the LANL experiment.

The emphasis placed on accuracy in selecting the Bulirsch-Stoer algorithm may have been unnecessary. Typically, the integration over a time step  $\Delta t$  would resolve after the second extrapolation step, i.e., the third integration using increasing substeps and the first which produces an error estimate, and this was largely independent of the error per step setting. Even with a field model expansion to  $\mathcal{O}(\ell = 6)$ , the uniformity of the magnetic field was such that the adaptive stepsize controller rarely changed the stepsize, and extrapolation using increasing number of substeps provided little benefit. This indicates that it may be more computationally efficient, with no loss in accuracy, to use a 4th order Runge-Kutta algorithm. The expected increase in efficiency would allow for more phase-space to be sampled. For this particular system,

if the tradeoff between accuracy and efficiency is 1:1, i.e., a factor of ten reduction in accuracy results in a factor of ten improvement in efficiency, then it is preferable to sample  $10^6$  neutrons with error in the expectation value of the  $\langle\sigma_z\rangle$  of 10 ppm than  $10^5$  neutrons with error 1 ppm.

An additional consideration for simulation of a false EDM based on the Ramsey method is the difficulty in setting the leading order resonant frequency estimate. In experiment, a co-magnetometer with atoms distributed very similarly to the UCNs gives the leading order estimate. In simulation, this estimate must be calculated from the field profile. This is highly dependent on the phase-space of the neutrons. Simulations can give a distribution of the positions as in figure 7.1, however, the trajectory information is just as important and is not as easily approximated. This information is embedded in the results given by a co-magnetometer, but is not so simple to determine in simulation.

As a result, Ramsey fringes from simulation have systematic shifts from the leading order estimate resonant frequency. This is problematic when it comes to setting probe frequencies, which as discussed in section 2.1 should be targeted at  $\nu \approx \nu_0 \pm \delta\nu/2$ . If the leading order estimate is offset by nearly  $\delta\nu/2$ , as in figure 7.3, then the simulations will be performed where the Ramsey method is least sensitive to small shifts rather than most sensitive. This can be counteracted by measuring a larger set of frequencies in a range  $\nu \in (\nu_0 - \delta\nu/2, \nu_0 + \delta\nu/2)$  centered about the leading order estimate. The problem with this is the reduction in useful statistics; approximately 60% of the simulation results will likely be at frequencies with minimum sensitivity to small shifts. This is problematic when it takes considerable amount of simulation time to accumulate suitable statistics.

### 7.3 Magnetometry Improvements

It has been proposed to use measurements of components of the magnetic field at optimized boundary locations as a method of reconstructing the field within the fiducial volume during the experiment [42]. Having the capability to accurately reconstruct the vector components of the magnetic field would allow systematic corrections, e.g., due to the false EDM  $\vec{v} \times \vec{E}$  term, to be made for each data run. Co-magnetometers only give an average scalar magnitude of the field inside of the storage chamber. Any systematic corrections based on the gradients must then be made using maps of the field which are taken without the full apparatus in place, and on separate days from the data collection. This introduces greater error in the systematic correction,

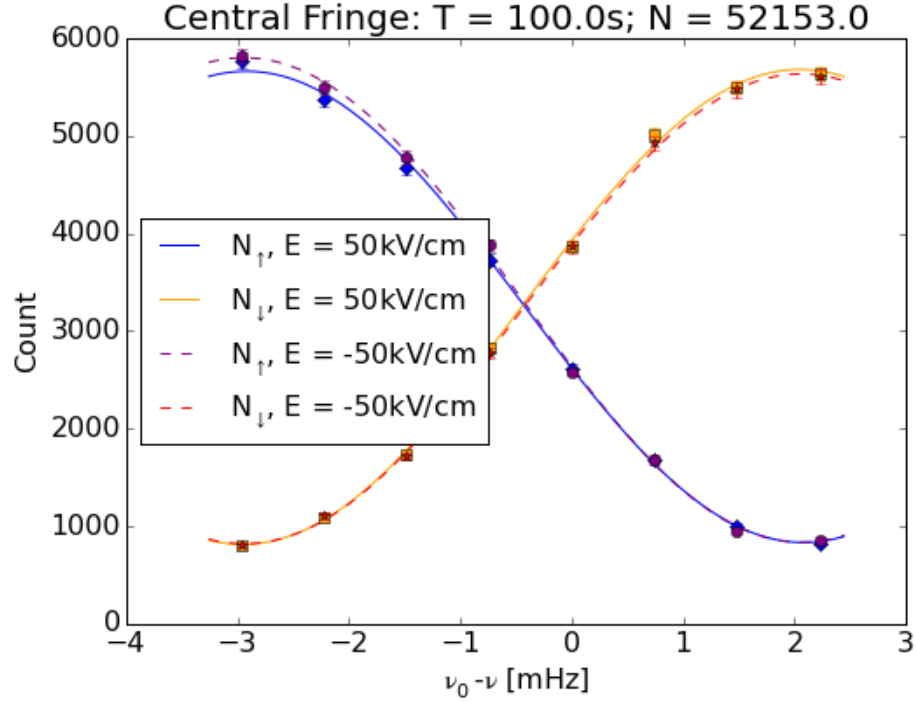


Figure 7.3: A simulated Ramsey measurement to determine the false EDM. Note the leading order estimate is shifted by nearly  $\delta\nu/2$ ; as a result, only  $\sim 25\%$  of the simulated frequencies are useful.

compared to gradient information collected simultaneous with the EDM data.

A prototype apparatus was constructed to do this, as discussed in section 4.4. The hardware demonstrated capability, and in-process refinements to the hardware and reconstruction method should soon make this technique ready for deployment.

The hardware improvements are primarily needed to promote long-term reliability. Stepper motors were used in this first apparatus, and are not ideal for the task. The main reason is that stepper motors do not “know” their position; there is no way to detect slipping or backlash in the motor. The position is tracked in software, which will become incorrect if the stepper motor slips. Servo motors would be a better option, because they have an intrinsic mechanism which determines the motor’s absolute position, and also have improved control over motion. An additional improvement would be in the use of a timing belt for rotating the turn-table. Kevlar string was used in the apparatus because it stretches little under tension. It was discovered that the length of string required between the turntable inside of the shield and the motor outside of the shield allowed enough stretch that an appreciable tension difference developed between the string on each side of the turn-table. This would cause problems syncing the angular rotation of the motor to the rotation of

the turn-table. A timing belt requires a more complex apparatus, but is more reliable than kevlar string. Combined with improvements to the turntable, this should substantially improve the long-term reliability of the mapper.

The reconstruction method was briefly discussed in the magnetic field modeling for simulation in section 3.3. The method is being refined by collaborators, but the closeness of the work with the author’s research warrants some brief comments. One difficulty is the number of boundary values which must be collected in order to reconstruct enough fit parameters: for  $\ell_v = 6$  in the vector components, the scalar potential method, preferred for reconstruction because a single set of coefficients determines all vector components, requires  $\ell_s = 7$ . This would require a minimum of 63 measurements to fit 63 components. Simplifications can be made, e.g., by symmetry, most of the odd terms in the vector, i.e., even in  $\ell_s$ , will be zero. Setting the  $\ell_s = 4, 6$  terms to zero, only 52 measurements are needed. The prototype apparatus can perform this number of measurements for each measurement cycle. However, in the case of cryogenic experiments, as in the proposed SNS nEDM experiment, the probes must be set in stationary locations, at least one probe for each fit parameter.

Another difficulty in the reconstruction method comes from the fitting algorithm. Any optimization algorithm is strongly dependent on the initial estimate for the fit parameters. The  $B_0$  source coil can be characterized beforehand, as in section 3.3, and these parameters can be used as the initial parameters used by the fitting procedure. The reconstruction problem then becomes the simpler case of solving for the perturbations to the ideal magnetic field.

If the boundary value method of magnetometry is to replace co-magnetometers completely, the phase-space of the neutrons must be very well understood. Such information is needed to calculate the weighted average magnitude of the magnetic field, so that an accurate leading-order estimate of the resonant frequency can be calculated from boundary measurements of the magnetic field.

#### **7.4 Final Notes on Magnetic Field Design for the Proposed LANL EDM Experiment**

Future design of neutron EDM experiments should utilize spin simulations to assist in design optimization. It is of particular interest to study the systematics resulting from magnetic field profiles which are optimized using different metrics. The standard formulation of the false EDM effect is typically given assuming a constant gradient  $dB_z/dz$ ; however, a topic of recent conferences is the contributions of higher order



terms in the gradient. Perhaps there is another metric which is superior for minimizing this effect. As was discussed in an analysis of simulations for the transverse spin relaxation time for average gradients of different profiles in section 3.5, consideration of the average magnitude of the gradient may not be the best option.

In deriving the false EDM, it is the contribution to the transverse fields caused by the constant gradient which are of interest. A contributing factor is the cylindrical symmetry of the magnetic field being considered. It may be more suitable to minimize the transverse components of the fields produced by the coil, or equivalently, by  $\vec{\nabla} \cdot \vec{B} = 0$ , minimizing the variance in the longitudinal component, and to design coils which are azimuthally asymmetric. Extensive studies should be conducted in simulations comparing the false EDM for coils optimized using different metrics in order to identify the most effective method. Attempting to minimize the effect by increasing order of an expansion is inefficient, and may in fact cause adversely large higher order terms.

The phase-space of the neutrons must also be studied experimentally. Accurate implementation of this in simulation can help tune the storage chamber dimensions; if it is determined that a disproportionate number of neutrons are located at larger radii, it may be beneficial to reduce the radius of the chamber to reduce systematic effects due to the magnetic fields.

Understanding more about a topic inevitably leads to new questions. The research presented here has contributed to future nEDM experiments, and raises interesting new questions to be studied in order to more thoroughly understand magnetic field related effects in spin-resonance experiments.

## Bibliography

- [1] J. M. Pendlebury et al. *Revised experimental upper limit on the electric dipole moment of the neutron*. Nov. 2015. DOI: 10.1103/PhysRevD.92.092003. URL: <http://link.aps.org/doi/10.1103/PhysRevD.92.092003>.
- [2] J. H. Smith, E. M. Purcell, and N. F. Ramsey. “Experimental Limit to the Electric Dipole Moment of the Neutron”. In: *Phys. Rev.* 108 (1 Oct. 1957), pp. 120–122. DOI: 10.1103/PhysRev.108.120. URL: <https://link.aps.org/doi/10.1103/PhysRev.108.120>.
- [3] C. S. Wu et al. *Experimental Test of Parity Conservation in Beta Decay*. Feb. 1957. DOI: 10.1103/PhysRev.105.1413. URL: <http://link.aps.org/doi/10.1103/PhysRev.105.1413>.
- [4] T. D. Lee and C. N. Yang. *Question of Parity Conservation in Weak Interactions*. Oct. 1956. DOI: 10.1103/PhysRev.104.254. URL: <http://link.aps.org/doi/10.1103/PhysRev.104.254>.
- [5] J. H. Christenson et al. *Evidence for the  $2\pi$  Decay of the  $K_2^0$  Meson*. July 1964. DOI: 10.1103/PhysRevLett.13.138. URL: <http://link.aps.org/doi/10.1103/PhysRevLett.13.138>.
- [6] Michael E. Peskin and Daniel V. Schroeder. *An Introduction to quantum field theory*. Reading, USA: Addison-Wesley, 1995. ISBN: 9780201503975, 0201503972. URL: <http://www.slac.stanford.edu/~mpeskin/QFT.html>.
- [7] R.F. Streater and A.S. Wightman. *PCT, Spin and Statistics, and All that*. Landmarks in Physics. Princeton University Press, 2000. ISBN: 9780691070629. URL: <https://books.google.com/books?id=uFNwSEQ25hEC>.
- [8] J. P. Lees et al. *Observation of Time-Reversal Violation in the  $B^0$  Meson System*. Nov. 2012. DOI: 10.1103/PhysRevLett.109.211801. URL: <http://link.aps.org/doi/10.1103/PhysRevLett.109.211801>.
- [9] A. D. Sakharov. *SPECIAL ISSUE: Violation of CP in variance, C asymmetry, and baryon asymmetry of the universe*. May 1991. DOI: 10.1070/PU1991v034n05ABEH002497.
- [10] Antonio Riotto and Mark Trodden. “RECENT PROGRESS IN BARYOGENESIS”. In: *Annual Review of Nuclear and Particle Science* 49.1 (1999), pp. 35–75. DOI: 10.1146/annurev.nucl.49.1.35. eprint: <https://doi.org/10.1146/annurev.nucl.49.1.35>. URL: <https://doi.org/10.1146/annurev.nucl.49.1.35>.
- [11] Michael Dine and Alexander Kusenko. *Origin of the matter-antimatter asymmetry*. Dec. 2003. DOI: 10.1103/RevModPhys.76.1. URL: <https://link.aps.org/doi/10.1103/RevModPhys.76.1>.

- [12] S. Chatrchyan et al. “Observation of a new boson at a mass of 125 GeV with the CMS experiment at the LHC”. In: *Physics Letters B* 716.1 (2012), pp. 30–61. ISSN: 0370-2693. DOI: <https://doi.org/10.1016/j.physletb.2012.08.021>. URL: <http://www.sciencedirect.com/science/article/pii/S0370269312008581>.
- [13] Michela D’Onofrio, Kari Rummukainen, and Anders Tranberg. “Sphaleron Rate in the Minimal Standard Model”. In: *Phys. Rev. Lett.* 113 (14 Oct. 2014), p. 141602. DOI: 10.1103/PhysRevLett.113.141602. URL: <https://link.aps.org/doi/10.1103/PhysRevLett.113.141602>.
- [14] I.B. Khriplovich and A.R. Zhitnitsky. “What is the value of the neutron electric dipole moment in the Kobayashi-Maskawa model?” In: *Physics Letters B* 109.6 (1982), pp. 490–492. ISSN: 0370-2693. DOI: [https://doi.org/10.1016/0370-2693\(82\)91121-2](https://doi.org/10.1016/0370-2693(82)91121-2). URL: <http://www.sciencedirect.com/science/article/pii/0370269382911212>.
- [15] C. Patrignani et al. “Review of Particle Physics”. In: *Chin. Phys.* C40.10 (2016), p. 100001. DOI: 10.1088/1674-1137/40/10/100001.
- [16] F.-K. Guo et al. “Electric Dipole Moment of the Neutron from 2 + 1 Flavor Lattice QCD”. In: *Phys. Rev. Lett.* 115 (6 Aug. 2015), p. 062001. DOI: 10.1103/PhysRevLett.115.062001. URL: <https://link.aps.org/doi/10.1103/PhysRevLett.115.062001>.
- [17] C. Patrignani et al. *Review of Particle Physics*. 2016. DOI: 10.1088/1674-1137/40/10/100001.
- [18] Evgenii P Shabalin. “Electric dipole moment of the neutron in gauge theory”. In: *Soviet Physics Uspekhi* 26.4 (1983), p. 297. URL: <http://stacks.iop.org/0038-5670/26/i=4/a=R01>.
- [19] Andrzej Czarnecki and Bernd Krause. “Neutron Electric Dipole Moment in the Standard Model: Complete Three-Loop Calculation of the Valence Quark Contributions”. In: *Phys. Rev. Lett.* 78 (23 June 1997), pp. 4339–4342. DOI: 10.1103/PhysRevLett.78.4339. URL: <https://link.aps.org/doi/10.1103/PhysRevLett.78.4339>.
- [20] R. Golub and Steve K. Lamoreaux. *Neutron electric-dipole moment, ultracold neutrons and polarized  $^3\text{He}$* . 1994. DOI: [http://dx.doi.org/10.1016/0370-1573\(94\)90084-1](http://dx.doi.org/10.1016/0370-1573(94)90084-1). URL: <http://www.sciencedirect.com/science/article/pii/0370157394900841>.
- [21] Norman F. Ramsey. *A Molecular Beam Resonance Method with Separated Oscillating Fields*. June 1950. DOI: 10.1103/PhysRev.78.695. URL: <https://link.aps.org/doi/10.1103/PhysRev.78.695>.
- [22] Stephan Paul. “The Neutron and the Universe - History of a Relationship”. In: *PoS BORMIO2012* (2012), p. 025. arXiv: 1205.2451 [hep-ex].
- [23] D.J.R. May. *A High Precision Comparison of the Gyromagnetic Ratios of the  $^199\text{Hg}$  Atom and the Neutron*. Thesis.

- [24] R. W. Pattie Jr. et al. “Measurement of the neutron lifetime using an asymmetric magneto- gravitational trap and in situ detection”. In: (2017). arXiv: 1707.01817 [nucl-ex].
- [25] R. W. Pattie et al. “Evaluation of commercial nickel–phosphorus coating for ultracold neutron guides using a pinhole bottling method”. In: *Nucl. Instrum. Meth. A* 872 (2017), pp. 64–73. DOI: 10.1016/j.nima.2017.07.051. arXiv: 1703.00508 [physics.ins-det].
- [26] S.K. Lamoreaux R. Golub D. Richardson. *Ultra-Cold Neutrons*. CRC Press, 1991. ISBN: 9781351406390. URL: <https://books.google.com/books?id=OyAuDwAAQBAJ>.
- [27] T. M. Ito et al. *Performance of the upgraded ultracold neutron source at Los Alamos National Laboratory and its implication for a possible neutron electric dipole moment experiment*. 2017. arXiv: 1710.05182 [physics.ins-det].
- [28] G. J. Russell, E. J. Pitcher, and L. L. Daemen. “Introduction to spallation physics and spallation-target design”. In: *AIP Conference Proceedings* 346.1 (1995), pp. 93–104. DOI: 10.1063/1.49085. eprint: <http://aip.scitation.org/doi/pdf/10.1063/1.49085>. URL: <http://aip.scitation.org/doi/abs/10.1063/1.49085>.
- [29] C. L. Morris et al. “Measurements of Ultracold-Neutron Lifetimes in Solid Deuterium”. In: *Phys. Rev. Lett.* 89 (27 Dec. 2002), p. 272501. DOI: 10.1103/PhysRevLett.89.272501. URL: <https://link.aps.org/doi/10.1103/PhysRevLett.89.272501>.
- [30] G. Pignol et al. “Frequency shifts and relaxation rates for spin-1/2 particles moving in electromagnetic fields”. In: *Phys. Rev. A* 92 (5 Nov. 2015), p. 053407. DOI: 10.1103/PhysRevA.92.053407. URL: <https://link.aps.org/doi/10.1103/PhysRevA.92.053407>.
- [31] Douglas D. McGregor. *Transverse relaxation of spin-polarized  $^3\text{He}$  gas due to a magnetic field gradient*. Mar. 1990. DOI: 10.1103/PhysRevA.41.2631. URL: <https://link.aps.org/doi/10.1103/PhysRevA.41.2631>.
- [32] G. D. Cates, S. R. Schaefer, and W. Happer. *Relaxation of spins due to field inhomogeneities in gaseous samples at low magnetic fields and low pressures*. Apr. 1988. DOI: 10.1103/PhysRevA.37.2877. URL: <https://link.aps.org/doi/10.1103/PhysRevA.37.2877>.
- [33] Norman F. Ramsey. “Resonance Transitions Induced by Perturbations at Two or More Different Frequencies”. In: *Phys. Rev.* 100 (4 Nov. 1955), pp. 1191–1194. DOI: 10.1103/PhysRev.100.1191. URL: <https://link.aps.org/doi/10.1103/PhysRev.100.1191>.
- [34] J. M. Pendlebury et al. “Geometric-phase-induced false electric dipole moment signals for particles in traps”. In: *Phys. Rev. A* 70 (3 Sept. 2004), p. 032102. DOI: 10.1103/PhysRevA.70.032102. URL: <https://link.aps.org/doi/10.1103/PhysRevA.70.032102>.

- [35] Peter J. Mohr, David B. Newell, and Barry N. Taylor. *CODATA recommended values of the fundamental physical constants: 2014*. Sept. 2016. DOI: 10.1103/RevModPhys.88.035009. URL: <http://link.aps.org/doi/10.1103/RevModPhys.88.035009>.
- [36] A. Steyerl et al. *Surface roughness effect on ultracold neutron interaction with a wall and implications for computer simulations*. May 2010. DOI: 10.1103/PhysRevC.81.055505. URL: <http://link.aps.org/doi/10.1103/PhysRevC.81.055505>.
- [37] Richard P. Brent. *Some long-period random number generators using shifts and xors*. Ed. by Wayne Read and A. J. Roberts. July 2007.
- [38] Roland Bulirsch and Josef Stoer. “Numerical treatment of ordinary differential equations by extrapolation methods”. In: *Numerische Mathematik* 8.1 (Mar. 1966), pp. 1–13. ISSN: 0945-3245. DOI: 10.1007/BF02165234. URL: <https://doi.org/10.1007/BF02165234>.
- [39] P. Deuffhard. “Order and stepsize control in extrapolation methods”. In: *Numerische Mathematik* 41.3 (Oct. 1983), pp. 399–422. ISSN: 0945-3245. DOI: 10.1007/BF01418332. URL: <https://doi.org/10.1007/BF01418332>.
- [40] Bayram Ali Ibrahimoglu. *Lebesgue functions and Lebesgue constants in polynomial interpolation*. 2016. DOI: 10.1186/s13660-016-1030-3. URL: <http://dx.doi.org/10.1186/s13660-016-1030-3>.
- [41] John David Jackson. *Classical Electrodynamics*. 1999.
- [42] Brad Plaster. *Accessing interior magnetic field vector components in neutron electric dipole moment experiments via exterior measurements*.
- [43] George B. Arfken, Hans J. Weber, and Frank E. Harris. *Mathematical Methods for Physicists*. 2013.
- [44] C.A. Baker et al. “Apparatus for measurement of the electric dipole moment of the neutron using a cohabiting atomic-mercury magnetometer”. In: *Nuclear Instruments and Methods in Physics Research Section A: Accelerators, Spectrometers, Detectors and Associated Equipment* 736 (2014), pp. 184–203. ISSN: 0168-9002. DOI: <https://doi.org/10.1016/j.nima.2013.10.005>. URL: <http://www.sciencedirect.com/science/article/pii/S0168900213013193>.
- [45] W. Gosling and M.J. Cunningham. *Gapped solenoid as a means of producing a highly uniform magnetic field over an extended volume*. 1974. DOI: 10.1049/piee.1974.0329.
- [46] R. Turner and R. M. Bowley. *Passive Screening of Switched Magnetic Field Gradients*.
- [47] Y. Sakamoto C.P. Bidinosti and K. Asahi. *General Solution of the Hollow Cylinder and Concentric DC Surface Current*.
- [48] Y. Sakamoto et al. *Development of high-homogeneity magnetic field coil for  $^{129}\text{Xe}$  EDM experiment*. Apr. 2015. DOI: 10.1007/s10751-014-1109-5. URL: <https://doi.org/10.1007/s10751-014-1109-5>.

- [49] Ito et al. *Technical Design of an Apparatus to Search for the Neutron Electric Dipole Moment at the Los Alamos National Laboratory Ultracold Neutron Source*.
- [50] Ryan Dadisman, Susan Gardner, and Xinshuai Yan. *Trapping penguins with entangled B mesons*. 2016. DOI: <http://dx.doi.org/10.1016/j.physletb.2016.01.002>. URL: [//www.sciencedirect.com/science/article/pii/S037026931600006X](http://www.sciencedirect.com/science/article/pii/S037026931600006X).
- [51] A. Angelopoulos et al. *First direct observation of time-reversal non-invariance in the neutral-kaon system*. 1998. DOI: [http://dx.doi.org/10.1016/S0370-2693\(98\)01356-2](http://dx.doi.org/10.1016/S0370-2693(98)01356-2). URL: <http://www.sciencedirect.com/science/article/pii/S0370269398013562>.
- [52] B. Podolsky A. Einstein and N. Rosen. *Can Quantum Mechanical Description of Physical Reality Be Considered Complete?* 1935.
- [53] A. J. Bevan et al. *The Physics of the B Factories*. 2014. DOI: 10.1140/epjc/s10052-014-3026-9. arXiv: 1406.6311 [hep-ex].
- [54] K.A. Olive et al (Particle Data Group). *RPP Summary Mesons*. 2014.
- [55] M.C Bañuls and J Bernabéu. *CP, T and {CPT} versus temporal asymmetries for entangled states of the Bd-system*. 1999. DOI: [http://dx.doi.org/10.1016/S0370-2693\(99\)01043-6](http://dx.doi.org/10.1016/S0370-2693(99)01043-6). URL: <http://www.sciencedirect.com/science/article/pii/S0370269399010436>.
- [56] Elaad Applebaum et al. *Subtleties in the BaBar measurement of time-reversal violation*. Apr. 2014. DOI: 10.1103/PhysRevD.89.076011. URL: <http://link.aps.org/doi/10.1103/PhysRevD.89.076011>.
- [57] J. Beringer et al. *Review of Particle Physics*. July 2012. DOI: 10.1103/PhysRevD.86.010001. URL: <http://link.aps.org/doi/10.1103/PhysRevD.86.010001>.
- [58] M. Beneke. *Corrections to from {CP} asymmetries in decays*. 2005. DOI: <http://dx.doi.org/10.1016/j.physletb.2005.06.045>. URL: <http://www.sciencedirect.com/science/article/pii/S0370269305008403>.
- [59] Hai-Yang Cheng, Chun-Khiang Chua, and Amarjit Soni. *Effects of final-state interactions on mixing-induced CP violation in penguin-dominated B decays*. 2005. DOI: 10.1103/PhysRevD.72.014006. arXiv: hep-ph/0502235 [hep-ph].
- [60] Gerhard Buchalla et al. *The Pattern of CP asymmetries in B —*i* s transitions*. 2005. DOI: 10.1088/1126-6708/2005/09/074. arXiv: hep-ph/0503151 [hep-ph].
- [61] *Production of highly uniform magnetic field for the n<sup>2</sup>EDM experiment at the Paul Sherrer Institute*. Oct. 19, 2017. URL: <https://meetings.triumf.ca/indico/event/10/session/11/contribution/37>.

## Vita

### Personal Information

Name: James Ryan Dadisman  
Place of Birth: Louisville, KY

### Educational Institutions

M.S. Physics  
University of Kentucky, Lexington, KY  
December 2015

B.S. Physics  
University of Kentucky, Lexington, KY  
July 2008

### Professional Positions

Graduate Research Assistant  
University of Kentucky, Lexington, KY  
Department of Physics and Astronomy  
May 2014 – May 2018

Graduate Teaching Assistant  
University of Kentucky, Lexington, KY  
Department of Physics and Astronomy  
August 2013 – May 2017

### Publications

R. Dadisman, S. Gardner, X. Yan, Trapping penguins with entangled B mesons, Phys. Lett. B754 (2016) 1–5. arXiv:1409.6801, doi:10.1016/j.physletb.2016.01.002.